

© 2025 Christopher C. Young

CONCEPTUAL DESIGN OF HADES
A CUBESAT CONDUCTING RADIO ASTRONOMY IN LUNAR ORBIT

BY

CHRISTOPHER C. YOUNG

THESIS

Submitted in partial fulfillment of the requirements
for the degree of Master of Science in Aerospace Engineering
in the Graduate College of the
University of Illinois Urbana-Champaign, 2025

Urbana, Illinois

Advisor:

Clinical Associate Professor Michael F. Lembeck

Abstract

The “HI Absorption in the Dark agES” (HADES) mission proposes a novel CubeSat architecture to address one of the most significant challenges in modern cosmology: the detection of the redshifted 21 cm neutral hydrogen signal from the Cosmic Dawn and Epoch of Reionization. Observations in the 1 to 100 MHz frequency regime are effectively impossible from Earth due to ionospheric cutoff and intense anthropogenic radio frequency interference. This thesis evaluates the feasibility of a lunar-orbiting 12U CubeSat designed to leverage the Moon’s far side as a natural shield against terrestrial and solar noise, targeting the detection of the global spectral distortion in the cosmic microwave background.

A comprehensive high-fidelity mission simulation framework was developed using the FreeFlyer software suite to assess orbital stability, science access, and subsystem performance. By incorporating the high-resolution GRAIL GL0660B lunar gravity model and third-body perturbations from the Earth and Sun, the study performed an extensive parameter sweep of the lunar orbital phase space. This analysis identified a narrow corridor of “quasi-frozen” near-equatorial orbits ($a \approx 1833$ km, $e \approx 0.01$, $i \approx 0.3^\circ$, $\omega \approx 160^\circ$) capable of maintaining stability for over one year without the need for station-keeping maneuvers. The selected design reference orbit yields 741 h of dual-shielded Prime Science integration time, providing a robust 32 % margin over the 560 h scientific requirement necessary to achieve the required signal-to-noise ratio.

Integrated subsystem analyses confirmed that the proposed platform can support this demanding mission profile. The electrical power system, utilizing 82.75 W beginning-of-life solar arrays and a 93 Wh battery, maintains a positive energy balance with a worst-case eclipse depth of discharge of 25 %, well within operational safety limits. The communications analysis demonstrates that a standard X-band link to the Deep Space Network, allocated just 20 min of contact time per day, provides sufficient capacity (3.50 GB/yr) to downlink the estimated 2.70 GB annual science data volume. These results validate the HADES mission concept, demonstrating that a low-cost CubeSat platform can effectively access the radio-quiet lunar far side to probe the early universe.

To Mom

*“We are the music makers,
And we are the dreamers of dreams...”*

— Arthur O’Shaughnessy, “Ode”

(and Willy Wonka)

Acknowledgments

First, I would like to thank Dr. Maryame El Moutamid and Dr. Amit Vishwas for introducing such an interesting and challenging problem in HADES to LASSI.

Many thanks to graduate student advisors Jenna Russell and Dung Quach-Wisdom, Professors Wayne Chang, Jason Merret, Laura Villafañe-Roca, Robyn Woollards, and Elle Wroblewski for their advice and support.

I wish to thank my LASSI co-conspirators: Isabel Anderson, Rick Eason, David Gable, Michael Harrigan, James Helmich, Qi Lim, Justin Lorenz, Ben Ochs, Murphy Stratton, Courtney Trom, Hongrui Zhao, and Michelle Zosky. Working alongside such an extraordinary and dedicated group of people has been a privilege. I am deeply grateful for your support, friendship, and camaraderie. Y'all challenged me to become a better engineer.

I would like to thank Dr. David Carroll, President of CU Aerospace. While I was a graduate student, he gave me an internship opportunity that helped me build my professional bona fides and later offered me a full-time position at CUA. I am sincerely grateful for his guidance and generosity.

Thank you to my family for always standing by me and cheering me on.

And, finally, the **BIG THREE**:

Thank you to my friend and orbital mechanics OG, **Phoenix Alpine**. Phoenix has a rare gift for combining deep technical expertise with a genuine sense of wonder for the beauty of natural systems. He gives his time generously and quietly inspires everyone around him. He is also one of the most courageous people I have ever met.

Thanks to my advisor and mentor, **Dr. Michael Lembeck**, who gave me a home in LASSI and allowed me to run around (with guardrails) until I found a project that piqued my curiosity and interest. Dr. Lembeck built a unique laboratory that fostered both conventional and unconventional approaches to solving problems. This environment promoted collaboration among other students, academics, universities, government agencies, and industry. His constant support, guidance, and (especially) patience were unwavering and invaluable.

Most of all, thanks to my beautiful wife, **Lisa**. I could not have made this Peter Pan-style journey without her support and sacrifice...period. She endured countless silly engineering and space stories, listened with practiced patience and humour to my grading-fueled TA rants, watched a *ton* of rocket launches, and, on more occasions than I can count, pried the mechanical pencil from my hand and sent me to bed. Lisa, you helped turn the improbable into the inevitable. Thanks, babe. Flawless.

“I’m not like this because I’m in Van Halen. I’m in Van Halen because I’m like this.”

—Cousin Richie, *The Bear*, Season 2, Episode 7, “Forks” (FX, 2023)

Table of Contents

List of Abbreviations	vi
Chapter 1 Introduction	1
Chapter 2 Radio Astronomy Primer	5
Chapter 3 Architecture and Requirements	13
Chapter 4 Lunar Orbit Stability	31
Chapter 5 Simulation Architecture	41
Chapter 6 Orbit Selection Analysis	63
Chapter 7 Power, Communications, and Data	87
Chapter 8 Conclusions	104
References	107
Appendix A Classical Orbital Elements	110
Appendix B HADES FreeFlyer Simulation Code	116

List of Abbreviations

ADC	Analog-to-Digital Converter
ADCS	Attitude Determination and Control System
AOP	Argument of Periapsis
BOL	Beginning of Life
C&DH	Command and Data Handling
CLPS	Commercial Lunar Payload Services
CMB	Cosmic Microwave Background
COE	Classical Orbital Elements
ConOps	Concept of Operations
CR3BP	Circular Restricted Three Body Problem
DARE	Dark Ages Radio Explorer
DoD	Depth of Discharge (of battery)
DSN	Deep Space Network
EIRP	Equivalent Isotropic Radiated Power
EPS	Electrical Power System
FPGA	Field-Programmable Gate Array
HADES	HI Absorption in the Dark agES
HI	Neutral Hydrogen
LASSI	Laboratory for Advanced Space Systems at Illinois
LLO	Low Lunar Orbit
LNA	Low-noise Amplifier
LOS	Line-of-Sight
LPF	Low-pass Filter
$\angle MES$	Moon-Earth-Sun angle
MPPT	Maximum Power Point Tracker

OAP	Orbital Average Power
PDU	Power Distribution Unit
QFO	Quasi-frozen Orbit
RA	Right Ascension
RAAN	Right Ascension of the Ascending Node
RF	Radio Frequency
RFI	Radio Frequency Interference
RX	Receive
SMA	Semi-major Axis
SNR	Signal-to-Noise Ratio
SRP	Solar Radiation Pressure
TA	True Anomaly
TX	Transmit
UTC	Coordinated Universal Time

a	Semi-major axis
e	Orbital eccentricity
i	Orbital inclination
Ω	Right Ascension of the Ascending Node
ω	Argument of Periapsis
ν	True Anomaly

Chapter 1

Introduction

In early 2023, the Cornell Center of Astrophysics and Planetary Sciences contacted the Laboratory for Advanced Space Systems at Illinois (LASSI) at the University of Illinois Urbana-Champaign to assess the feasibility of developing a small research satellite for a novel implementation. Principal Investigators Dr. Maryame El Moutamid and Dr. Amit Vishwas proposed a mission to conduct low-frequency (1 to 100 MHz) radio observations from lunar orbit, specifically targeting the transit periods across the radio-quiet far side of the Moon.

The resulting mission concept was named “HADES” (HI Absorption in the Dark agES). In Greek mythology, Hades is the god of the unseen, a fitting namesake for a mission designed to probe the “Dark Ages” of the universe, an epoch that remains effectively invisible to traditional optical telescopes. The primary scientific objective of HADES is to provide observational measurements of the first sources of light in the universe and early structure formation. It aims to achieve this by detecting the global sky-averaged intensity of the redshifted 21 cm spectral line of neutral hydrogen (HI) against the cosmic microwave background (CMB).

This Master’s thesis presents the systems engineering analysis and high-fidelity simulation framework developed to evaluate the feasibility of the HADES CubeSat mission. It focuses on the critical interplay between orbital dynamics, power generation in cislunar space, and the stringent data requirements of radio cosmology.

1.1 The Scientific Imperative: Probing the Cosmic Dawn

The 21 cm spectral line of HI is one of the most powerful tools in modern cosmology. Produced when the electron in a hydrogen atom undergoes a hyperfine transition, flipping its spin relative to the proton, this line has a rest wavelength of 21 cm (1420 MHz). As the universe expands, photons emitted during early epochs are stretched, or redshifted, to lower frequencies. By observing this redshift, astronomers can map the distribution and state of HI back through cosmic time.

Of particular interest is the epoch known as the “Cosmic Dawn,” occurring roughly 100 million to 500 million years after the Big Bang (redshift $z \approx 15 - 30$). During this period, the very first stars and galaxies formed, emitting ultraviolet light that began to heat and reionize the intergalactic medium. This transition leaves a spectral imprint on the CMB, a distinct absorption trough in the 21 cm signal (Fig. 1.1). Detecting the depth and shape of this trough would constrain the properties of the first stars and potentially reveal non-standard physics, such as interactions between baryonic matter and dark matter [1].

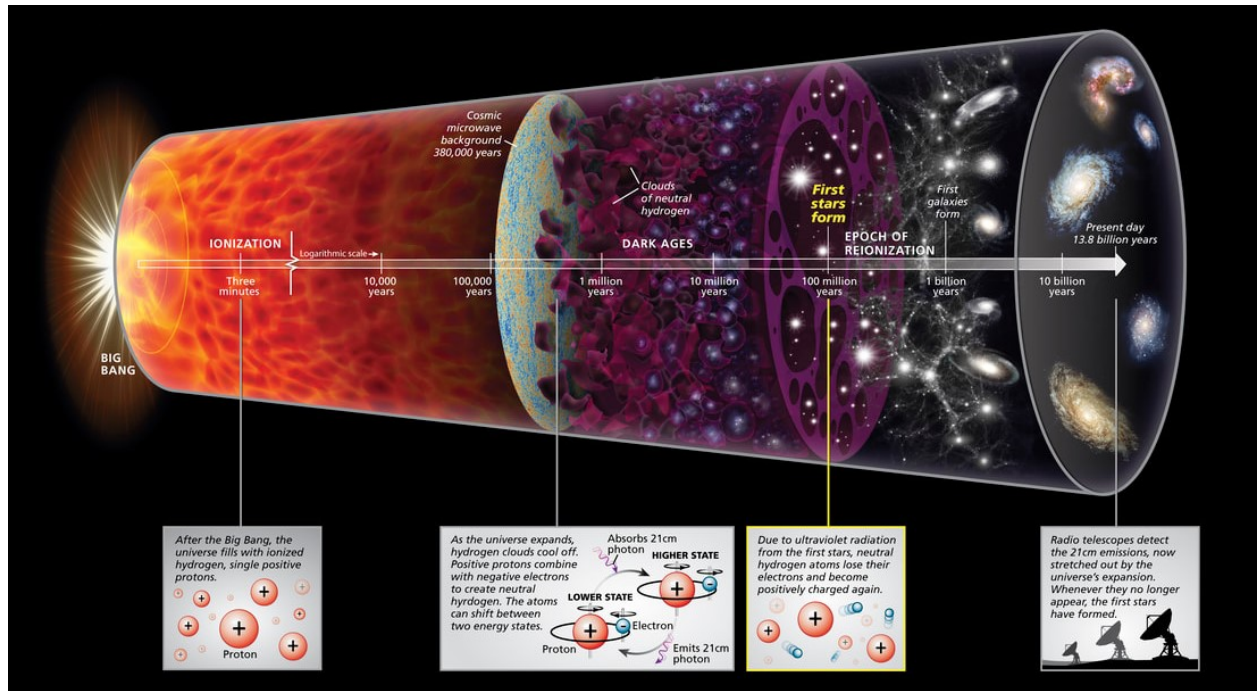


Figure 1.1: 21cm Cosmology.

HI has a rest wavelength of 21 cm. By observing at low radio frequencies, its red-shifted radio emission (and absorption) from gas clouds can be studied. These gas clouds were the raw material that formed the first luminous cosmic structures at these early epochs [2].

However, this signal is elusive. In 2018, the ground-based EDGES experiment reported a detection of this absorption profile centered at 78 MHz [3]. The signal was unexpectedly deep, defying standard cosmological models. Subsequent experiments, such as SARAS 3, have disputed this finding, suggesting the EDGES result may have been an artifact of systematic errors or terrestrial interference [4]. This controversy highlights a fundamental barrier: the relevant frequencies (10 to 100 MHz) are heavily contaminated on Earth. The ionosphere absorbs and refracts signals below 30 MHz, and the entire band is awash in anthropogenic Radio Frequency Interference (RFI) from FM radio, television, and digital communications. To resolve the mystery of the Cosmic Dawn, instruments must go where the Earth’s noise cannot follow.

1.2 Mission Context and Scope

To bypass terrestrial interference, HADES leverages the Moon as a natural shield. A spacecraft in low lunar orbit (LLO) is periodically occulted from Earth, creating a “radio-quiet zone” on the lunar far side. During these intervals, the Moon blocks terrestrial RFI, and if the geometry is correct, can simultaneously block solar radio emissions. This dual-shielded environment offers the low-noise, interference-suppressed conditions necessary to detect the faint nanokelvin-level perturbations of the 21 cm signal.

While mission concepts such as the Dark Ages Radio Explorer (DARE) have previously established the scientific utility of the lunar environment for probing the Cosmic Dawn [5], they typically rely on flagship-class or Discovery-class satellite platforms. HADES represents a novel departure from this paradigm, attempting to achieve similar sensitivity within the extreme size, weight, and power (SWaP) constraints of a 12U CubeSat.

The emergence of NASA’s Artemis program and the Commercial Lunar Payload Services (CLPS) initiative has made access to this environment feasible for university-class missions. HADES is designed as a 12U CubeSat to take advantage of these secondary payload opportunities, reducing launch costs while enabling high-impact science.

For space-based observations to accurately measure high-redshift HI absorption, three target radio continuum foregrounds must be characterized in the 1 to 100 MHz regime. Thus, the specific scientific objectives of HADES are:

- **Galactic Synchrotron Foreground:** Directly measure the average brightness temperature contributed by Galactic synchrotron radiation.
- **Interstellar Dust Foreground:** Measure interstellar dust absorption to place lower limits on the decrease in brightness temperature.

- **Lunar RFI Environment:** Measure the total lunar RFI intensity to provide a novel, high-resolution characterization of the lunar RFI environment’s temporal and frequency evolution.

1.3 Thesis Organization

This thesis is organized to trace the mission design from high-level requirements through detailed simulation and subsystem validation.

- **Chapter 2: Radio Astronomy Primer** provides the necessary background on radio astronomy techniques and the specific advantages of the lunar environment.
- **Chapter 3: Architecture and Requirements** decomposes the science goals into functional and performance requirements for the satellite bus and payload.
- **Chapter 4: Lunar Orbit Stability** reviews the theory of lunar orbital dynamics, discussing the impact of mass concentrations (mascons) and third-body perturbations that drive the search for stable trajectories.
- **Chapter 5: Simulation Architecture** details the custom high-fidelity simulation environment developed in FreeFlyer to model the HADES mission.
- **Chapter 6: Orbit Selection Analysis** presents the results of parametric sweeps used to identify a “quasi-frozen” orbit that balances stability with science access.
- **Chapter 7: Power, Communications, and Data** evaluates the feasibility of the proposed bus architecture, verifying that the solar arrays, batteries, and X-band link can support the selected science orbit.
- **Chapter 8: Conclusions** summarizes the feasibility of the mission.
- **Appendix A** provides a brief refresher on the classical orbital elements and their geometry.

The analysis presented herein demonstrates that by carefully selecting an orbit that exploits the Moon’s natural gravity harmonics, a CubeSat-class platform can survive and operate in the cislunar environment, potentially solving one of the most significant outstanding questions in cosmology.

Chapter 2

Radio Astronomy Primer

To establish the scientific context for HADES, this chapter reviews the fundamentals of radio astronomy and the necessity of space-based observation. Ground-based measurements face severe limitations at low frequencies due to ionospheric cutoff and anthropogenic interference, leaving key regions of the electromagnetic spectrum obscured. The following discussion examines how moving to the lunar environment overcomes these barriers, specifically exploiting the Moon’s natural shielding to create the radio-quiet conditions required for the mission.

2.1 What is Radio Astronomy?

Radio astronomy is the study of celestial objects and physical processes that emit radio-frequency electromagnetic radiation. These emissions span a broad range of frequencies and originate from phenomena such as pulsars, quasars, supernova remnants, and the CMB. Unlike visible light, radio waves have long wavelengths and low photon energies, allowing them to pass through interstellar dust and gas. This makes radio astronomy uniquely suited for probing regions of the universe that are opaque at optical or infrared wavelengths (Fig. 2.1).

Observations in the radio regime have expanded our understanding of the cosmos by revealing otherwise hidden structures and dynamic processes. Measurements of the redshifted 21 cm line of HI, in particular, have opened a window into the early universe and the formation of large-scale structure. Radio astronomy continues to serve as a powerful diagnostic tool in both cosmology and high-energy astrophysics.

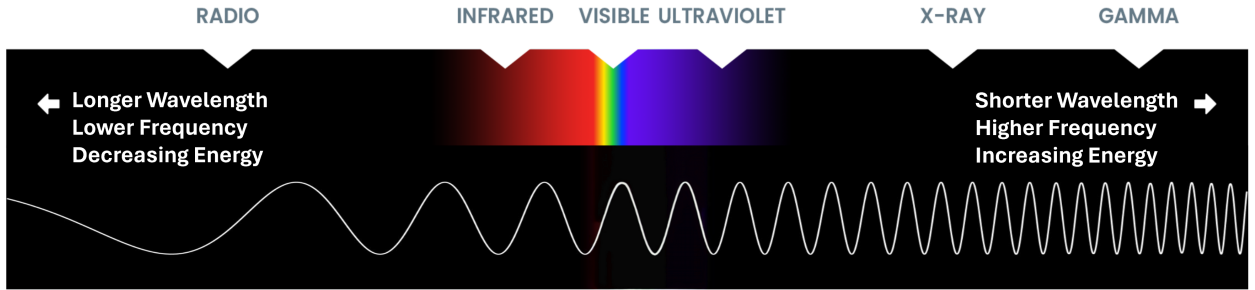


Figure 2.1: The Electromagnetic Spectrum.

Radio waves, characterized by their long wavelengths and low frequencies, are fundamental for exploring astronomical phenomena that remain invisible in other spectra. Visible light, while crucial to many areas of astronomy, represents only a small fraction of what can be observed [6].

2.2 Terrestrial Radio Astronomy

The field of radio astronomy began in the 1930s when Karl Jansky, working at Bell Labs, first detected radio emissions from the center of the Milky Way [7]. This marked the birth of a new observational discipline. Over the following decades, radio astronomy matured rapidly through the development of increasingly sophisticated ground-based instruments.

Large facilities such as the Green Bank Telescope (West Virginia), the Very Large Array (New Mexico), the Square Kilometre Array (South Africa and Australia), and the Five-hundred-meter Aperture Spherical Telescope (China) have enabled discoveries including the first pulsar, the first quasar, the first exoplanet, and the first gravitational lens observed in radio frequencies. These observatories continue to be instrumental in mapping galactic structure, studying transient phenomena, and investigating cosmic magnetism.

2.3 Terrestrial Radio Astronomy Challenges

Despite its successes, terrestrial radio astronomy faces persistent limitations rooted in both natural and artificial interference. The Earth's atmosphere and ionosphere can block, absorb, or refract incoming signals, particularly at low frequencies below 30 MHz. These are precisely the frequencies most relevant to early-universe studies, such as observations targeting the cosmic Dark Ages. In addition to signal attenuation, the ionosphere introduces time-varying distortion and phase noise, degrading both the fidelity and resolution of astronomical data.

Moreover, RFI from human-made sources continues to escalate. The proliferation of communication systems, satellites, and digital electronics has created a crowded and noisy electromagnetic environment around Earth. This interference can mask or corrupt the weak celestial signals that radio astronomers seek to detect.

To mitigate these effects, ground-based observatories adopt a range of strategies: selecting remote or shielded sites, designing robust front-end filters and digital post-processing algorithms, and participating in international efforts to coordinate spectrum allocation and usage. However, these mitigation approaches are increasingly constrained by the growing demand for radio frequency (RF) bandwidth and global connectivity.

2.4 Space Radio Astronomy

Space-based radio astronomy involves the deployment of telescopes and scientific instruments beyond Earth’s atmosphere—on satellites orbiting the Earth, the Moon, or other celestial bodies. This approach offers distinct advantages over ground-based systems by eliminating interference from the atmosphere, ionosphere, and terrestrial RFI. Operating in space allows access to the full radio spectrum, including low-frequency bands that are absorbed or scattered before reaching the ground. These frequencies provide a unique window into the most ancient and distant regions of the universe.

In addition to spectral access, space radio astronomy enables observations from diverse vantage points. Instruments in orbit can be coordinated across multiple baselines to form powerful interferometric arrays, or used independently to monitor transient phenomena with continuous sky coverage. This flexibility in positioning and geometry opens up new observational strategies unavailable from the ground.

Notable missions include Japan’s Highly Advanced Laboratory for Communications and Astronomy (HALCA), the first satellite dedicated to space-based Very Long Baseline Interferometry (VLBI); RadioAstron, a Russian radio telescope operating in concert with global observatories to study cosmic radio sources such as quasars and black holes; and Spektr-RG, a Russian-German space observatory with capabilities across high-energy and radio-frequency domains.

Despite these advantages, space radio astronomy remains technically and economically challenging. Missions must overcome the risks of launch, the constraints of limited power and mass, and the harsh variability of the space environment, all of which can degrade instrument performance and reliability over time.

2.5 Motivation for Radio Astronomy on the Far Side of the Moon

One of the most promising and ambitious locations for a fixed-base radio telescope is the far side of the Moon. The far side of the Moon, the hemisphere that always faces away from Earth, benefits from a unique form of natural shielding. It is not only protected from Earth's RFI but also experiences periodic shielding from solar radio emissions, depending on the Moon's position relative to the Sun. The far side of the Moon is a pristine, quiet platform to conduct low radio frequency observations of the early Universe's Dark Ages, as well as space weather and magnetospheres associated with habitable exoplanets [5]. A radio telescope on the far side of the Moon would have unparalleled sensitivity and resolution far exceeding any current radio telescope on Earth.

Two proposals for surface radio telescopes on the lunar far side surface include:

- **Lunar Crater Radio Telescope (LCRT):** 1 km wide wire mesh antenna suspended within a 3 km wide lunar crater. LCRT utilizes one spacecraft delivering the mesh and a separate lander to deliver DuAxel rovers to build the dish over several days or weeks [8].
- **Farside Array for Radio Science Investigations of the Dark ages and Exoplanets (FARSIDE):** A four-petal shaped array of 128 dipole antennas attached to a power and data tether. A lander/base station delivers a rover that deploys the antennas and tether over the course of several days. FARSIDE is designed to take advantage of the emerging transportation and communication infrastructure associated with NASA's Artemis missions [5].

Similarly, a satellite in lunar orbit will periodically find itself in the shadow of the Moon, eclipsed from the Earth and the Sun. In assessing the location trade-offs in Table 2.1, Cornell concluded that while a ground-based telescope could be built with a large aperture on the lunar far side, a lunar orbiting platform represents a far less complex undertaking for making initial observations.

Table 2.1: Comparison of Locations for Radio Astronomy

Location	Advantages	Disadvantages
Earth Terrestrial	<ul style="list-style-type: none"> • Accessibility: Easier to build, maintain, and upgrade • Cost: Lower cost and complexity • Ability to combine multiple telescopes for interferometry 	<ul style="list-style-type: none"> • Ionosphere: Limits observations to higher frequencies and introduces noise and signal distortion • RFI: Increasing global communication infrastructure significantly hampers observations • Restricted by the Earth's rotation and curvature, which limit the field of view and observation time
Lunar Far Side Terrestrial	<ul style="list-style-type: none"> • RFI Shielding: Bulk of the Moon blocks the radio signals from the Earth • Solar Shielding: Periodic solar radio shielding depending on Moon-Sun geometry • Unaffected by the ionosphere, which allows for observations at lower frequencies • Potential for Large Apertures: The lunar surface can support large, stable antenna structures built from lunar materials • Stable and cold environment, which reduces thermal noise, improves sensitivity, and reduces issues related to orbital dynamics 	<ul style="list-style-type: none"> • Infrastructure Needs: Significant infrastructure must be developed, including habitats, power sources, and communication relays • Cost and Complexity: Transporting materials and building large structures is expensive and complex • Solar Interference: Dependent on the lunar cycle and rotation
Lunar Far Side Orbital	<ul style="list-style-type: none"> • RFI Shielding: Orbiting in lunar shadow can benefit from the Moon blocking Earth's RFI • Solar Shielding: Periodic solar radio shielding depending on Moon-Sun geometry • Flexibility: CubeSats can be deployed and repositioned relatively quickly and easily compared to lunar surface installation • Cost: CubeSats are less expensive to build and launch than large lunar surface structures • Scalability: Multiple satellites can work in a network, offering distributed observations, redundancy, and interferometry 	<ul style="list-style-type: none"> • Limited Power: Smaller solar panels and batteries can restrict operational time • Limited Payload: CubeSats have limited capacity for large antennas or other scientific equipment • Orbital Dynamics: Due to the Moon's irregular gravitational field, maintaining a stable orbit requires frequent adjustments • Short Observation Windows: The best observation periods are limited to when the CubeSat is on the far side of the Moon and in the Moon's shadow, which blocks radio interference from both the Earth and the Sun

2.6 Techniques Used in Radio Astronomy

Regardless of location, radio astronomy is a broad term covering multiple techniques for making celestial observations in the radio frequency domain. Cornell identified multiple techniques that a lunar orbiting satellite could use to investigate HI absorption. For all of these applications, three parameters play key roles in successful radio astronomy observations:

1. **Aperture:** refers to the diameter of a radio telescope's dish or the effective size of an antenna array. It determines the amount of radio waves the telescope can collect and directly impacts the telescope's ability to detect faint signals.

2. **Sensitivity:** the ability of a radio telescope to detect weak or faint signals from astronomical sources.

Sensitivity is driven by factors such as aperture size, the efficiency of the receiving system, and the duration of observations.

3. **Resolution:** the ability of a radio telescope to distinguish between two closely spaced objects in the sky. The higher the resolution, the more detailed the image. Resolution is influenced by telescope aperture and observed radio wavelength.

The aperture size impacts both sensitivity and resolution: a larger aperture collects more radio waves, increasing sensitivity and allowing the detection of fainter signals. It also enhances resolution, enabling the telescope to distinguish closely spaced objects. However, higher resolution can sometimes reduce sensitivity due to narrower beamwidths.

2.6.1 Radio Interferometry

Radio interferometry combines the signals from two or more radio antennas to create a single image of an astronomical source. By measuring the phase differences between the signals received at each antenna, the technique can achieve a much higher resolution and sensitivity than a single radio telescope. This is due to the effective aperture of the interferometer being equal to the distance between the antennas. Radio interferometry provides high-resolution imaging of various astronomical objects, such as stars, galaxies, quasars, and supernova remnants. It is particularly valuable for observing the detailed structures of these objects, which are not possible with single-dish radio telescopes. Other applications include the study of stellar dynamics, the detection of exoplanets, and observing black holes, pulsars, and CMB radiation. While a typical radio telescope is made of a single large dish, an interferometer composed of many dipole antennas is the preferred design for 21 cm observations [1].

2.6.2 Radio Spectroscopy

Radio spectroscopy analyzes the radio frequency spectra emitted or absorbed by celestial objects to determine their composition, temperature, density, distance, velocity, and magnetic field. Molecules and atoms emit or absorb radio waves at specific frequencies, known as spectral lines. By collecting and analyzing these spectra, radio spectroscopy can reveal the chemical composition and physical state of sources. Radio spectroscopy is important for studying dust-obscured regions, star formation, and the structure of galaxies. High sensitivity is crucial for detecting faint spectral lines, and high resolution is needed to distinguish between closely spaced spectral features. A larger aperture improves both these aspects, enabling more detailed and accurate spectral analysis.

2.6.3 Radio Polarimetry

Radio polarimetry is the study of the polarization of radio waves by astronomical sources. A radio telescope equipped with a polarimeter can detect the electric field vectors of radio waves and measure their orientation and degree of polarization. Radio polarimetry can reveal the magnetic field, geometry, and scattering properties of the radio source, as well as the effects of the interstellar medium on the radio waves. High sensitivity is essential to detect subtle polarization signals, and good resolution is necessary to map the polarization structure across different regions of the source. A larger aperture enhances the ability to detect and resolve these polarized signals.

2.6.4 Radio Tomography

Radio tomography involves measuring the intensity and frequency of radio waves from different angles to create detailed images and three-dimensional models of astronomical objects. Radio tomography can reveal the internal structure, density, temperature, and composition of the radio source or the medium, as well as the variations and fluctuations in these parameters. Radio tomography can also detect radio sources or media that are obscured by dust or gas, such as the interstellar medium, the intergalactic medium, or the CMB. Sensitivity is important for detecting weak signals from different depths, and resolution is critical for accurately mapping the three-dimensional structure. A larger aperture contributes to improved sensitivity and resolution, allowing for more detailed tomographic reconstructions.

2.7 A Closing Window of Opportunity

During the writing of this thesis, two landmark achievements advanced lunar exploration.

In February 2024, NASA deployed its first radio telescope on the lunar surface: the Radiowave Observations on the lunar Surface of the photo-Electron Sheath (ROLSES-1) instrument. Delivered aboard Intuitive Machines' *Odysseus* lander, which touched down near the lunar south pole, the instrument operated successfully despite the lander tipping on arrival. ROLSES-1 collected valuable radio frequency data both during transit and over two operational periods on the lunar surface. It detected terrestrial technosignatures in the form of shortwave emissions from Earth that penetrated the ionosphere, along with components of the galactic radio background [9]. These results validated critical elements of the instrument's hardware, calibration, and signal processing chain, providing a technology pathfinder for future low-frequency lunar missions.

In June 2024, China successfully executed their Chang'e 6 mission, a groundbreaking endeavor that achieved the first-ever lunar far side sample return. The Chang'e 6 rover landed in the South Polar-Aitken basin, conducted its scientific operations, and returned collected samples to Earth. Communications were enabled by the Queqiao-2 relay satellite, which not only supported this mission but is expected to serve as a persistent node for future Chang'e operations.

These achievements, however, arrive amid a rapidly evolving lunar environment. Missions in orbit and on the surface are poised to introduce increasing levels of RFI, threatening the viability of sensitive low-frequency observations. “No fewer than—and perhaps far more than—15 distinct civil, commercial, and scientific entities are planning a series of international missions to the lunar surface and orbit over the next two decades” [10]. If emission levels, spectral leakage, and operational frequency bands are not strictly coordinated, the radio-quiet environment essential to Dark Ages science may be lost, no matter the observational vantage point.

Chapter 3

Architecture and Requirements

Translating the scientific objectives of HADES into a flight-ready architecture requires a rigorous decomposition of mission needs into functional and performance requirements. This chapter defines the spacecraft conceptual design, establishing the system-level constraints that govern the satellite configuration, subsystems, and operational logic necessary to support low-frequency radio astronomy in the lunar environment.

3.1 Mission Objectives

The primary objective of the HADES mission is to characterize deep space radio emissions in the 1 to 100 MHz range, mapping the intensity of HI from shortly after the Big Bang. HADES will conduct observations in the quiet zones of lunar orbit, where the radio frequency shadows of the Sun and Earth overlap. To achieve this objective, a systems engineering process was followed to develop a definitive set of mission requirements that guide the design and implementation.

3.2 Systems Engineering Process

The systems engineering technical management process provides a pathway for stakeholder objectives to be formulated into functional, performance, and operational requirements constrained by cost, schedule, and other programmatic considerations. The comprehensive scope of this process ensures a responsive and balanced design (Fig. 3.1). The left-hand side of the V-model follows a top-down approach to system decomposition and design and integration, followed by a bottom-up approach to system verification and validation on the right-hand side

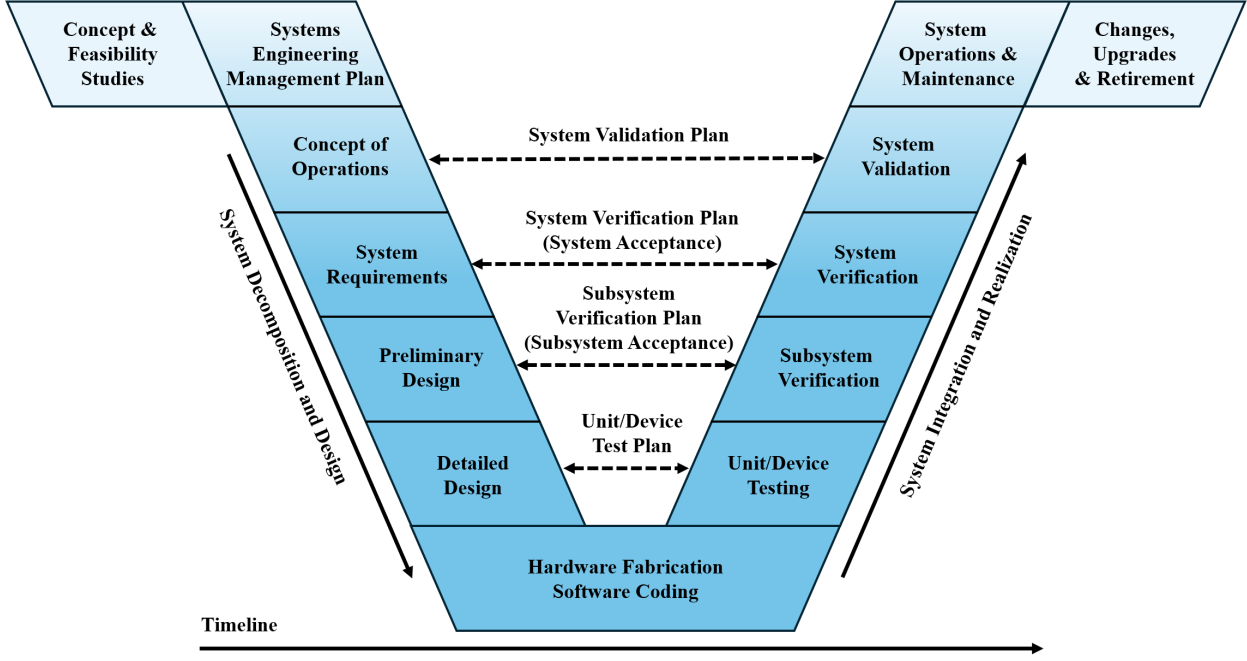


Figure 3.1: Systems Engineering V.

The HADES design is being developed within this framework [11] [12].

3.2.1 HADES Mission Requirements Formulation

HADES concept definition studies were undertaken to assess the technical and operational feasibility of deploying a satellite in lunar orbit to collect radio frequency information from the early universe. This process started with the collection of the most important mission requirements from the Principal Investigators.

HADES must conduct its primary observations in the far side radio-quiet zone of lunar orbit. The Moon acts as a natural shield, making the side away from Earth an ideal location for observing faint cosmic radio signals without interference from Earth's artificial radio sources. This shielding also extends to solar-origin radio bursts, especially during coronal mass ejections, which can overpower the Galactic synchrotron. The Prime Science zone, defined as the region of lunar orbit where the Moon simultaneously shields the Sun and Earth, offers the optimal conditions for detecting the faint cosmic radio signals targeted by HADES. HADES' orbit must be designed to spend sufficient time on the lunar far side to meet this requirement. Because the Moon-Earth-Sun geometry changes over the synodic month, the extent and location of this dual eclipse zone evolve with lunar phase (Fig. 3.2).

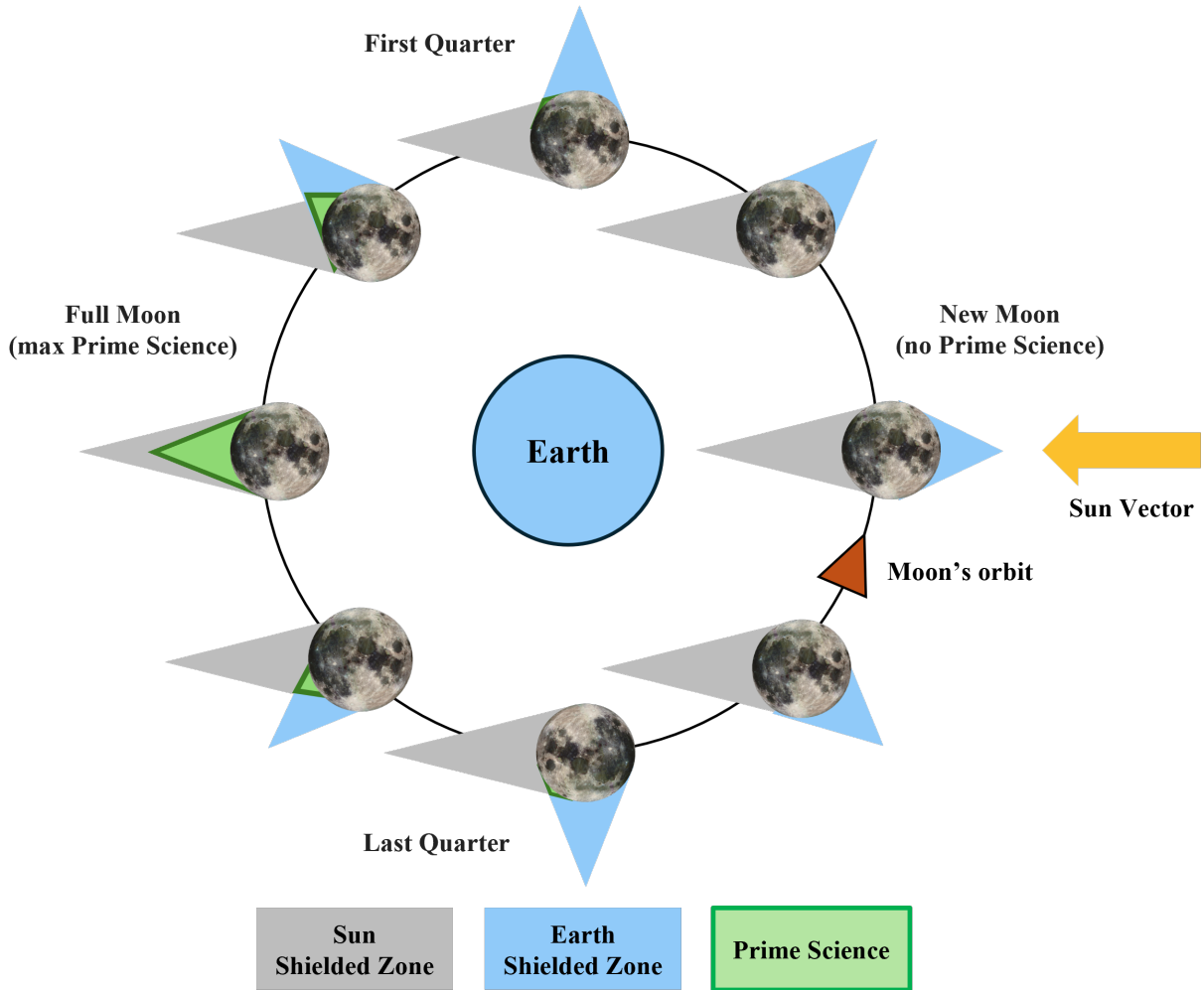


Figure 3.2: HADES Prime Science geometry over the lunar synodic month.

The Moon orbits Earth through several phases, including New Moon, First Quarter, Full Moon, and Last Quarter, with the yellow arrow indicating the Sun direction. Grey cones show the Sun-shielded zone on the lunar far side, blue cones show the Earth-shielded zone, and the green shading marks their overlap, the Prime Science zone. As the lunar phase moves toward Full Moon, the dual-shielded overlap widens, providing the longest intervals of simultaneous shielding from terrestrial and solar radio emission, then contracts again as the Moon moves away from new phase.

Over 560 hours of total integration time on targeted cosmic signals must be accomplished by the mission. This duration is derived from the radiometer sensitivity equation, which dictates the observing time needed to detect the weak 21 cm spectral line embedded within dominant foreground emissions. In practice, accumulating 560 hours of data over the mission will provide sufficient signal-to-noise ratio (SNR) to extract cosmological features from background fluctuations. A science phase spanning several months was planned to meet this requirement. The orbit and key subsystems, such as power, thermal, control and data handling (C&DH), and communications, were designed to support prolonged operations on the lunar far side.

Specific antenna pointing to a region of the sky at a right ascension between $|20 \pm 10^\circ|$ and $|80 \pm 10^\circ|$ and a declination of $-70 \pm 10^\circ$ (in the MJ2000 equatorial frame) is required during the Prime Science phase. This sky region was selected to focus on an area where the 21 cm cosmological signal is predicted to be most prominent and where contaminating Galactic emissions are relatively lower. Meeting this requirement imposes constraints on HADES' attitude determination and control system (ADCS), as the spacecraft must be capable of accurately pointing and maintaining the antenna within the allowed tolerance for extended periods to maximize data collection and quality.

Prime Science observations occur at altitudes below 100 km above the lunar surface. Keeping the spacecraft in LLO ensures that the Moon itself provides maximum shielding from terrestrial radio emissions (longer durations are available at lower altitudes, as the Moon blocks a larger solid angle of Earth). This low altitude substantially attenuates Earth's RFI and mitigates solar radio interference when the spacecraft is in the Moon's radio shadow. However, low altitude comes with a trade-off: the lunar gravity field is highly non-uniform, making such orbits unstable over time. A low-altitude orbit also means a faster orbital period, which limits continuous observation time during Prime Science observation windows. Fig. 3.3 shows a close up of the Prime Science conditions and geometry.

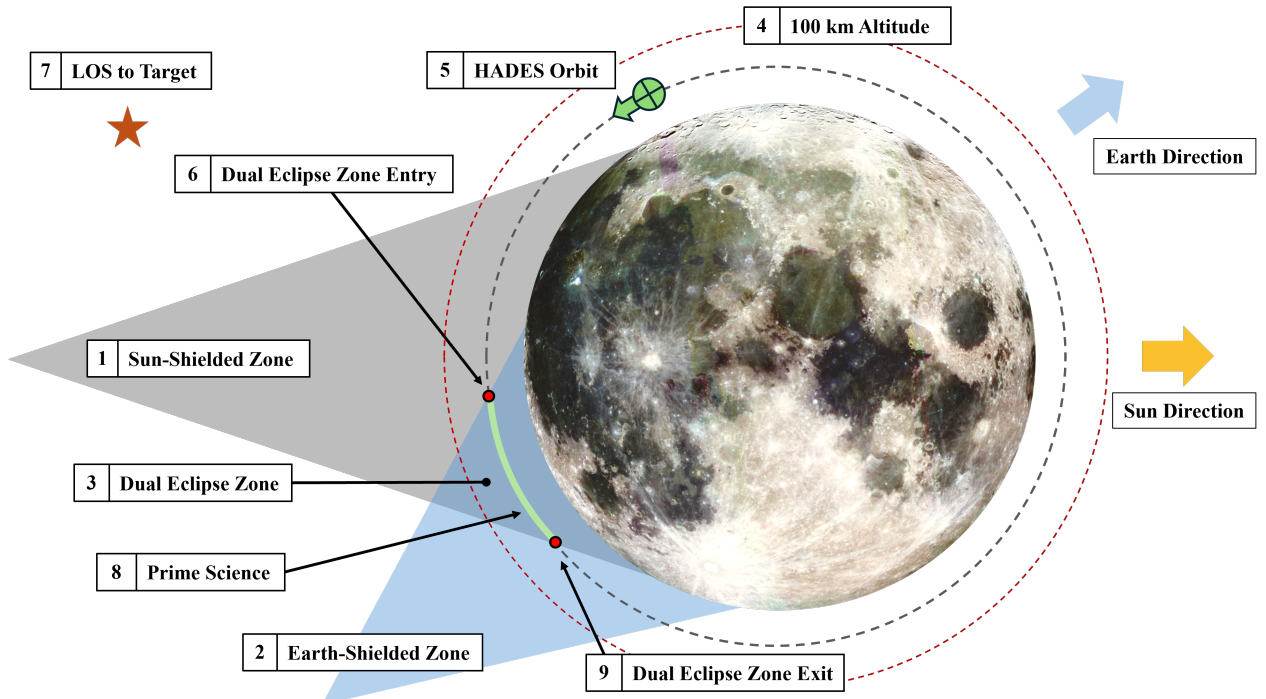


Figure 3.3: Dual-eclipse geometry for HADES Prime Science intervals. The Sun-shielded zone (1) and Earth-shielded zone (2) overlap to form the dual eclipse zone (3) on the lunar far side. The dashed red curve marks the 100 km altitude (4) near the nominal HADES orbit (5). As the spacecraft enters the dual eclipse zone at point (6) and exits at point (9), it transits the highlighted Prime Science segment (8) while maintaining line-of-sight (LOS) to the quiet-sky target (7). The Earth and Sun directions set the occultation geometry that defines these intervals.

Each Prime Science observation period must last at least 20 minutes. This duration ensures that each pass collects enough data to contribute meaningfully to the mission science objectives. Because the target cosmological signals are extremely faint and buried beneath strong foregrounds (for example Galactic synchrotron emission), longer integrations are required to separate signal from noise. As a result, all spacecraft subsystems (power, thermal, attitude, and data handling) must support at least 20 minutes of uninterrupted high-rate science data collection per observation.

Finally, the spacecraft's self-generated radio noise must be suppressed by at least -80 dB relative to the natural background. This electromagnetic compatibility requirement prevents onboard electronics from contaminating the extremely weak radio observations. It drives shielding, component selection, and internal layout, and may require some communication hardware to be powered down or operated in a reduced mode during Prime Science intervals.

Table 3.1 summarizes the principal stakeholder science requirements that guide the design and implementation of the HADES mission and form the basis of its mission concept of operations (ConOps).

Table 3.1: Principal Stakeholder Science Requirements

Requirement ID	Requirement	Note
MSN-1	The mission shall conduct foreground observations in the Prime Science zone.	The Moon provides natural shielding from Earth-based RFI and solar emissions. This environment is essential for detecting faint 21 cm signals from the early universe.
MSN-2	The mission shall provide >560 hours of Prime Science observation time.	Required to build sufficient SNR for signal extraction based on the radiometer equation. Drives mission duration, data storage, power, and communication architectures.
MSN-3	During Prime Science, the HADES instrument antenna boresight shall be pointed at Right Ascension between $ 20 \pm 10^\circ $ and $ 80 \pm 10^\circ $.	Target coordinates selected to optimize for minimal Galactic foregrounds while capturing high-redshift HI signals.
MSN-4	During Prime Science, the HADES instrument antenna boresight shall be pointed at a declination of $-70 \pm 10^\circ$.	Target coordinates selected to optimize for minimal Galactic foregrounds while capturing high-redshift HI signals.
MSN-5	Prime Science observations shall be conducted at altitudes <100 km.	Maximizes RF shielding from Earth.
MSN-6	Prime Science observational periods shall be >20 min.	Ensures enough continuous data is gathered during each observation period to contribute meaningfully to the 21 cm integration.
MSN-7	During Prime Science, HADES RFI/EMI shall be <-80 dB suppression.	Critical to prevent contamination of sensitive observations.

3.2.2 HADES Concept of Operations

The HADES ConOps describes how the mission science objectives are achieved by decomposing it into discrete functional phases (Fig. 3.4).

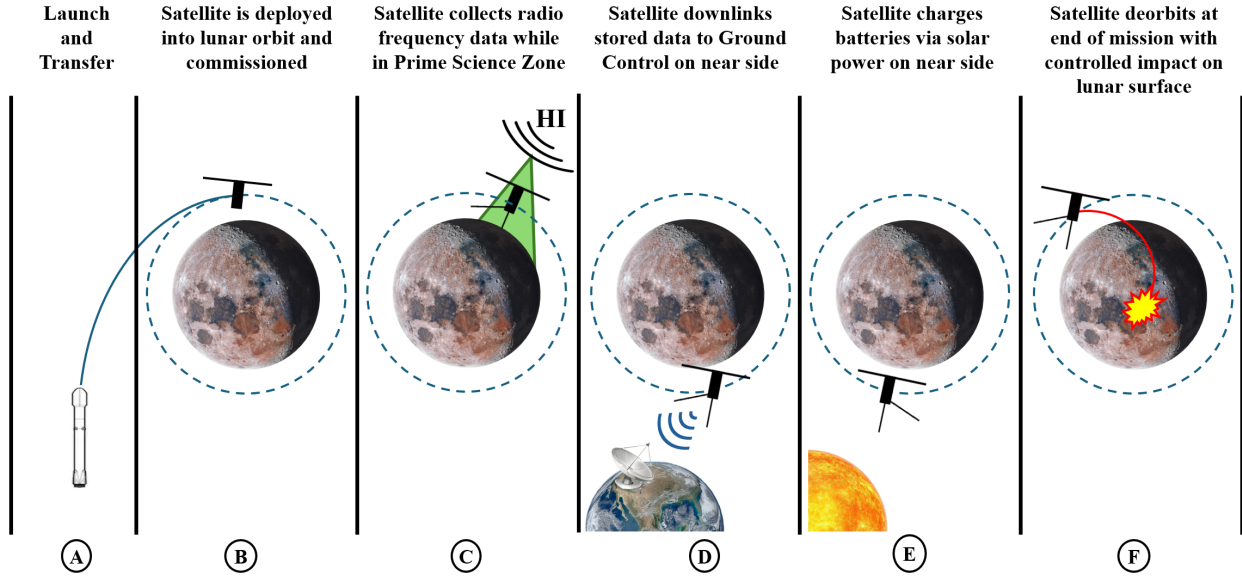


Figure 3.4: HADES ConOps.

The mission begins with launch and trans-lunar injection, followed by lunar orbit insertion. Once in orbit, HADES conducts low-frequency radio science observations on the Moon’s far side, where it is shielded from terrestrial and solar interference. During near side passes, HADES recharges its batteries via solar power and establishes communications with Earth. At end-of-life, a controlled deorbit maneuver ensures a safe, targeted impact on the lunar surface.

Phase (A) Launch and Lunar Orbit Insertion: HADES is delivered to lunar orbit as a secondary payload aboard a commercial lunar rideshare or NASA CLPS mission. The spacecraft is deployed either into lunar orbit by the delivery service. This approach reduces the total ΔV required for HADES operations. After deployment, the spacecraft orients itself, deploys solar panels, activates critical subsystems, and confirms basic health status.

Phase (B) Commissioning: Once in its operational lunar orbit, HADES enters a multi-day commissioning phase to verify the performance of all spacecraft systems prior to initiating science operations. The 3.3 m dipole antenna is extended and checked for structural and functional integrity. The ADCS is calibrated and fine-tuned. The scientific instrument is powered on and run through internal calibration routines, including antenna impedance checks, signal path verification, and noise injection tests via the onboard calibration unit. Telemetry is monitored by ground teams to validate thermal, power, and communication performance. This phase ensures the spacecraft is stable, properly oriented, and capable of meeting science pointing and sensitivity requirements before transitioning to sustained science operations.

Phase (C) Prime Science Observations: The core of the mission takes place when HADES enters a Prime Science zone on the lunar far side and collects wideband radio spectra in the 1–100 MHz range using its deployed dipole antenna and onboard spectrometer. Prime Science observation windows depend on both spacecraft geometry and visibility of the target sky region. To ensure data integrity, internal calibration routines are executed as needed. All non-essential subsystems, especially those that generate RFI, are either powered down or placed in a reduced-noise mode. Prime Science data is stored in non-volatile memory for later downlink.

Phase (D) Data Downlink: Once the spacecraft emerges from the lunar far side and regains LOS with Earth, and depending upon scheduling, HADES enters the communications phase. Stored science data and telemetry are transmitted to the Deep Space Network (DSN) ground stations using an X-band communication system. Ground stations also upload command sequences, ephemeris updates, and software patches during this phase. The system transitions to either standby mode in preparation for the next orbit’s science pass or orients itself for battery recharge.

Phase (E) Battery Recharge: Outside of data downlink phases while on the near side, the primary focus shifts to energy replenishment. HADES orients its solar panels to maximize incident sunlight for efficient power generation. This solar energy is then managed by the onboard power system to recharge the batteries, restoring them to optimal levels required for the subsequent science observation period in the lunar shadow and other operational demands.

Phase (F) End-of-Mission Disposal: At the conclusion of science operations and after all stored data has been transmitted, HADES initiates a controlled deorbit sequence. The spacecraft uses its remaining propellant to lower its perilune, ensuring impact on the lunar surface. This final maneuver prevents the creation of long-term debris in lunar orbit and aligns with planetary protection and sustainability best practices. Telemetry will be transmitted as long as communication is feasible, with the mission formally concluding at surface impact.

3.3 HADES System of Systems

A satellite can be viewed as a “Systems of Systems” (SoS), an assembly of specialized subsystems each performing distinct functions yet all critically interconnected and interdependent. Mission success is contingent not merely upon the individual performance of these subsystems, but critically upon their integrated and synergistic operation. Table 3.2 outlines the major subsystems of HADES.

Table 3.2: HADES Subsystems

Subsystem	Definition
Payload	The primary mission-specific equipment to be accommodated by the spacecraft, including scientific instruments.
Power	This subsystem generates, stores, conditions, and distributes electrical power to all other satellite subsystems. It consists of solar panels for energy generation, batteries for energy storage (especially for operations during eclipses or when solar panels are not illuminated), and power management and distribution (PMAD) to condition, regulate, and switch power.
Command and Data Handling (C&DH)	Often referred to as the On-Board Computer (OBC), this subsystem processes ground commands, manages other subsystems, collects and stores telemetry and science data, and executes scripts for autonomous operations.
Communication	Provides two-way data exchange between the satellite and ground stations. It is responsible for transmitting science data and telemetry to Earth, receiving commands from ground control, and includes transceivers and antennas as primary components.
Attitude Determination and Control (ADCS)	Determines and controls the satellite's orientation in space. It employs celestial sensors (star trackers, sun sensors) and inertial sensors (gyroscopes, accelerometers) for attitude determination. Orientation adjustments are executed using actuators, including reaction wheels or thrusters.
Propulsion	The propulsion subsystem enables controlled velocity changes for two primary functions: initial orbit insertion and deorbiting at the end of the mission. No station-keeping or mid-mission trajectory corrections are performed.
Thermal Control	Maintains satellite component temperatures within operational limits using passive methods (insulation, coatings, heat pipes, radiators) and active methods (heaters) to handle extreme space temperature variations.
Structures and Mechanisms	Provides the primary physical framework for the satellite, accommodating all other subsystems and ensuring structural integrity under launch and operational loads. It includes mechanisms for deployables such as solar panels and antennas.

Derived requirements “flow down” from the high-level mission objectives, the ConOps, and the constraints imposed by the mission. Derived functional requirements define the capabilities necessary to achieve mission success. Performance requirements specify the measurable criteria for implementing the functions. Derived functional and performance requirements for the satellite and subsystems are summarized in the tables below. Each requirement is written as a “shall” statement that is unambiguous, attainable, necessary, and verifiable.

3.3.1 Functional and Performance Requirements

Table 3.3 outlines the functional requirements of the HADES satellite. These requirements specify the essential capabilities and functions the satellite must possess to define its operational scope.

Table 3.3: Satellite Functional Requirements

Requirement ID	Requirement	Note
SAT-1	The satellite shall be compliant with any requirements levied by the launch system.	The satellite must be qualified to design and test standards set by the launch system so as not to endanger the launch vehicle or any other co-manifested systems.
SAT-2	The satellite shall be capable of continuous operations after deployment from the launch vehicle.	Continuous implies that the satellite is self-powered and operates in and out of the Moon's shadow.
SAT-3	The satellite shall maintain a thermally controlled environment for all subsystems and payload in LLO.	The satellite provides an operational environment for the bus and payload instrument.
SAT-4	The satellite shall collect radio frequency data from the payload.	The principal mission objective is to collect radio frequency data while in the Prime Science Zone, when the Moon blocks the Earth and Sun's RFI.
SAT-5	The satellite shall control pointing to celestial position targets in three axes.	The satellite needs to point at a targeted region of space during transit through the Prime Science Zone in order to collect frequency data. Trade studies will determine inputs to pointing control.
SAT-6	Science data shall be collected from the instrument by the C&DH subsystem.	The instrument does not have storage capability.
SAT-7	The satellite shall accept commands uplinked from Ground Control and store them in C&DH memory.	A communication system is required to transfer commands and data from the ground to the satellite.
SAT-8	The satellite shall process uplinked commands.	The satellite will execute command scripts sent from the ground.
SAT-9	The satellite shall downlink data to Ground Control.	Data (science and telemetry) collected onboard the satellite, is sent to ground control for analysis.
SAT-10	The satellite shall maintain time after being initialized by a valid time source.	A real-time clock keeps time onboard the satellite after it is initialized by the ground.

Tables 3.4 to 3.22 list the functional and performance requirements for the all of the HADES satellite subsystems. This thesis concentrated on analyzing the power, data, and communication subsystems.

Table 3.4: Payload Subsystem Functional Requirements

Requirement ID	Requirement	Note
PAY-1	The payload shall collect radio frequency data.	The satellite will point the dipole antenna boresight at the specified celestial target.
PAY-2	The payload shall collect calibration data using an internal reference source.	Known reference signals will be used for instrument calibration and systematic error detection.

Table 3.5: Payload Subsystem Performance Requirements

Requirement ID	Requirement	Note
PAY-3	The payload shall collect > 560 hours of Prime Science data over the lifetime of the satellite.	Orbit lifetime and thermal control capabilities must provide sufficient lifetime to achieve this mission objective.
PAY-4	The payload shall collect Prime Science data in intervals > 20 continuous minutes.	The payload will support programmable acquisition durations of greater than 20 minutes to accommodate variable-length science windows.

Table 3.6: Power Subsystem Functional Requirements

Requirement ID	Requirement	Note
POW-1	The power subsystem shall provide a renewable source of energy for the satellite.	After deployment, solar power must be provided for the mission lifetime.
POW-2	The power subsystem shall provide energy storage for the satellite.	Intended to utilize rechargeable batteries.
POW-3	The power subsystem shall distribute power to the satellite subsystems.	Intended to condition, regulate, and distribute power to all subsystems.
POW-4	The power subsystem storage device shall be chargeable through an access port while stored in the deployer.	Access must be provided through the structure to an access port to keep batteries charged prior to launch.

Table 3.7: Power Subsystem Performance Requirements

Requirement ID	Requirement	Note
POW-6	The power subsystem shall provide 14.0 W to meet the daily average as defined by the mission power budget.	Value derived from the finalized mission power budget using time-averaged duty cycles for science, communications, and housekeeping loads.
POW-7	The power subsystem shall provide 93 Wh of energy storage.	Storage requirement derived from the worst-case eclipse energy deficit and the 30 % lifetime depth-of-discharge limit in the mission power budget.

Table 3.8: Command and Data Handling Subsystem Functional Requirements

Requirement ID	Requirement	Note
C&DH-1	The C&DH subsystem shall store payload data for transmission to Ground Control.	Payload data includes Prime Science Data Segments and telemetry data. The C&DH send the stored data through the communications subsystem to the ground.
C&DH-2	The C&DH subsystem shall provide storage for data received from Ground Control.	Includes commands, data files, and new programs received from the communications subsystem.
C&DH-3	The C&DH subsystem shall store telemetry data for downlink to Ground Control.	Telemetry refers to individual subsystem status or state data.
C&DH-4	The C&DH subsystem shall perform computations on stored data.	Includes processes that store, compress, or alter data.
C&DH-5	The C&DH subsystem shall synchronize the C&DH real-time clock with a time standard.	Time standard in UTC. The software is intended to perform the synchronization with ground control clocks.
C&DH-6	The C&DH subsystem shall execute flight software.	Flight software includes onboard tasks executed by the C&DH operating system as required to operate the satellite.
C&DH-7	The C&DH subsystem shall be re-programmable by external sources.	External access points will be provided, including access ports and ground station uplinks.
C&DH-8	The C&DH subsystem shall provide a mechanism to restart the C&DH processing elements in the event of a recoverable failure.	Intended for application of a watchdog timer. Recoverable failures include those induced by system upsets or caused by errors in the flight software.

Table 3.9: Command and Data Handling Subsystem Performance Requirements

Requirement ID	Requirement	Note
C&DH-9	The C&DH memory shall provide 16 Mbit of nonvolatile storage for commands.	Sized to store all time-tagged command sequences required between worst-case ground contacts, including contingency scripts.
C&DH-10	The C&DH memory shall provide 64 Mbit of nonvolatile storage for flight software.	Allocated for the primary flight software image plus at least one redundant copy and margin for future on-orbit patches.
C&DH-11	The C&DH memory shall provide 512 Mbit of nonvolatile storage for subsystem data.	Based on housekeeping telemetry rates for all subsystems and the maximum interval between downlinks, with margin for anomaly logs.
C&DH-12	The C&DH memory shall provide 4 Gbit of storage for payload data.	Driven by prime-science data volume, on-board compression assumptions, and the maximum number of orbits between downlinks.

Table 3.10: Communications Subsystem Functional Requirements

Requirement ID	Requirement	Note
COMM-1	The communication subsystem shall receive commands from Ground Control.	Command reception is provided by the uplink channel sized in the link budget, with packet validation and error checking to ensure command integrity.
COMM-2	The communications subsystem shall transmit data and telemetry to Ground Control.	Housekeeping telemetry and stored data are formatted into packets and routed to the downlink channel defined in the communications architecture.

Table 3.11: Communications Subsystem Performance Requirements

Requirement ID	Requirement	Note
COMM-3	The communications subsystem shall receive data uplinked from a ground station at a rate of 4 kbps.	Uplink rate is derived from expected daily command volume and typical ground pass durations, with margin for contingency commanding.
COMM-4	The communications subsystem shall transmit downlink data to a ground station at a rate of 64 kbps.	Downlink rate is derived from estimated daily science and housekeeping data volume, the number and length of available contacts, and the X-band link budget.

Table 3.12: Attitude Control and Determination Subsystem Functional Requirements

Requirement ID	Requirement	Note
ADCS-1	The ADCS shall provide pointing control in three axes.	The ADCS will have sensors and actuators allowing it to point at arbitrary celestial targets.
ADCS-2	The ADCS shall provide pointing knowledge in three axes.	The ADCS will include sensors capable of determining spacecraft orientation with sufficient accuracy to support science operations

Table 3.13: Attitude Control and Determination Subsystem Performance Requirements

Requirement ID	Requirement	Note
ADCS-3	The ADCS shall provide three axes pointing control with an accuracy of $\leq 10^\circ$ in each axis.	This ensures the payload antenna boresight remains within the required target field of view during Prime Science observations
ADCS-4	The ADCS shall provide three axes pointing knowledge with an accuracy of $< 2^\circ$.	This supports post-processing and calibration of Prime Science data by ensuring the payload pointing vector is known to within the required angular tolerance.

Table 3.14: Propulsion Subsystem Functional Requirements

Requirement ID	Requirement	Note
PROP-1	The propulsion subsystem shall provide thrust capability for orbital insertion correction after deployment.	Assumes minor ΔV may be needed post-separation to achieve science orbit parameters.
PROP-2	The propulsion subsystem shall support an end-of-life maneuver to ensure impact with the lunar surface.	Satisfies disposal and planetary protection requirements by avoiding long-term orbital debris.

Table 3.15: Propulsion Subsystem Performance Requirements

Requirement ID	Requirement	Note
PROP-3	The propulsion subsystem shall provide a total ΔV capability of ≥ 20 meter/sec.	Derived from combined insertion correction and disposal burn needs.

Table 3.16: Thermal Subsystem Functional Requirements

Requirement ID	Requirement	Note
THRM-1	The thermal subsystem shall maintain an operational thermal environment for the satellite bus subsystems.	Control relies on passive insulation/coatings and active heaters, particularly to maintain battery temperature during eclipse.
THRM-2	The thermal subsystem shall maintain an operational thermal environment for the payload.	Thermal stability is required to minimize gain drift and thermal noise in the Low Noise Amplifier.

Table 3.17: Thermal Subsystem Performance Requirements

Requirement ID	Requirement	Note
THRM-3	The thermal subsystem shall maintain satellite bus subsystem electronics within a temperature range of: $-20^{\circ}\text{C} < \text{Temperature} < 40^{\circ}\text{C}$	Individual subsystem temperature requirements may spawn additional requirements for the thermal subsystem.
THRM-4	The thermal subsystem shall maintain the payload imaging sensor at a temperature of: $-10^{\circ}\text{C} < \text{Temperature} < 40^{\circ}\text{C}$	The payload may provide some embedded hardware to interface with the thermal system to achieve this environment.

Table 3.18: Structure Subsystem Functional Requirements

Requirement ID	Requirement	Note
STRC-1	The structure subsystem shall be compliant with applicable launch provider requirements.	All applicable launch vehicle services provider standards for structures, deployers, etc. will be applied to the design.
STRC-2	The structure subsystem shall accommodate mounting and interface provisions for an external communications antenna.	Includes mounting, stowing (if applicable) and electrical connections for the communications antenna.
STRC-3	The structure subsystem shall provide supporting surfaces for external solar cells.	May include fixed or deployable panel surfaces for mounting external solar cells.

Table 3.19: Launch Vehicle Subsystem Functional Requirements

Requirement ID	Requirement	Note
LV-1	The launch system shall deploy the satellite into LLO.	This requirement will drive downstream specifications for target orbit parameters, including altitude, inclination, and eccentricity, to be defined via trade studies.
LV-2	The launch system shall provide a safe environment for the nonoperational satellite prior to launch.	While under launch provider control, the satellite must be protected from thermal, humidity, and contamination extremes prior to integration and launch.

Table 3.20: Launch Vehicle Subsystem Performance Requirements

Requirement ID	Requirement	Note
LV-3	The satellite shall be maintained by the launch system within an ambient temperature range of $0^{\circ}\text{C} < \text{Temp} < 40^{\circ}\text{C}$.	The launch service provider shall ensure the satellite is stored in a temperature-controlled environment consistent with pre-launch requirements.
LV-4	The satellite shall be maintained by the launch vehicle within an ambient humidity range of $0\% < \text{Humidity} < 60\%$.	The launch service provider shall ensure humidity levels are actively monitored and controlled during satellite handling and integration. May require a dry nitrogen flow prior to deployment.

Table 3.21: Ground Control Subsystem Functional Requirements

Requirement ID	Requirement	Note
GC-1	Ground Control shall provide a command uplink to the satellite.	The ground system transmits data to the satellite's communications interface.
GC-2	Ground Control shall accept data downlinked from the satellite.	The ground system receives telemetry and science data from the satellite's communications interface.
GC-3	Ground Control shall maintain tracking information of the satellite in orbit.	Implies the ability to know where the satellite is located. May use commercial or government tracking assets.

Table 3.22: Ground Control Subsystem Performance Requirements

Requirement ID	Requirement	Note
GC-4	Ground Control shall provide command uplink to the satellite at a rate of 4 kbps.	Uplink rate was selected to match DSN-supported modulation and coding and to allow nominal and contingency command loads to be uploaded within typical contact durations with margin.
GC-5	Ground Control shall accept data downlinked from the satellite at a rate of 64 kbps.	Downlink rate is consistent with the X-band link budget under worst-case geometry and supports the expected daily science and housekeeping data volume within the allocated DSN contact time.

With the functional and performance requirements established, the design effort next defined the onboard systems needed to meet mission objectives within the constraints of lunar orbit. The power, communications, attitude control, thermal, and command and data handling subsystems are specified to support extended operations in the radio-quiet zone during Prime Science observations. With the spacecraft architecture in place, attention now turns to the scientific payload, which acquires and processes the low-frequency radio signals at the core of HADES's science goals.

3.4 The HADES Scientific Payload

The heart of the HADES mission is its scientific instrument, a highly sensitive radio frequency receiver system designed to detect the faint cosmological signals in the 1–100 MHz band (Fig. 3.5). The instrument was engineered with careful attention to sensitivity, bandwidth, and interference mitigation to achieve the mission's science objectives.

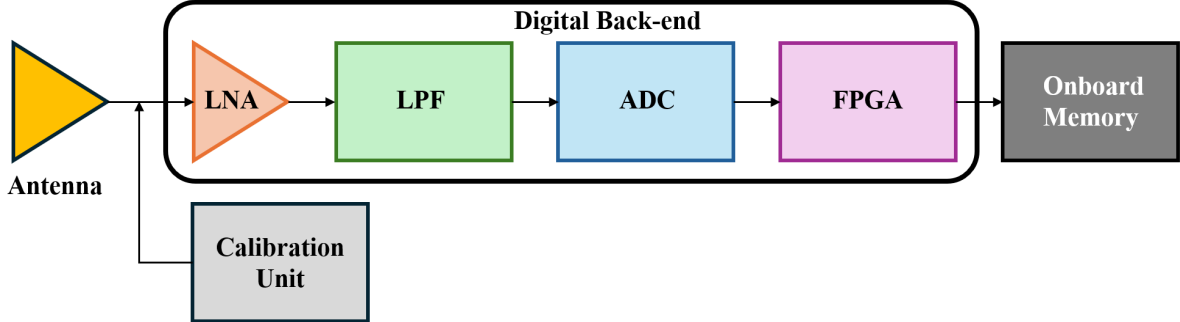


Figure 3.5: Block diagram of the HADES science instrument signal chain.

The incoming cosmic radio signal is received by the dipole antenna and amplified by a low-noise amplifier (LNA). The signal is then filtered by a low-pass filter (LPF) to define the instrument’s operating band 1 to 100 MHz and remove out-of-band interference. The filtered analog signal is digitized by an analog-to-digital converter (ADC) and processed by a field-programmable gate array (FPGA) to compute power spectra. The resulting data is stored in onboard memory. A calibration unit is connected to the antenna input to inject reference signals for periodic gain and system noise calibration.

At a high level, the HADES science instrument is a single-element radiometer: essentially a broadband radio telescope on a small satellite. Its main sensor is a 3.30 m tip-to-tip dipole antenna, which serves as the primary antenna for capturing cosmic radio signals. This dipole is made of two elements, each approximately 1.65 m long, deployed orthogonally during satellite commissioning. The dipole’s length was driven by the desired frequency range: it is roughly half a wavelength at 45 MHz, in the middle of HADES’s band. This configuration provides a reasonably efficient antenna aperture for the band of interest.

The antenna is linearly polarized and is sensitive to radiation from a very large portion of the sky (dipoles have a broad beam pattern, approximately a dipole donut pattern). In HADES’s configuration, the dipole orientation and the spacecraft attitude together determine the sky region being observed, typically one lobe of the dipole’s pattern oriented toward the target sky area.

The frequency coverage of 1 to 100 MHz is extremely broad, spanning two orders of magnitude: from very low frequencies just above the ionospheric cutoff (approximately 1 MHz) up to the lower end of traditional FM radio (100 MHz). This wide range allows HADES to capture both the strongest Galactic foregrounds at lower frequencies as well as the expected 21 cm cosmological signal. The antenna and RF front-end are designed to have a near-uniform response over this band. This necessitates careful impedance matching and a low-loss feed line, as the impedance of a short dipole varies with frequency (the 1 MHz end of the band is far from resonance and thus the antenna is less efficient there).

Despite the inefficiency at the lowest frequencies, HADES includes them in the band to explore phenomena like the ionospheric cutoff and any potential signals in the 1 to 5 MHz range, noting that the lunar ionosphere has a plasma frequency around 0.20 to 1 MHz, which effectively blocks signals below approximately 1 MHz.

The signals collected by the dipole antenna are extremely weak, originating from the faint cosmic background, and are many orders of magnitude fainter than typical terrestrial radio emissions. The first element in the instrument chain is a Low-Noise Amplifier (LNA) located as close to the antenna feed as possible. The LNA boosts the incoming voltage signal from the antenna while adding minimal noise. Following the LNA, a band-defining low-pass filter (LPF) sharply attenuates frequencies above 100 MHz to reject out-of-band interference. The LPF also serves to block frequencies below 1 MHz, effectively band-limiting the input to 1–100 MHz. This filtering is important because any strong signals outside the band (for instance, some spacecraft emissions or solar bursts at higher frequencies) could otherwise saturate the downstream electronics. Notably, the filter design considered the lunar environment: below 1 MHz, the lunar ionospheric plasma frequency means there is little extraterrestrial signal, so HADES sacrifices that part of the spectrum to ensure a cleaner band of interest.

After filtering, the analog signal is fed into a high-speed Analog-to-Digital Converter (ADC). The ADC samples the analog waveform at a very high rate to capture the full 100 MHz bandwidth. Once digitized, the data stream is handed to a set of Field-Programmable Gate Arrays (FPGAs), which perform real-time digital signal processing. The FPGAs implement a spectrometer, channelizing the 1 to 100 MHz band into narrow frequency bins using a Fast Fourier Transform. The spectrometer then integrates the power in each frequency bin over time. This reduces the data rate and improves sensitivity by averaging out random noise fluctuations.

The data output from the instrument is not raw voltage samples, which would be prohibitively large, but rather power spectral density measurements across the 1 to 100 MHz range, integrated over suitable time intervals. The expected data product for each observation period could be a spectrum with 1 MHz resolution (100 channels) averaged over 20 minutes, or a series of finer-resolution spectra that can later be combined on the ground. In terms of volume, even moderate-resolution spectra (e.g., 1000 channels) every few minutes can be accommodated in onboard memory for later downlink after compression or averaging.

The instrument also records housekeeping data, such as LNA temperature, gain settings, and related telemetry used to calibrate the measurements.

To ensure the scientific integrity of these measurements, the instrument includes a calibration subsystem. Calibration is critical for separating true sky signals from internal gain fluctuations, systematic biases, and temperature-dependent effects. The calibration unit is connected to the antenna input through a switchable path and can inject known reference signals, such as thermal noise from a resistor or noise diode, into the signal chain. These references allow periodic in-flight calibration of the system gain and noise temperature. Additionally, the Moon itself provides a natural calibration reference: when the spacecraft’s antenna points

toward the lunar surface, the known thermal emission of the Moon (with its well-characterized brightness temperature at these frequencies) can be used to cross-check and scale the observed spectra. By alternating views of cold sky, the Moon, and internal references, the instrument can maintain high-fidelity calibration over the mission lifetime.

With the functional and performance requirements defined, the remaining primary design driver is the operational environment. The requirement for low-altitude access to the lunar far side places HADES in a regime strongly influenced by gravitational anomalies. To ensure the spacecraft can maintain a stable orbit over the full mission duration, the underlying dynamics must be rigorously characterized. The following chapter analyzes the lunar potential field to identify the stability corridors that bound the feasible mission envelope.

Chapter 4

Lunar Orbit Stability

Designing a long-duration LLO for HADES is fundamentally an orbital-stability problem. A small CubeSat must remain close to the Moon for a year or more while repeatedly accessing a specific region of the far side under stringent viewing and occultation constraints for low-frequency cosmology [3], [4], [5]. Unlike most Earth-orbiting missions, where perturbations from the non-spherical gravity field are relatively well behaved and dominated by J_2 [13], low lunar orbits are shaped by a strongly irregular gravity field due to buried mass concentrations (mascons) and by comparatively strong third-body forces from Earth (and, to a lesser extent, the Sun). These effects can drive large, secular drifts in eccentricity and argument of periapsis, quickly degrading orbit geometry or leading to impact if not carefully managed [14], [15], [16].

To identify a stable trajectory that meets these constraints, the following analysis examines the unique dynamical environment of the Moon. By contrasting the lunar perturbation regime with Earth-orbit dynamics and reviewing the evolution of stability strategies ranging from early reconnaissance probes to modern gravity-mapping missions, a class of quasi-frozen orbits is identified as the optimal solution for the HADES science profile.

4.1 The Challenge of Sustained Operations in Lunar Orbits

The motion of an artificial satellite is never exactly Keplerian. Deviations from the ideal two-body solution arise from non-spherical gravity, third-body perturbations, atmospheric drag (when present), solar radiation pressure, and other forces [13]. For most low Earth orbit (LEO) missions the dominant long-term perturbation is the Earth's oblateness term, J_2 , which drives slow, predictable precession of the orbital plane and argument of perigee. Higher-order harmonics and third-body effects are usually smaller perturbations that can be treated as corrections.

The lunar environment is qualitatively different. First, the Moon’s gravity field is extremely non-uniform. Early tracking of Lunar Orbiter spacecraft and the Apollo subsatellites revealed large, localized positive gravity anomalies over the circular maria, the *mascons*, which strongly perturb low orbits [14], [15], [17]. Second, because the Moon orbits only ~ 60 lunar radii from Earth, third-body accelerations from Earth are large compared to the Moon’s own higher-degree harmonics, particularly for higher-altitude or elliptical trajectories [14], [18]. As a result, no single perturbation term cleanly dominates over long time spans in many useful lunar orbits.

A simple order-of-magnitude comparison illustrates these differences. Consider notional 100 km circular orbits around Earth and the Moon. The central gravitational acceleration is roughly -9.50 m/s^2 for the Earth case and -1.60 m/s^2 for the Moon. At Earth, the perturbing acceleration from J_2 exceeds those from higher-degree terms and third-body effects by several orders of magnitude, enabling compact averaged theories and familiar design tools such as Sun-synchronous orbits [13]. At the Moon, however, the triaxiality coefficient C_{22} and the Earth’s third-body pull are comparable to or larger than the lunar J_2 contribution [16], [19]. The result is a coupled problem in which along-track and radial accelerations vary strongly with longitude and altitude, and the long-term evolution of eccentricity and argument of periapsis becomes highly sensitive to initial conditions.

To frame the design problem, Table 4.1 summarizes the relative sizes of the main perturbing accelerations for representative low-altitude orbits around Earth and the Moon. The values are order-of-magnitude estimates based on canonical gravity models and simple third-body scaling, and are intended to highlight trends rather than provide precise numbers.

Table 4.1: Order-of-Magnitude Comparison of Perturbing Accelerations in Low Orbits

Perturbing Effect	Earth Orbiter (100 km)	Lunar Orbiter (100 km)
Central Gravity	$\sim -9.50 \text{ m/s}^2$	$\sim -1.60 \text{ m/s}^2$
J_2 (Oblateness)	$\sim 10^{-3}$ to 10^{-2}	$\sim 10^{-6}$
C_{22} (Equatorial Ellipticity)	$\sim 10^{-6}$	$\sim 10^{-5}$
Third-Body Gravity	$\sim 10^{-6}$ (Moon)	$\sim 10^{-5}$ (Earth)

For HADES, which targets a low-altitude, mildly eccentric orbit to maximize dwell time in dual Earth-Sun eclipse on the far side, the dominant design concern is not short-term tracking error but the secular evolution of the elements over many months. Without deliberate orbit selection or station-keeping, even orbits that appear benign over a few weeks can evolve into configurations with perilune below the surface or with geometric conditions that no longer meet the science requirements [14], [20]. This motivates a stability-first approach to orbit design.

4.2 The Evolution of Lunar Orbiter Mission Design and Stability Strategies

The history of lunar orbiter mission design reflects the gradual improvement of gravity models and the growing importance of long-term stability considerations. Early missions prioritized short-term reconnaissance and accepted short orbital lifetimes. Later mapping orbiters incorporated frequent station-keeping to counter mascon-driven drifts. More recent designs exploit *frozen* or *quasi-frozen* solutions identified from analytical and numerical studies of the lunar gravity field, significantly reducing propellant requirements. Table 4.2 highlights representative missions along this trajectory.

Table 4.2: Representative Lunar Orbiter Missions and Stability Approaches

Mission	Agency / Epoch	Nominal Orbit	Stability Strategy / Outcome
Lunar Orbiter 1–5	NASA / 1966–67	Elliptical, often low perilune	Short-duration photographic reconnaissance; intentional deorbit after completion to avoid interference and to ensure disposal [17].
Apollo PFS-1/2	NASA / 1971–72	Low, near-equatorial	Unmaintained; PFS-1 survived ~ 1.5 yr near an incl. of $\sim 28^\circ$, whereas PFS-2 at $\sim 10^\circ$ decayed and impacted after ~ 1 month [21], [22].
Lunar Prospector	NASA / 1998–99	100 km polar	Gravity-mapping mission with allocated station-keeping budget; periapsis later lowered to enhance sensitivity before a targeted impact [19], [23].
Kaguya (SELENE)	JAXA / 2007–09	100 km polar	Active maintenance of the main orbiter and two subsatellites; gravity and altimetry data significantly improved pre-GRAIL fields [24], [25].
LRO (Prime)	NASA / 2009–11	50 km polar	Regular station-keeping to maintain a near-circular mapping orbit; ΔV budget ~ 150 m/s for one-year mission [26], [27].
LRO (Extended)	NASA / 2011–present	Elliptical, frozen-like	Transition to a frozen-like elliptical orbit reduced annual station-keeping from $\mathcal{O}(100)$ to a few m/s while preserving science return [27].

Early Reconnaissance: The Lunar Orbiter Program (1966–1967)

The five Lunar Orbiter missions were designed to acquire photographic coverage of prospective Apollo landing sites and to perform basic geodetic measurements, not to explore long-term orbital stability [17]. After initial capture and orbit adjustment, each spacecraft operated in a low, often elliptical mapping orbit for a few weeks to months, then executed a controlled impact. This operational concept deliberately avoided the need to understand or control long-term mascon-driven instabilities.

Ironically, the tracking data collected for navigation provided the first evidence of severe gravity anomalies. Doppler residuals from Lunar Orbiter spacecraft could not be reconciled with a uniform or mildly oblate lunar potential [15], [17]. These discrepancies motivated deeper analysis of the gravity field and set the stage for the discovery of mascons.

Discovery and Geophysical Nature of Mass Concentrations

Muller and Sjogren's classic 1968 analysis of Lunar Orbiter tracking revealed large positive gravity anomalies correlated with the circular maria, leading to the identification of lunar mascons [15]. By mapping residual accelerations along the ground track, they showed that regions such as Mare Imbrium and Mare Serenitatis host strong, localized mass surpluses that pull nearby spacecraft forward and downward.

Subsequent geophysical work established mascons as super-isostatic structures: dense material near the base of large impact basins is supported by a strong lithosphere, rather than having been relaxed away [28], [29]. High-resolution gravity data from GRAIL later confirmed a bull's-eye pattern of positive Bouguer anomalies centered on many large basins [16], [30]. The current consensus is that mascons form through a multi-stage process involving basin-forming impacts, mantle rebound, and infill by dense mare basalts, which are then mechanically “frozen” as the crust thickens [29], [30].

From an orbital-dynamics perspective, mascons introduce strong, longitude-dependent perturbations. Low-altitude passes over major basins experience enhanced along-track acceleration and significant changes in eccentricity and argument of perilune over relatively few revolutions [14], [20]. For unmaintained orbits, this can lead either to rapid impact or to large growth in eccentricity that renders the orbit operationally unusable.

An Unintentional Experiment: The Apollo Subsatellites (1971–1972)

The Apollo Particles and Fields Subsatellites (PFS-1 and PFS-2) provided a natural experiment in low-altitude lunar orbital stability. Deployed from the Apollo 15 and 16 Command Modules, they were intended to obtain extended measurements of the lunar plasma and magnetic environments [21].

PFS-1, released in 1971 into a mildly elliptical orbit with an inclination near 28° , survived for roughly 1.5 years before reentry, its lifetime limited more by programmatic priorities than dynamical instability [21], [22]. PFS-2, however, was deployed in 1972 into a nearly circular ~ 100 km orbit at about 11° inclination. That satellite experienced rapid mascon-driven evolution: its perilune altitude decreased and its eccentricity grew until impact occurred after only 34 days and 425 revolutions [21], [22]. The contrast between these two subsatellites helped establish that low-altitude lunar orbit lifetimes are strongly dependent on inclination and argument of periapsis, not just altitude.

The Era of Active Orbit Maintenance

By the late 1990s, lunar mission designers treated short lifetimes for generic LLOs as an established fact. The Lunar Prospector mission (1998–1999) explicitly budgeted ΔV for maintaining a near-circular 100 km polar mapping orbit for approximately one year, and subsequently lowered periapsis to enhance sensitivity before a planned impact [23]. Analysis of the Prospector radioscience data yielded major improvements in the global gravity field and in estimates of mascon amplitudes [19].

JAXA’s Kaguya (SELENE) mission (2007–2009) carried a main orbiter and two subsatellites, one in an eccentric, low-perilune orbit to enhance gravity resolution [24]. Maintaining these configurations required frequent orbit adjustments and careful modeling of mascon and third-body perturbations, and the resulting tracking data supported improved global gravity models [25]. Together, Prospector and SELENE provided a pre-GRAIL generation of gravity models that were sufficient for basic mission design but still left large uncertainties, particularly on the far side.

NASA’s Lunar Reconnaissance Orbiter (LRO) initially used a quasi-frozen commissioning orbit before entering a 50 km mean-altitude polar mapping orbit for its prime mission [31]. Station-keeping maneuvers every ~ 27 – 28 days were required to bound the altitude and control the location of periselene [26], [27]. This active-maintenance strategy was feasible for a flagship orbiter with ample propellant but is not practical for a small, resource-constrained CubeSat.

High-Fidelity Gravitational Mapping: The GRAIL Mission

The Gravity Recovery and Interior Laboratory (GRAIL) mission revolutionized knowledge of the lunar gravity field. Two identical spacecraft, Ebb and Flow, flew in tandem at low polar altitude and used a Ka-band ranging system to measure inter-satellite distance changes with micrometer precision. These data, combined with radiometric tracking from Earth, enabled the recovery of high-degree spherical harmonic gravity models [16], [30].

The primary mission, at altitudes near 55 km, produced gravity solutions to degree and order 420–660, improving the resolution of the field by several orders of magnitude relative to pre-GRAIL models. The extended mission lowered the orbit to \sim 23 km, allowing ultra-high-degree fields such as GL0900C and GL1500E and complementary independent models including GrazLGM420b [16], [32]. These models resolve gravity features at scales of \sim 10 to 15 km globally and even finer in many regions.

The hemispheric structure of the gravity field is illustrated in Fig. 4.1, which shows a GRAIL-based Bouguer gravity disturbance map derived from the GrazLGM420b model. This visualization makes explicit the contrast between the strongly mascon-dominated near side and the more diffuse far side anomalies [32].

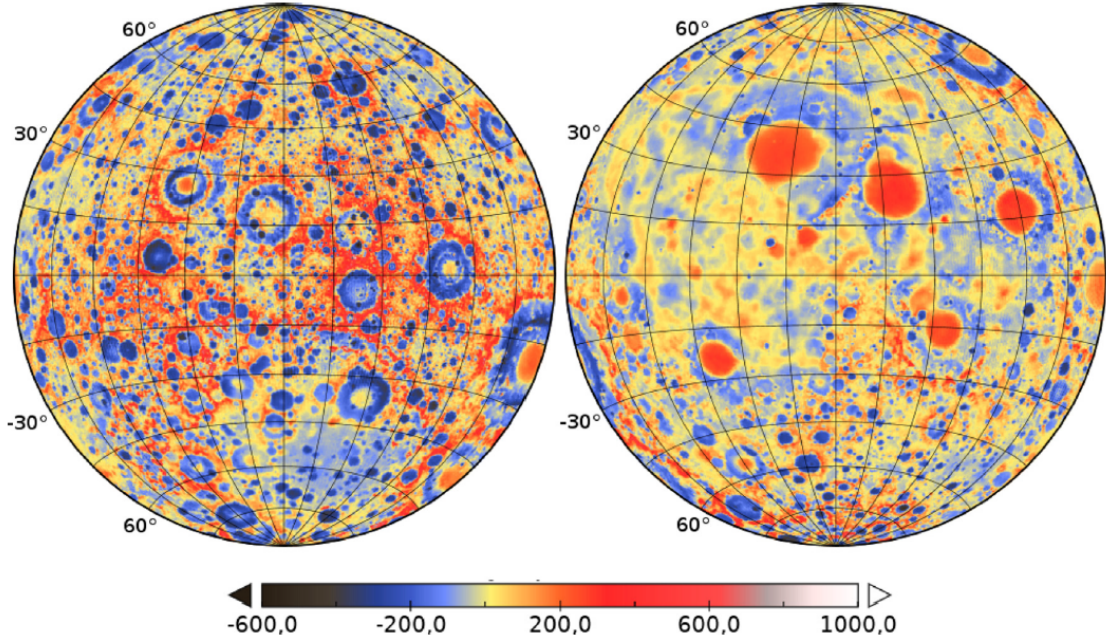


Figure 4.1: Lunar gravity disturbance map.

The GrazLGM420b lunar gravity model, derived from GRAIL Primary Mission data, shows the lunar far side (left) and near side (right). Gravity disturbances are expressed in milligals (mGal), representing deviations from uniform gravity caused by subsurface mass distribution. Larger positive values indicate mass concentrations, while negative values correspond to lower-density crust. These variations influence lunar orbital dynamics and spacecraft trajectory stability [32].

On the near side, strong positive anomalies associated with mascon basins and the Procellarum region dominate the signal, whereas the far side exhibits weaker, more diffuse anomalies [30], [32]. For orbit design, this maps directly onto regions where low-altitude passes are more or less strongly perturbed: near side mascon belts generate large along-track accelerations and secular changes in eccentricity and argument of periapsis, while far side terrain is dynamically quieter.

For missions such as LRO, updating to GRAIL-based fields significantly improved orbit determination and allowed the use of frozen or quasi-frozen extended-mission orbits with small maintenance ΔV [27], [33]. For HADES, GRAIL fields allow the effects of mascons on low-altitude quasi-equatorial orbits to be modeled with sufficient fidelity that long-term stability can be assessed numerically rather than guessed from low-order theories.

4.3 Third-Body Perturbations

At very low altitude, the dominant perturbations on a lunar satellite arise from the Moon's own non-spherical gravity. As altitude increases, however, the gravitational influence of Earth becomes increasingly important. For orbits with apoapsis beyond a few hundred kilometers, secular and long-period effects driven by the Earth can be comparable to those driven by the lunar J_2 , C_{22} , and mascons [14], [18].

The dynamics are conveniently framed in the CR3BP, in which the satellite is treated as a massless third body moving in the combined gravitational field of the Earth and Moon. When expressed in orbital-element form, Earth's perturbation appears as an averaged disturbing function that drives slow evolution in eccentricity e , inclination i , and argument of periapsis ω [18], [20]. For eccentric orbits, these variations can lead to kilometer-per-day changes in perilune altitude at moderate altitudes [14], and to librations or circulations of ω that either help or hinder frozen-orbit conditions.

Analytical treatments typically expand the third-body disturbing function in Legendre polynomials and perform single or double averaging over mean anomaly (and sometimes over the third-body mean anomaly) to derive secular evolution equations. These theories have been used to identify families of frozen orbits in simplified models and to estimate their robustness under the combined influence of lunar zonal and tesseral harmonics plus Earth perturbations [20], [34]. For detailed design of a specific mission like HADES, however, such analytical results are best treated as guides: final assessment of long-term behavior requires numerical integration with a realistic GRAIL-based gravity field and explicit third-body dynamics.

4.4 Modern Solutions: Frozen and Stable Orbits

A *frozen orbit* is an orbit in which selected elements (most often e and ω) exhibit negligible secular drift, so that the orbital geometry repeats over long time scales with only small oscillations. In a Keplerian plus J_2 Earth model, classical frozen orbits are obtained by choosing e , ω , and i such that the averaged rates $\dot{e} \approx 0$ and $\dot{\omega} \approx 0$, typically with $\omega \approx \pm 90^\circ$ so that the perigee lies at high latitude [13]. The same conceptual framework can be extended to the Moon, but the presence of strong tesseral terms (C_{22} and higher) and third-body perturbations makes the analysis more complex.

Elipe and Lara showed that, even in simplified lunar gravity models, there exist families of frozen orbits at essentially all inclinations, with different characteristic eccentricities and arguments of periapsis [20]. Abad et al. later developed an analytical model that provides initial conditions for lunar frozen orbits, validated against higher-degree gravity fields [34]. These studies focus on dynamical equilibria in the averaged system; real spacecraft orbits subjected to a full GRAIL field and third-body effects exhibit small “breathing” oscillations around these equilibria.

From an operational perspective, *quasi-frozen* orbits (QFO) are often more relevant than perfectly frozen solutions. In a QFO, the averaged rates of e and ω are small but non-zero, such that the elements remain bounded within a specified envelope over the mission lifetime [20], [34]. LRO’s extended mission orbit, for example, is an eccentric polar configuration whose periselene location and eccentricity oscillate within controlled limits while requiring only a few meters per second of maintenance ΔV per year [27].

For low lunar altitudes, empirical and numerical studies have highlighted a set of particularly stable inclinations near 27° , 50° , 76° , and 86° [22], [35]. These families correspond to combinations of i , e , and ω in which the disturbing effects of major mascons and Earth’s gravity tend to cancel when averaged over many revolutions. Near equatorial inclinations, additional stable, low-altitude quasi-frozen families have been identified that keep perilune over the far side and avoid the strongest near side mascon belts [36]. Analytical models provide corresponding frozen-orbit solutions in simplified gravity fields that are consistent with these numerical families [34]. These solutions are particularly attractive for low-frequency radio astronomy missions such as DARE and HADES, where science observations are confined to far side radio-quiet windows [5], [36].

The design philosophy adopted in this work is therefore to treat the family of known frozen and quasi-frozen solutions as a dynamical “map,” and then to search within and near those families for orbits that maximize HADES science return while remaining passively stable over a one-year mission.

4.5 Derivation of the HADES Science Orbit

The preceding sections established how low-altitude lunar orbital dynamics are controlled by the combined effects of mascons, global gravity structure, and third-body perturbations, and how modern gravity models enable practical frozen or QFO design. This section describes how those principles are applied to derive a specific quasi-frozen science orbit for HADES.

Recalling Fig. 3.3, HADES science observations are restricted to intervals when four conditions are simultaneously satisfied: (1) the spacecraft is above the far side, (2) both Earth and Sun are occulted by the Moon, (3) the radio antenna boresight is pointed to a designated quiet-sky field within attitude constraints, and (4) the dwell time exceeds a minimum duration (e.g., 20 min) below a maximum science altitude (here 100 km). These requirements directly couple orbital geometry to scientific performance.

Most heritage lunar orbiters have optimized for global coverage, polar illumination, or mapping resolution. By contrast, HADES optimizes the *integrated prime science time* per lunation under dual occultation with continuous target pointing. The resulting orbit need not be polar; instead, it must satisfy three high-level objectives:

- Provide frequent, repeatable dual-eclipse windows on the far side with dwell times ≥ 20 min at altitudes below 100 km;
- Maintain orbital elements (a, e, i, ω) within operational limits over a one-year mission without routine orbit-maintenance burns; and
- Support a feasible attitude and power profile, including off-target slews for power and communication between science intervals.

These objectives motivate the choice of a low-altitude, mildly eccentric, near-equatorial QFO with perilune fixed over the far side.

Modeling Overview

The derivation of the HADES science orbit is carried out using a multi-stage modeling and screening process. Analytical frozen-orbit theory provides initial guesses and qualitative guidance, but the final design relies on long-term numerical propagation with a high-fidelity force model.

The modeling approach adopts the following elements:

- **Gravity Model:** The lunar gravity field is represented by a GRAIL-derived spherical harmonic model truncated at moderate degree (e.g., GL0660B or an equivalent such as GrazLGM420b), capturing the dominant mascon and global structure while limiting computational cost. Earth and Sun gravities are included as point-mass third bodies.
- **Non-gravitational Forces:** For stability assessment, solar radiation pressure and thermal re-radiation are included as perturbations; their effect on long-term element drift is small compared to gravity but not negligible for a low-mass CubeSat.

- **Element Set:** Orbits are parameterized by Keplerian elements $(a, e, i, \Omega, \omega, \nu)$ at a common epoch. To manage the design space, candidate orbits are generated in families that respect known frozen/quasi-frozen structure.
- **Science Geometry:** For each propagated trajectory, LOS to Earth, Sun, and the chosen sky target is computed at each timestep to identify dual-occultation intervals meeting the dwell and pointing requirements, as introduced in Chapter 3.
- **Communications and Duty Cycle:** Confirm that downlink geometry occurs outside the radio-quiet windows and that contact opportunities remain adequate without impacting science intervals.

From Validation to a Design Point

Within the stable candidate set, preference is given to trajectories that exhibit the hallmarks of quasi-frozen behavior: small, bounded oscillations in eccentricity and argument of periapsis, with no significant long-term trend in semi-major axis or inclination. For these orbits, the pattern of dual-eclipse windows repeats from lunation to lunation with only modest phase drift, simplifying mission operations. Within this feasible set, the design point maximizes prime science minutes per lunation subject to altitude, lifetime, and pointing limits. This design point becomes the baseline for the Chapter 5 simulation campaign, and, ultimately, a final science orbit selection and time-domain performance assessment.

Chapter 5

Simulation Architecture

Validating the feasibility of the HADES mission profile requires a rigorous assessment under realistic orbital and operational conditions. To determine if the system architecture defined in Chapter 3 can satisfy the stability constraints identified in Chapter 4, a high-fidelity simulation environment was developed using a.i. Solutions' FreeFlyer software suite. This framework incorporates the GRAIL-based lunar gravity model, solar radiation pressure, and precise ephemerides for the Earth, Sun, and Moon to model the spacecraft's dynamic state with high precision. The following discussion details the simulation structure, force modeling strategies, and autonomous logic used to transform theoretical trajectory candidates into verifiable mission performance metrics.

FreeFlyer has been independently verified and validated (IV&V) through rigorous campaigns conducted by NASA centers, the U.S. Air Force, and commercial operators. According to the 2020 FreeFlyer IV&V Summary Report, FreeFlyer has been applied in both crewed and robotic missions, including operational support for the International Space Station (ISS), James Webb Space Telescope (JWST), and NOAA's GOES series, among others. It is routinely employed by NASA, the U.S. Space Force, the National Reconnaissance Office (NRO), and commercial satellite operators for critical functions such as orbit determination, maneuver planning, and attitude control [37].

This framework enables quantitative evaluation of science access (as provided by spacecraft resources), ground contact duration, and mission length across a range of candidate orbits. The chapter begins by outlining the simulation structure and force models, then walks through the mode logic and filtering criteria, and concludes with validation of candidate orbits and system-level performance metrics.

5.1 Simulation Environment and Setup

The HADES mission simulation was designed to analyze the dynamic operational profile of a long-duration CubeSat in LLO. The simulation architecture integrates deterministic orbit propagation with conditional logic for slewing, science collection, communications, power generation, and eclipse handling. This hybrid system combines FreeFlyer's graphical interface with its object-oriented FreeForm scripting language, enabling examination of key behaviors while maintaining full control over simulation sequencing, data logging, and visualization.

The HADES simulation loop was structured to evaluate spacecraft state and trigger subsystem behaviors on each orbital step. FreeForm scripts were used to implement modular procedures for vector construction, eclipse detection, science window filtering, ground station visibility, power generation and consumption, and data downlink. This modularity allows for rapid iteration across subsystem configurations and operational assumptions. A schematic of the decision logic embedded in each simulation cycle is shown in Fig. 5.1, highlighting key flow paths including dual-eclipse entry, prime science execution, scheduled communication events, and battery recharging.

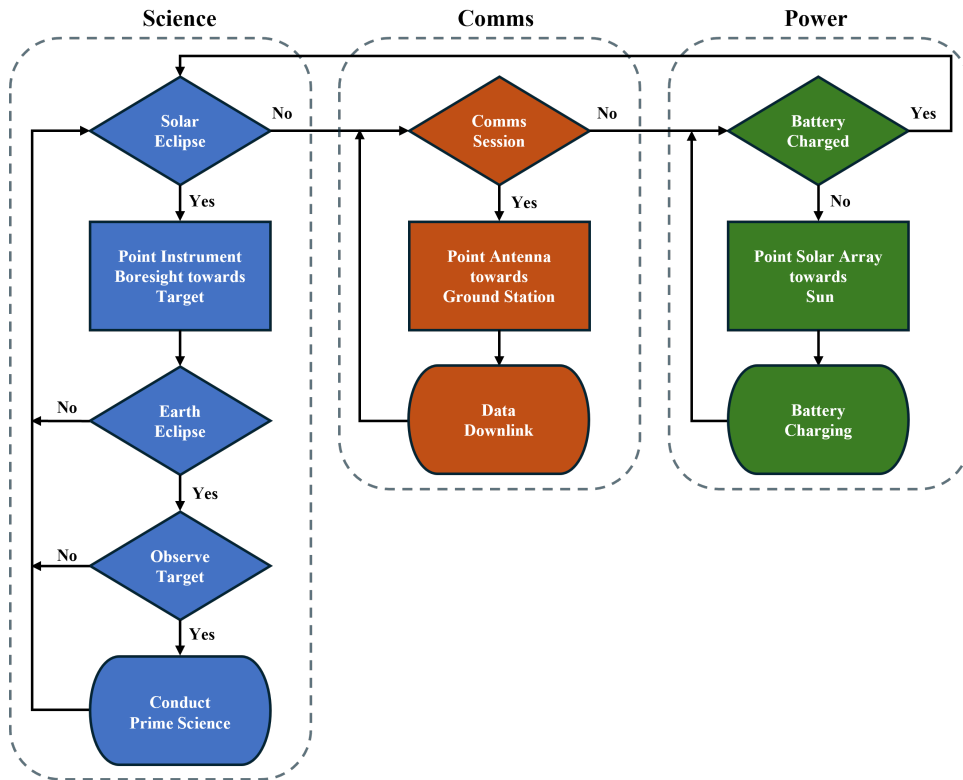


Figure 5.1: High-level simulation logic flowchart.

The timeline-based model executes sequential checks for eclipse conditions, science pointing opportunities, and scheduled communications windows. Depending on geometric visibility and operational constraints, the spacecraft transitions between observation, data downlink, and solar array battery charging modes.

5.2 Spacecraft Setup

Before orbital propagation or subsystem modeling could be performed, a baseline spacecraft object was defined using FreeFlyer's Control screen. This object served as the primary container for all spacecraft-specific parameters, including orbit definition, mass properties, reference frames, and coordinate system settings.

The initial orbit was defined using Keplerian elements in a Moon-centered inertial frame. For a brief refresher on these classical elements and their geometry, see Appendix A. The simulation utilized FreeFlyer's Moon Principal Axis (PA) inertial frame evaluated at J2000. Here, J2000 refers to a standard reference date (January 01 2000) that is widely used in astrodynamics to define fixed inertial directions. The Moon PA frame is centered at the lunar center of mass with axes aligned to the Moon's principal moments of inertia at the J2000 epoch. This orientation is fixed, so it behaves as an inertial frame. The reference plane is the Moon PA equatorial plane and the reference direction is the fixed x -axis of the Moon PA frame. While this Moon-centered inertial frame differs from the familiar Earth-based MJ2000 frame, it is convenient for specifying the lunar gravity field and local orbital geometry. Finally, an epoch defines the reference time from which all orbital states and time-dependent events are propagated. For all HADES simulations, the state epoch was set to January 01 2027 00:00:00 UTC, with states expressed in the fixed Moon PA inertial frame.

The initial orbital elements were varied systematically during early mission design phases to explore a wide range of candidate geometries. Semi-major axis, eccentricity, inclination, and right ascension of the ascending node (RAAN) were swept parametrically to evaluate orbit stability and science visibility. In the final analyses, the orbital elements were explicitly defined to align science opportunities with lunar far side coverage and QFO stability.

Figure 5.2 shows the spacecraft setup tab in FreeFlyer's Control screen, where the epoch, reference frame, and orbital elements are specified.

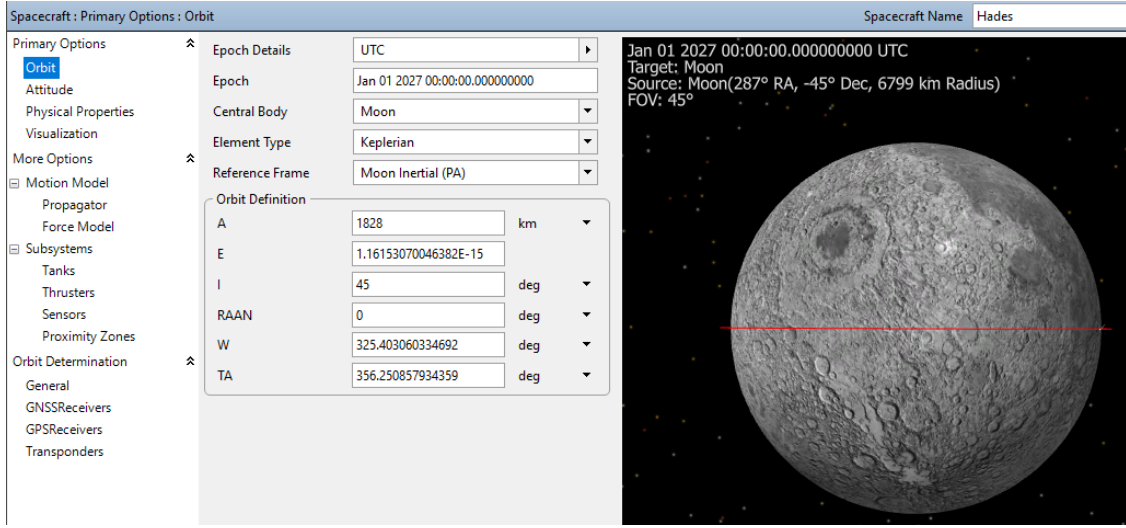


Figure 5.2: HADES initial orbital state definition in FreeFlyer.

The spacecraft is modeled in a Moon-centered inertial frame using Keplerian elements specified at the mission epoch. This configuration reflects a low-altitude lunar orbit with 45° inclination and argument of periapsis selected to align the orbital ground track with far side observation windows. The right-hand pane visualizes the orbit relative to the lunar surface.

5.3 Spacecraft Physical Properties

The spacecraft's physical characteristics were defined in FreeFlyer to support accurate modeling of environmental forces. These parameters determine how solar radiation pressure (SRP) and third-body perturbations influence the spacecraft's motion and response over time. Surface properties for SRP area were assigned nominal values representative of a 12U CubeSat-class platform.

The dry mass was set to 20 kg, consistent with a fully integrated 12U design incorporating deployable antennas, solar panels, and the primary science payload. The center of mass and moment of inertia tensor were derived from a low-fidelity CAD model (Fig. 5.3) assuming a homogeneous internal mass distribution. Although simplified, this model captures the deployed geometry essential for determining the moments of inertia and the projected cross-sectional area. This projected area served as the primary input for the SRP model detailed in §5.5. Finally, these derived mass and geometric properties were entered into FreeFlyer's configuration panel to initialize the spacecraft's dynamic characteristics (Fig. 5.4).

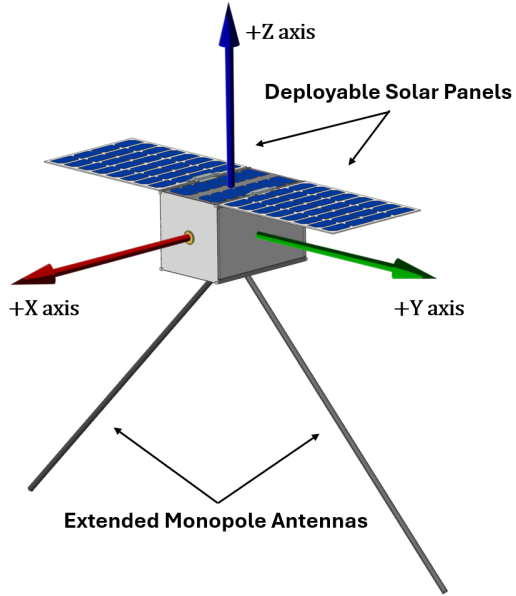


Figure 5.3: Simplified CAD rendering of the HADES spacecraft in its deployed configuration. The 12U bus includes a planar solar array and two extended monopole antennas. This geometry informs the estimation of center of mass, projected surface area, and moment of inertia values used in the simulation.

Spacecraft : Primary Options : Physical Properties																				
<ul style="list-style-type: none"> Primary Options Orbit Attitude Physical Properties Visualization More Options <input checked="" type="checkbox"/> Motion Model Propagator Force Model <input checked="" type="checkbox"/> Subsystems Tanks Thrusters Sensors Proximity Zones Orbit Determination General GNSSReceivers GPSReceivers Transponders 	Aerodynamic Properties <table border="1"> <tr> <td>Drag Area</td> <td>1.0</td> <td>m²</td> </tr> <tr> <td>Lift Area</td> <td>1.0</td> <td>m²</td> </tr> <tr> <td>SRP Area</td> <td>1.0</td> <td>m²</td> </tr> <tr> <td>Coefficient of Drag (Cd)</td> <td>2.2</td> <td></td> </tr> <tr> <td>Coefficient of Lift (Cl)</td> <td>1.2</td> <td></td> </tr> <tr> <td>Coefficient of Reflectivity (Cr)</td> <td>1.4</td> <td></td> </tr> </table>	Drag Area	1.0	m ²	Lift Area	1.0	m ²	SRP Area	1.0	m ²	Coefficient of Drag (Cd)	2.2		Coefficient of Lift (Cl)	1.2		Coefficient of Reflectivity (Cr)	1.4		Dry Inertial Properties
		Drag Area	1.0	m ²																
		Lift Area	1.0	m ²																
		SRP Area	1.0	m ²																
		Coefficient of Drag (Cd)	2.2																	
		Coefficient of Lift (Cl)	1.2																	
	Coefficient of Reflectivity (Cr)	1.4																		
	Mass	20	kg																	
	Center of Mass																			
	X	-0.0896097	m																	
Y	0.1660266																			
Z	0.0877964																			
Moments of Inertia																				
X	0.2011272	Y	0	Z	0															
Y	0	X	0.2999508	Z	0															
Z	0	X	0	Y	0.3052392															

Figure 5.4: HADES physical property configuration in FreeFlyer. The spacecraft's mass properties, aerodynamic areas, and moments of inertia were defined based on standard CubeSat values and CAD-derived analysis. These parameters inform the simulation of SRP and dynamic response to external perturbations.

5.4 Orbit Propagation Configuration

In the orbital simulation, propagation refers to the numerical process of integrating a spacecraft's state forward in time by solving its governing equations of motion. These equations incorporate all significant forces acting on the body. Propagation is performed in a Moon-centered inertial frame using a full force model that includes lunar gravity, third-body perturbations from the Earth and Sun, and solar radiation pressure. Each of these components is detailed in the following sections.

FreeFlyer offers multiple integration methods for modeling spacecraft orbital dynamics. Fixed-step integrators advance the solution using a constant time interval (“timestep”) that ensures consistent output timing but can under-resolve short-lived events if the step size is too large. Variable-step integrators adjust the step size dynamically to follow derivatives while maintaining accuracy within a specified error tolerance.

FreeFlyer allows users to configure their own propagation scheme by selecting an integrator and defining the force environment independently. The integration schemes offered are listed in Table 5.1.

Table 5.1: Integrators Available in FreeFlyer

Integrator	Order	Step Type	Accuracy	Speed	Use Case	Not Ideal For
Runge–Kutta 4	4th	Fixed or Variable	Moderate	Fast	General propagation, impulsive maneuvers	Long-term perturbation analysis
Runge–Kutta 7	7th	Fixed or Variable	High	Moderate	Higher precision without full RK8(9) cost	Highly perturbed orbits
Runge–Kutta 8(9)	8th/9th	Fixed or Variable	Very High	Slower	High-precision lunar orbit modeling	Speed-critical runs
Bulirsch–Stoer	Variable	Variable	Very High	Slow	Long-term orbit evolution with smooth forces	Fast maneuvers, short-duration phases
Cowell (Predictor–Corrector)	Predictor–Corrector	Fixed	Moderate	Fast	Multi-body simulations with stable elements	Impulsive or discontinuous forces

For HADES, the Runge-Kutta 8(9) integrator was selected (Fig. 5.5). This is a high-order, fixed-step method that offers strong numerical stability and sufficient accuracy for long-duration simulations. It is especially effective at capturing brief orbital events such as eclipse transitions, LOS visibility windows, and science-pointing intervals without requiring excessively small-time steps. Although it is not the fastest method

available, its performance provides the accuracy required for mission analysis. Compared to lower-order methods such as RK4 or RK7, RK 8(9) maintains accuracy over longer intervals and supports propagation in conditions where perturbation derivatives are large. It allows the HADES simulation to capture critical transitions in orbit geometry with sufficient resolution and reliability.

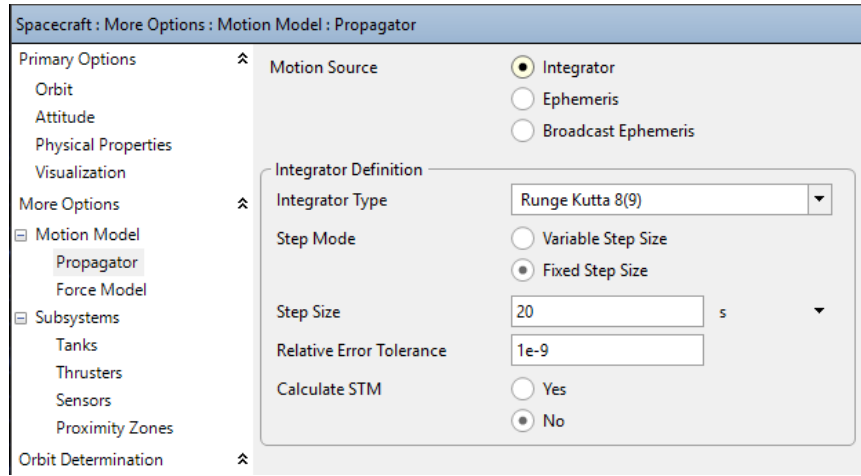


Figure 5.5: HADES integrator settings for final orbit simulations.

The Runge-Kutta 8(9) integrator was configured with a fixed 20-second step size, selected based on convergence testing to ensure accurate capture of transient events. A 60-second step size was used during coarse parametric sweeps to accelerate large-scale orbit evaluations.

To determine an appropriate fixed step size, a convergence analysis was conducted. A representative orbit was propagated over a 30-day period using discrete step sizes ranging from 1 to 120 seconds. Each run produced a summary data file, and `PrimeScienceDurationTotB` was used as the primary convergence metric. This metric includes geometric constraints on eclipse, target alignment, and altitude. Results were plotted against step size to reveal numerical drift and sampling artifacts (Fig. 5.6). Step sizes up to 30 seconds produced nearly identical outcomes, with variations attributed to low-level numerical noise. Beyond 45 seconds, a consistent decline in accumulated science time was observed. At 75 seconds and above, erratic fluctuations appeared, indicating the onset of numerical aliasing due to under-sampling of short-lived events.

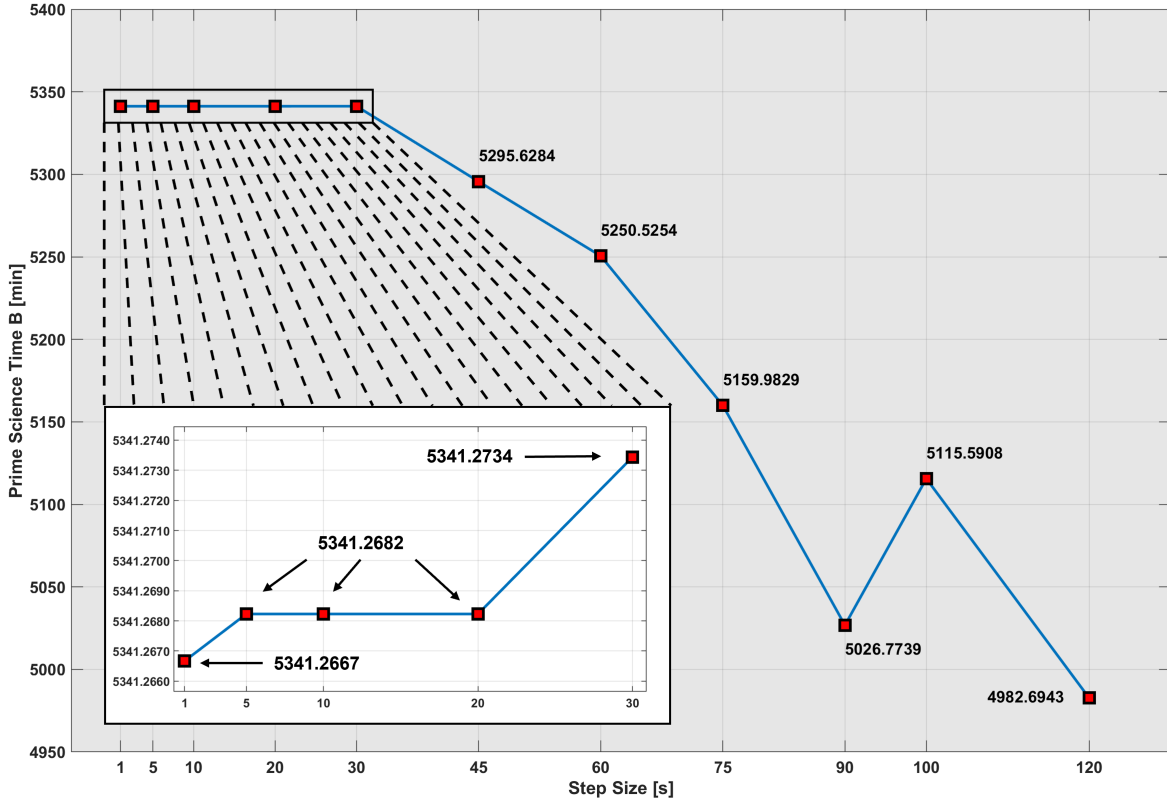


Figure 5.6: Convergence of `PrimeScienceDurationTotB` as a function of fixed propagation step size.

Results demonstrate stable behavior below 30 seconds, with numerical drift becoming noticeable at 45 seconds and severe divergence beyond 60 seconds due to missed transient events. A 60-second step size was selected for coarse design space sweeps, while a 20-second step size was used for final analyses to ensure accurate science metrics with manageable computational cost.

Based on these observations, a two-tier propagation strategy was adopted to balance fidelity with computational efficiency. A 60-second step size was used for preliminary parametric sweeps, such as inclination versus eccentricity studies, where tens of thousands of orbit cases were analyzed to capture global trends. The minor loss in precision at this step size was considered acceptable for such exploratory analyses. For final orbit selection and detailed science opportunity modeling, the step size was reduced to 20 seconds to ensure numerical convergence and accurately capture high-frequency orbital transitions. This choice provides a high-fidelity representation of `PrimeScienceDurationTotB` without incurring the excessive computational costs associated with finer steps of 1–5 seconds, while ensuring that critical events remain fully resolved.

5.5 Force Modeling

The spacecraft was subjected to a set of perturbing forces selected to reflect the dominant influences on long-duration, low-altitude motion around the Moon. These forces are modeled to capture both short-term variability and secular trends that influence orbit stability and science opportunity access over the course of the mission.

The lunar gravity field is modeled using the GL0660B spherical harmonic solution developed from data collected during NASA’s GRAIL mission. This high-resolution model captures the Moon’s asymmetric internal mass distribution, including prominent near side mascon basins and deep crustal anomalies on the lunar far side. For HADES, the model is truncated to degree and order 70. This means the gravitational potential includes harmonic terms up to the 70th order in both latitude and longitude, enabling the model to represent regional-scale variations such as basin structures and mascon clustering. In practical terms, increasing the degree and order of a gravity model is analogous to increasing the resolution of a topographic map. Finer detail is revealed, but at the cost of increased computational load. A 70×70 model strikes a balance by capturing the primary gravitational irregularities that influence low-altitude orbit evolution while excluding higher-frequency features that contribute little over the mission duration.

Gravitational effects from the Earth and Sun were included as third-body perturbations. Each was modeled as a point mass exerting Newtonian acceleration on the spacecraft, with positions resolved relative to the Moon’s center. This approach captured the dominant secular and periodic variations in the lunar orbit caused by evolving Moon–Earth–Sun geometry.

SRP arises from the momentum transferred by solar photons as they impact the spacecraft surface. While each photon carries negligible energy, their cumulative effect produces a continuous, low-magnitude force that can perturb orbital elements over time. In the lunar environment, SRP contributes to secular changes in eccentricity and argument of periapsis, especially for small, low-mass spacecraft.

In FreeFlyer’s spherical radiation pressure model, SRP acceleration acts along the vector from the spacecraft to the Sun and is only applied when the spacecraft is not in eclipse. SRP is applied to the spacecraft modeled as a uniformly reflective sphere. The force magnitude is proportional to the spacecraft’s cross-sectional area normal to the Sun vector, its reflectivity coefficient, and inversely proportional to the square of the Sun-spacecraft distance. This formulation does not depend on the spacecraft’s attitude or panel orientation, making it well suited for simplified long-term analyses. Although it neglects detailed geometry or material effects, the spherical approximation provides a reliable first-order estimate of SRP influence in low-thrust environments such as lunar orbit.

The lunar gravity model was implemented via a dedicated FreeForm script, **Set Lunar Force Model**. The script specifies the GL0660B field, truncates it to degree and order 70, and links the model to the spacecraft object before propagation. All other force model settings, including Earth and Sun third-body perturbations, SRP parameters, and atmospheric drag exclusion, were configured directly within FreeFlyer’s Force Model tab. These definitions remained consistent across all simulations and are shown in Fig. 5.7.

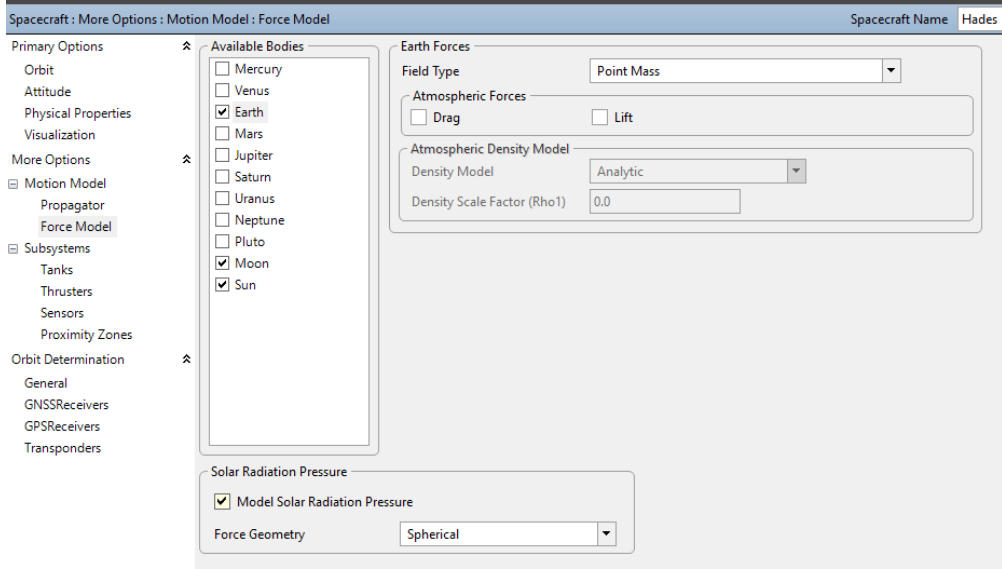


Figure 5.7: HADES simulation force model configuration in FreeFlyer.

Third-body gravitational effects from the Earth and Sun are included as point-mass perturbations. Solar radiation pressure is enabled using the default spherical force geometry. Atmospheric drag is disabled due to the absence of a lunar exosphere at operational altitudes.

5.6 Mission Logic and FreeForm Script Architecture

The operational behavior of the HADES spacecraft was modeled through a structured sequence of modular FreeForm scripts within FreeFlyer. Each script represents a self-contained logic block responsible for a specific subsystem or mission event, such as force modeling, vector construction, attitude slewing, power management, science data collection, or ground-station communication. In combination, these procedures implement both the one-time initialization of the scenario and the recurring mission loop that governs spacecraft behavior throughout the simulation timeline. Although the Mission Sequence editor displays the scripts as a linear list, most entries act as callable subroutines. The **Step HADES and Write to File** driver described in Fig. 5.8 invokes the subsystem procedures cyclically at each integration step, while the initialization routines at the top of the sequence execute only once at the beginning of the run.

In addition to dynamic control, FreeForm scripts also manage the generation of key simulation outputs, including numerical data files, plots, and 3-D visualizations. The complete mission sequence used in the HADES simulation is shown in Fig. 5.8.

//	#	Content
	1	FreeForm: Set Lunar Force Model
	2	FreeForm: Build Vectors
	3	FreeForm: Build Structures
	4	FreeForm: Build Slewing Coordinate Systems
	5	FreeForm: Procedure Slew
	6	FreeForm: Procedure Update Vector Epochs
	7	FreeForm: Procedure Science Calculations
	8	FreeForm: Procedure Ground Station Contact
	9	FreeForm: Procedure Power Generation
	10	FreeForm: Procedure Power Consumption
	11	FreeForm: Build Outputs
	12	FreeForm: Step HADES and Write to File

Figure 5.8: HADES simulation Mission Sequence.

The simulation executes a series of modular FreeForm procedures that define HADES spacecraft dynamics, subsystem behavior, and output generation. Each module encapsulates a distinct function such as force modeling, vector construction, slewing, science operations, power management, or communication, and is invoked conditionally within the simulation timeline.

5.6.1 Set Lunar Force Model

The **Set Lunar Force Model** procedure initializes the gravitational environment used for propagation. In this script, the default point-mass approximation of the Moon is replaced with a high-order spherical-harmonic potential field derived from GRAIL mission data. The propagator associated with the HADES spacecraft is explicitly cast as a Runge-Kutta 8(9) numerical integrator, and the Moon’s gravity field is configured to use the GSFC GL0660B model.

The script defines the lunar field type as a potential model and sets both the degree and order of the spherical harmonics to 70, balancing dynamical fidelity with computational efficiency. The potential file *GL0660B.potential*, located in the FreeFlyer installation directory, contains normalized harmonic coefficients up to degree 660 and represents a truncated form of the full GRAIL field, providing sub-5 km spatial resolution for low-altitude propagation.

This configuration ensures that the simulation accurately captures the lunar gravitational perturbations responsible for long-term orbital drift and stability behavior, while maintaining real-time performance during multi-orbit campaigns. By establishing this environment first in the mission sequence, all subsequent propagation, attitude, and science logic are executed within a physically representative lunar potential.

5.6.2 Build Vectors

The **Build Vectors** procedure establishes the geometric relationships among key bodies and reference points in the simulation, providing the foundation for subsequent access, pointing, and illumination calculations. Multiple Vector objects are instantiated to represent the instantaneous LOS directions from the HADES spacecraft to major celestial bodies and mission targets, including the Earth, Sun, Moon, and the defined galactic science target. Each vector is assigned a unique color and display method within the FreeFlyer 3-D visualization window to support diagnostic analysis of geometry and attitude orientation during runtime. For later use in slewing and science logic, several normalized unit vectors are derived from these primary vectors. These normalized vectors form the basis for computing inertial attitude frames, determining anti-solar pointing configurations, and enforcing the geometric constraints that define valid science observation intervals.

A corresponding *VisibilityCalculator* object is then configured to evaluate LOS visibility and occultation conditions for these same bodies. Visibility segments are created within the *VisibilityCalculator* to assess whether the Earth, Sun, or galactic target are obscured by the Moon or other bodies at any point in the orbit. These visibility checks serve as event triggers for eclipse entry, dual-quiet window detection, and science observation scheduling later in the mission logic sequence.

The script also constructs fixed reference vectors from the lunar center to the Earth, Sun, and target direction. These Moon-centered vectors provide a stable geometric baseline for evaluating relative orientations such as sub-solar and sub-Earth points, as well as for visualizing the evolving Sun–Moon–target configuration.

Finally, separate vector and visibility structures are established to model communication links between HADES and the DSN ground stations at Canberra, Goldstone, and Madrid. Each ground-station vector is initialized with color-coded identifiers and linked to its own visibility segment that accounts for occultations by both the Moon and Earth.

5.6.3 Build Structures

The **Build Structures** procedure declares and initializes persistent states used across the simulation loop. It organizes event timing, geometry flags, power generation and consumption, and battery state into typed containers that downstream procedures read and update without reallocation.

Tables 5.2 to 5.5 provide a detailed inventory of the variables contained within the simulation data structures. The first two tables describe the timekeeping and event-tracking variables, while the latter two summarize the parameters governing power generation, energy storage, and electrical load modeling. These definitions serve as the common interface between the various FreeForm scripts and procedures.

Table 5.2: TIME_KEEPING structure

Structure Field	Type / Units	Definition
DualEclipseStatus	Boolean (0 = no, 1 = yes)	Simultaneous occultation of Earth and Sun by the Moon.
DualEclipseStart, DualEclipseEnd	TimeSpan	Start and end times of the dual-eclipse period.
DualEclipseDuration	minutes	Duration of dual eclipse.
DualEclipseStartAlt, DualEclipseEndAlt	km	Altitude at start and end of dual eclipse.
PrimeScienceStatus	Boolean (0 = no, 1 = yes)	Prime Science window active flag.
PrimeScienceStart, PrimeScienceEnd	TimeSpan	Start and end times of Prime Science window.
PrimeScienceDuration	minutes	Duration of current Prime Science window.
PrimeScienceDurationTotA	minutes	Cumulative Prime Science time (all altitudes).
PrimeScienceDurationTotB	minutes	Cumulative Prime Science time below 100 km.
PrimeScienceAltStart, PrimeScienceAltEnd	km	Altitude at start and end of Prime Science window.
EarthEclipseStatus	Boolean (0 = no, 1 = yes)	Earth eclipsed by Moon (Earthlight blocked).
EarthEclipseStart, EarthEclipseEnd	TimeSpan	Start and end of Earth eclipse.
EarthEclipseDuration	minutes	Duration of Earth eclipse.
SunEclipseStatus	Boolean (0 = no, 1 = yes)	Sun eclipsed by Moon (sunlight blocked).
SunEclipseStart, SunEclipseEnd	TimeSpan	Start and end of Sun eclipse.

Continued on next page

Table 5.2: TIME_KEEPING structure (Continued)

Structure Field	Type / Units	Definition
SunEclipseDuration	minutes	Duration of Sun eclipse.
TargetStatus	Boolean (0 = no, 1 = yes)	Galactic-target pointing active.
TargetStart, TargetEnd	TimeSpan	Start and end of target pointing.
TargetDuration	minutes	Duration of target-pointing interval.
MoonVertexAngle	degrees	Earth–Moon–Sun vertex angle used for geometry gating.
peekFlag	Boolean (0 = first run, 1 = subsequent)	Initialization indicator for first simulation pass.
AltMin, AltMax	km	Minimum and maximum altitude tracked during mission.
EccMin, EccMax	unitless	Minimum and maximum orbital eccentricity tracked.
currOrbitNum	integer	Current orbit index (orbit numbering enabled).
GSContactFlag	Boolean (0 = no, 1 = yes)	DSN contact status flag.
GSIIndex	integer	DSN station index (0 = Canberra, 1 = Goldstone, 2 = Madrid).
GSContactStart, GSContactEnd	TimeSpan	Start and end of DSN contact interval.
GSContactDuration	minutes	Duration of current DSN contact.
GSOrbitNum	integer	Orbit index associated with contact interval.

Table 5.3: POWER_VARS structure

Structure Field	Type / Units	Definition
cellArea	m ²	Area per solar cell.
cellNum	count	Number of solar cells.
cellEfficiency	fraction	Conversion efficiency of cells.
panelPower	W	Instantaneous array output power.
powerUsed	W	Total instantaneous load power.
powerGenerated	W	Instantaneously generated power.
solarFlux	W/m ²	Incident solar flux at spacecraft.

Table 5.4: ENERGY_STORAGE Structure

Structure Field	Type / Units	Definition
DoD	%	Allowable battery depth of discharge.
MaxEnergyStored	Wh	Maximum battery capacity.
MinEnergyBus	Wh	Minimum bus energy required.
EnergyStored	Wh	Battery current state of charge.

Table 5.5: Electrical Loads Definitions

Subsystem	Nominal Draw (W)	Notes
Payload (active)	15.0	Full science mode.
Payload (standby)	2.0	Low-power keep-alive mode.
Payload controller	0.25	Instrument control electronics.
IMU	1.5	Inertial measurement unit.
EPS	0.15	Electrical power system.
Flight computer	0.33	OBC baseline operation.
X-Band transceiver (TX)	29.0	Transmit mode.
X-Band transceiver (RX)	9.0	Receive mode.
Sun Sensors	0.3	6 at 0.05 W each.
Reaction Wheels	3.25	Steady state.
Battery heaters	2.64	8 at 0.33 W each.
ADCS Controller	0.3	Control electronics.
Star Tracker	1.0	Imaging mode.

5.6.4 Build Slewing Coordinate Systems

The Build Slewing Coordinate Systems procedure establishes the reference frames used for Sun and target pointing maneuvers. Two coordinate systems are constructed to define these orientations relative to the spacecraft body axes:

- `csToSun`: aligns HADES $+Z$ axis with the normalized Sun vector, providing optimal solar-panel exposure for power generation during non-science periods.
- `csToTarget`: aligns HADES $-Z$ axis with the normalized galactic-target vector, orienting the radio-antenna boresight toward the science field during prime observation intervals.

Each coordinate system is generated using the *BuildCoordinateSystem* function, which enforces an orthogonal basis by defining a primary alignment vector and a secondary reference vector derived from the HADES to Moon line. Maneuver timing is set to 60 seconds, and these values are passed to the slewing routine described next in the next section.

5.6.5 Procedure Slew

The **Slew** procedure defines the low-level logic used to rotate the spacecraft between Sun-pointing and target-pointing attitudes. It provides the mechanism that physically carries out the attitude changes commanded by higher-level decision logic in the **Run and Step** procedure (§5.6.12), which determines when a slew should occur based on spacecraft illumination.

When called, the procedure compares the spacecraft's current orientation to the target coordinate system, either the Sun-pointing frame or the science-target frame, and computes the angular velocity required to complete the maneuver within the specified time. A temporary spacecraft object is used to calculate the target orientation and determine the relative rotation between the two frames. This relative rotation is then expressed as a quaternion, from which the principal rotation axis and total rotation angle are extracted. The resulting body-frame angular velocity vector is assigned directly to the spacecraft to execute a constant-rate slew toward the target attitude.

The procedure runs continuously throughout the simulation, updating the commanded angular velocity at each step so that slewing remains synchronized with the current orbital geometry. When the spacecraft achieves the desired alignment, the relative rotation angle approaches zero and the spacecraft transitions smoothly into steady-state pointing.

In this architecture, the **Slew** procedure acts as the actuator-level implementation of the attitude control logic, while the higher-level **Run and Step** sequence determines the appropriate attitude mode: Sun-tracking when the spacecraft is illuminated, or science-tracking when it is shadowed. Together, these routines provide a fully autonomous attitude control loop within the FreeFlyer simulation environment.

5.6.6 Procedure Update Vector Epochs

The **Update Vector Epochs** procedure maintains synchronization between the spacecraft's current state and the vector objects defined earlier in the simulation. Because vector objects in FreeFlyer are referenced to bodies that move continuously with time, their associated epochs must be updated whenever the spacecraft state advances.

This short routine takes the active spacecraft object along with the lists of vectors built in §5.6.2 and assigns each vector's epoch to match the spacecraft epoch, ensuring that all reference directions remain temporally consistent. Keeping the vector epochs synchronized guarantees that LOS, occultation, and illumination calculations reflect the correct geometric relationships at each simulation step. This prevents timing drift between propagated spacecraft motion and the dynamic positions of the Earth, Sun, Moon, target, and ground stations.

5.6.7 Procedure Science Calculations

The **Science Calculations** procedure evaluates illumination geometry, target visibility, and science integration windows at each simulation step. It serves as the central logic block for identifying valid radio-quiet intervals when the HADES spacecraft is simultaneously occulted from both the Earth and the Sun while maintaining LOS to the galactic target.

At each update, the procedure reads current visibility states from the *VisibilityCalculator* objects defined in §5.6.2 and synchronizes them with the **TIME_KEEPING** structure. The logic first determines the individual visibility of the Earth, Sun, and target, recording start and end times along with elapsed durations for each event. When both the Earth and Sun are simultaneously occulted by the Moon, the **DualEclipseStatus** flag is set, marking the beginning of a radio-quiet interval. The interval closes when either body reappears, and the **DualEclipseDuration** is computed and stored.

If target visibility occurs concurrently with a dual eclipse, the **PrimeScienceStatus** flag is triggered, signifying a valid science window. The spacecraft altitude at the start and end of this window is recorded, and the duration is added to cumulative totals stored in **PrimeScienceDurationTotA** (all altitudes) and **PrimeScienceDurationTotB** (periods below 100 km). These accumulated values represent the total science integration time across the simulation timeline.

All results are written to the TIME_KEEPING structure and exported through data tables for post-processing. The procedure also updates vector visualization flags so that Earth and Sun vectors are displayed only when visible, and the target vector is displayed solely during active science windows. This continuously updating logic enables real-time assessment of science opportunity, linking the dynamic orbital geometry to mission performance. It provides the quantitative basis for later analysis of total science time, altitude distribution, and duty cycle within the simulation results.

5.6.8 Procedure Ground Station Contact

The **Ground Station Contact** procedure determines downlink opportunities between the HADES spacecraft and the three DSN stations. The routine uses the *VisibilityCalculator* segments created in §5.6.2 to assess when each ground station has a clear LOS to the spacecraft. These visibility checks account for both lunar and Earth occultations to ensure that communication links are established only when the spacecraft is geometrically visible to the station.

At each simulation step, the routine reads the current spacecraft epoch and evaluates the visibility status of all ground-station segments. When a new contact event begins, the `GSContactFlag` is set to 1, the corresponding ground-station index is stored in `GSIndex`, and the `Active` property of the relevant vector in the *hadesToGS* function is enabled for visualization. The start time of the contact is recorded as `GSContactStart`.

While a contact is active, the routine continues to monitor the selected ground station's visibility segment. When an end event is detected, the `GSContactFlag` is reset to 0, the end time (`GSContactEnd`) and duration (`GSContactDuration`) are computed, and the results are reported to the FreeFlyer console. The ground-station vector is then deactivated, and the routine resets for the next contact event.

This continuously updating logic ensures that contact windows are dynamically synchronized with the spacecraft's orbit and the relative motion of the Earth and Moon. The outputs provide both time-resolved downlink opportunities and cumulative statistics on communication access for each DSN site. These data support later analysis of downlink scheduling, data-volume allocation, and mission timeline planning.

5.6.9 Procedure Power Generation

The **Power Generation** procedure calculates instantaneous electrical output from the spacecraft's solar panels as a function of orientation, illumination, and solar flux. It updates the POWER_VARS structure at each simulation step, providing a continuously varying estimate of available power that responds to Sun incidence geometry and eclipse conditions.

The procedure begins by reading panel properties, including cell area A_{cell} (m^2), number of cells N_{cell} , and nominal conversion efficiency η_{cell} , from the `Power` structure and obtaining the instantaneous solar flux G_{\odot} (W/m^2) from the spacecraft object. The Sun vector is then transformed from the inertial frame to the body coordinate system using the `AttitudeConvert` function so the local Sun direction can be compared to the $+Z$ panel normal (Fig. 5.9).

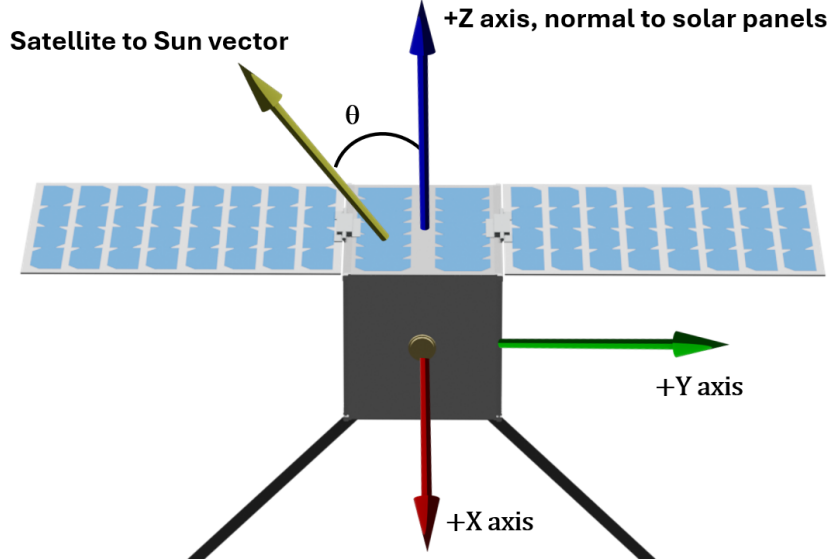


Figure 5.9: Sun-incidence geometry for the HADES power model.

The Sun vector in the body frame is compared to the $+Z$ body axis, which is normal to the solar panels, to define the incidence angle θ . Only the $+Z$ panel is modeled; generated power scales with $\cos \theta$ for $\theta < 90^\circ$ and is zero for $\theta \geq 90^\circ$ or during eclipse.

Only the $+Z$ panel is modeled as active for power generation, consistent with HADES nominal Sun-pointing attitude. The Sun vector in the body frame is compared to the $+Z$ body axis to define the incidence angle θ . When the spacecraft is illuminated (`InShadow = 0`) and the Sun incidence angle is less than 90° , the procedure first forms the beginning-of-life normal-incidence array power

$$P_{\text{array,BOL}} = G_{\odot} A_{\text{cell}} N_{\text{cell}} \eta_{\text{cell}}, \quad (5.1)$$

and then scales this value by $\cos \theta$ to obtain the ideal array DC power at that time step,

$$P_{\text{array}}(t) = P_{\text{array,BOL}} \cos \theta(t). \quad (5.2)$$

When the Sun is more than 90° from the panel normal or the spacecraft is in eclipse, $P_{\text{array}}(t)$ is set to zero.

To represent non-ideal effects and downstream electronics, the code applies a constant derating factor f_{derate} to account for temperature, degradation, and harness losses, and multiplies by the Maximum Power Point Tracker (MPPT) and Power Distribution Unit (PDU) efficiencies η_{MPPT} and η_{PDU} . The instantaneous power available on the regulated bus is therefore

$$P_{\text{bus}}(t) = P_{\text{array}}(t) f_{\text{derate}} \eta_{\text{MPPT}} \eta_{\text{PDU}}, \quad (5.3)$$

and is set to zero whenever the spacecraft is in eclipse or the panel is backlit.

The resulting instantaneous bus power is stored in the variable `powerGenerated` for use by the energy-storage and power-budget subsystems. Evaluated at $\theta = 0^\circ$, Eq. (5.1) and Eq. (5.3) yield the beginning-of-life array power $P_{\text{array,BOL}}$ and the corresponding bus power that appear in the orbit-average power analysis in Chapter 7. This continuously updating calculation links attitude dynamics and orbital lighting conditions to the electrical subsystem model, providing realistic power generation behavior across illuminated, shadowed, and slewing intervals within the FreeFlyer simulation.

5.6.10 Procedure Power Consumption

The **Power Consumption** procedure models the spacecraft's instantaneous electrical load and updates the onboard energy state each simulation step. It determines which subsystems are active based on mission conditions, computes total power draw, and adjusts stored battery energy accordingly.

Each subsystem's nominal load is defined within the *ElectricalLoad* array, with corresponding *LoadFlag* values used to enable or disable power consumption dynamically. The routine begins by setting baseline load conditions for essential systems such as the flight computer, attitude sensors, and the electrical power system (EPS). Conditional logic then modifies these flags based on operational state.

During ground-station contact events, both the transmit and receive functions of the X-band transceiver are activated, significantly increasing total power use. When a prime science window is active, the payload and controller are powered on to enable radio observations. Thermal control heaters are toggled on whenever the spacecraft is in shadow, compensating for radiative cooling during eclipse.

At each propagation step, the routine computes total instantaneous power draw using a vector dot product between the *ElectricalLoad* and *LoadFlag* arrays. The resulting `PowerUsed` value and the previously computed `PowerGenerated` value are then used to update the stored battery energy as shown in Eq. (5.4):

$$E_{\text{new}} = E_{\text{prev}} - Power_{\text{used}} \Delta t + Power_{\text{gen}} \Delta t. \quad (5.4)$$

This value is converted to watt-hours for energy tracking. The battery energy is monitored between `MinEnergyBus` and `MaxEnergyStored` to prevent overcharge or depletion. This continuously updating process links subsystem activity, environmental conditions, and communication events to the spacecraft's overall energy balance. It provides a realistic assessment of power availability and consumption across illumination cycles, science intervals, and communication passes throughout the simulation.

5.6.11 Build Outputs

The **Build Outputs** procedure defines the graphical and data-reporting interfaces used to monitor spacecraft state, subsystem performance, and science conditions during the simulation. This routine creates and configures multiple *PlotWindow* and *DataTableWindow* objects, along with a text-based *ReportInterface* for exporting key variables to file.

At initialization, the procedure constructs a data table that tracks elapsed time, Sun and Earth eclipse status, and the prime science flag from the `TIME_KEEPING` structure. Several dedicated plot windows are then generated to visualize key simulation metrics, including eclipse and target visibility status, spacecraft altitude, power levels, and ground-station contact periods. Each plot window facilitates rapid review of mission behavior over the full simulation duration.

Power tracking plots combine generated power, battery energy, and depth of discharge variables from the `POWER_VARS` and `ENERGY_STORAGE` structures, providing a clear depiction of the spacecraft's energy balance through illuminated and eclipsed segments. Additional plots display the Sun-Moon-Earth vertex angle, eclipse status and duration, and prime science duration, allowing direct correlation between geometry and science performance.

Finally, the *ReportInterface* object formats and exports a customizable data array containing time history information to a comma-delimited text file for post-processing. These outputs enable both qualitative visualization of spacecraft dynamics within FreeFlyer and quantitative analysis of simulation results in external tools such as MATLAB or Excel. The **Build Outputs** routine serves as the primary interface between the dynamic simulation core and the downstream mission analysis workflow.

5.6.12 Step HADES and Write to File

The **Step HADES and Write to File** procedure serves as the primary simulation driver, controlling spacecraft propagation, subsystem updates, and data logging throughout the mission timeline. It sequentially executes all procedures developed in the preceding sections at each time step, maintaining consistency between the spacecraft's dynamic state and its operational subsystems.

At initialization, the routine instantiates the spacecraft using the initial Moon-centered Keplerian state. The procedure then specifies the propagation step size (20 s) and simulation duration (365 d) and opens a *ReportInterface* for data output.

During each iteration of the main loop, the procedure performs the following sequence:

1. **Synchronize epochs:** Update the epochs of all vector objects to the current spacecraft epoch to ensure geometric consistency.
2. **Compute eclipse and visibility states:** Calls the subroutines *EclipseCalcs* to determine Earth, Sun, and dual-eclipse conditions, and *GSContact* to evaluate ground-station visibility.
3. **Subsystem updates:** Invoke the procedures **Power Generation** and **Power Consumption** to compute electrical balance and update stored energy.
4. **Attitude control logic:** Select the appropriate attitude mode. When the Sun is visible, HADES slews toward the Sun for power generation; otherwise, it slews toward the science target for data collection. The **Set Slew Rate** routine computes the required body angular velocity for each transition.
5. **Visualization and output update:** Refresh active plot windows and vector objects for real-time monitoring.
6. **Data reporting:** Populate the *arrDataOutput* array with elapsed time, eclipse durations, science flags, orbital elements, and subsystem metrics. Write the array to the FreeFlyer console and to an external report via the *ReportInterface* object.

At the end of each loop iteration, select data-reporting variables within TIME_KEEPING are reset, and the spacecraft state is advanced one step with the “Step” command. Error trapping ensures that propagation halts gracefully if numerical or logical errors occur, with a `crashFlag` recorded in the data output.

This continuously running procedure forms the backbone of the simulation, integrating orbital mechanics, attitude control, visibility logic, and subsystem modeling into a single time-stepped architecture. The structured data output enables direct post-processing in MATLAB or other analysis tools, supporting evaluation of orbital stability, science-time statistics, and subsystem performance over the full simulated mission duration.

Chapter 6

Orbit Selection Analysis

Using the simulation tools developed in Chapter 5, the HADES science-orbit design process began with a broad survey of the solution space to identify and down-select the most promising candidates. First, a constant-SMA sweep was performed to isolate performance trends, revealing a near-equatorial corridor with strong yearly science yield. A coupled $a-e$ sweep then refined the design by controlling periapsis while sampling (i, ω) within this favorable geometry. A composite score, QFOscore, balanced PrimeScienceTimeB with bounding metrics to identify quasi-frozen candidates. Based on this analysis, a final initial condition was selected for the detailed HADES simulations.

6.1 Constant-SMA Preliminary Design-Space Sweep

In the first phase, a broad preliminary design sweep mapped the landscape of possible orbits by holding the semi-major axis constant and varying other orbital elements over wide ranges. The SMA was fixed at $a = 1831$ km, corresponding roughly to a 94 km circular lunar orbit (a low orbit near the verge of the 100 km altitude limit). This value was chosen so that even at the highest eccentricities considered, the periapsis would not drop below approximately 30 km altitude, providing a buffer above the lunar terrain. With the semi-major axis a and inclination i fixed, the eccentricity e and argument of periapsis ω were then varied, along with a single representative true anomaly. Figure 6.1 illustrates the parameterization of the preliminary design-space sweep grid.

Inclination sweep. A sweep of the inclination was performed for $i = 0$ to 30° in 0.1° increments. This resolution maps broad trends and captures the sensitive low-inclination band where science access and lifetime change rapidly.

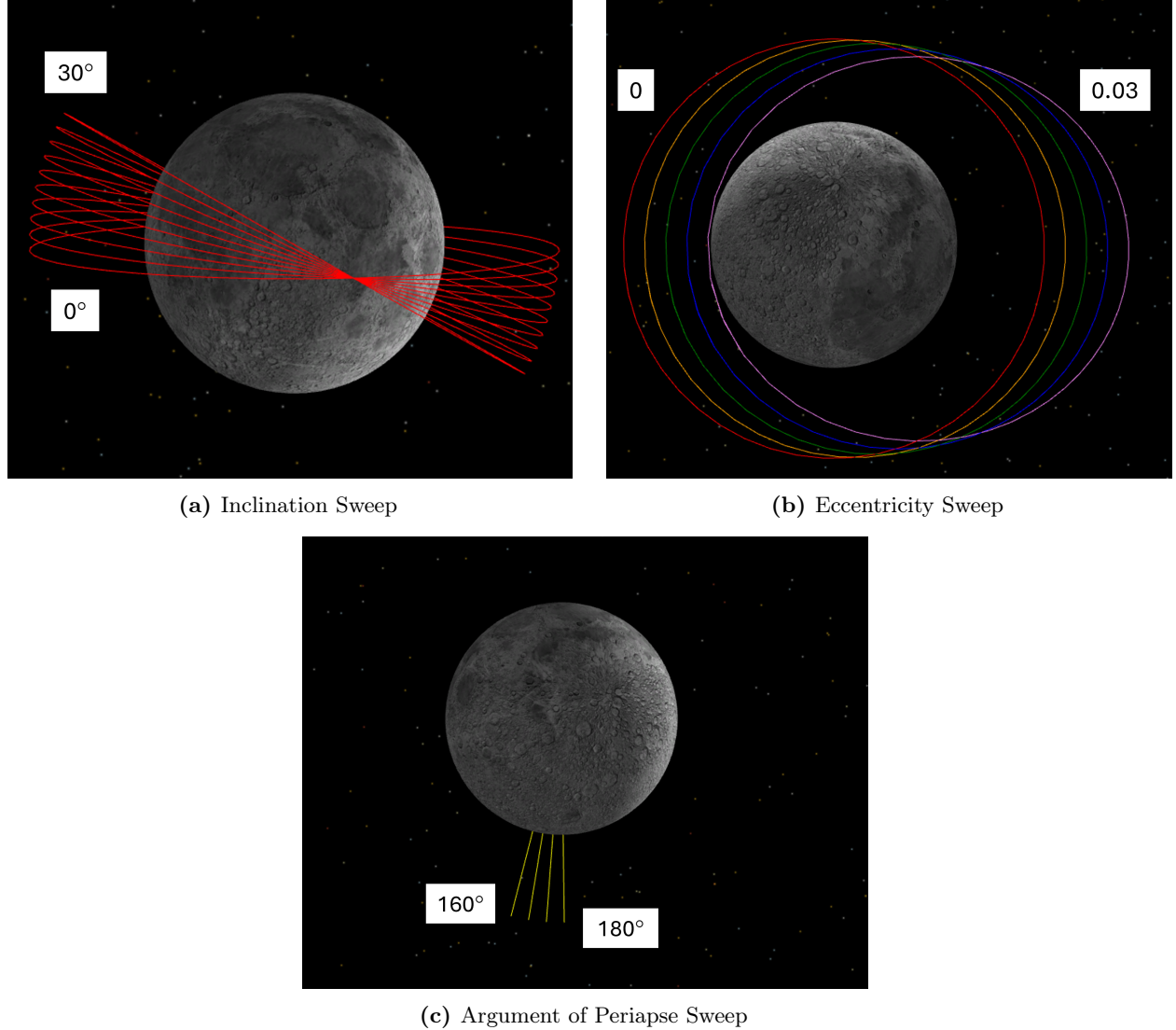


Figure 6.1: Visualization of constant-SMA parameter sweep at $a = 1831$ km.

(a) Inclination sweep from 0° to 30° in 0.1° increments, showing the increasing tilt of the orbital plane relative to the lunar equator. (b) Eccentricity sweep from $e = 0$ to $e = 0.03$ in 0.005 increments at fixed a , illustrating the transition from circular to mildly elliptical orbits. (c) Argument-of-periapsis sweep from $\omega = 160^\circ$ to $\omega = 180^\circ$ in 5° increments, rotating the line of apsides to sample different periapsis longitudes in the mascon field. Panels are schematic and depict the grid geometry rather than the full propagated set of trajectories.

Eccentricity sweep. A sweep of the eccentricity was performed for $e = 0$ to 0.03 in 0.005 steps. At $a = 1831$ km, $e \approx 0.03$ places periselene near 30 km altitude and keeps apolune below 160 km. Higher eccentricities were avoided to prevent periapsis from dipping into extremely low altitudes or degrading orbit stability.

Argument of periapsis. Finally, a sweep of the argument of periapsis was performed for $\omega = 160$ to 180° in 5° steps. Varying ω exposes how lunar longitude governs dual-eclipse alignment and decay behavior.

Each combination of (i, e, ω) was propagated for 365 d with the full force model and simulation logic described in Chapter 5. In total, 12 040 distinct orbit cases were simulated in this coarse sweep. The outcome of this constant- a preliminary design search was a “Skittles plot” of yearly PrimeScienceTimeB yield across the inclination–eccentricity–AOP grid (Fig. 6.2).

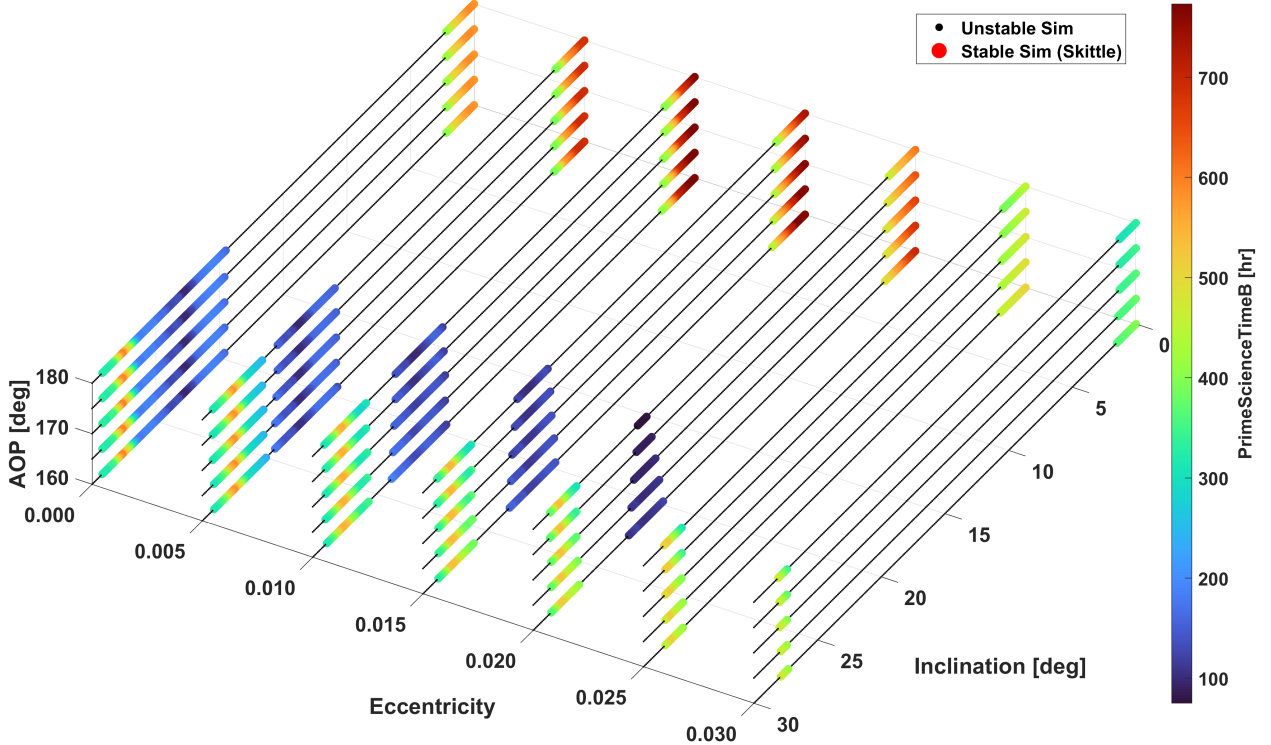


Figure 6.2: Skittles plot of the constant-SMA preliminary design sweep at $a = 1831$ km.

Each colored marker corresponds to a one-year propagation at a unique (i, e, ω) . The axes show inclination, eccentricity, and argument of periapsis. Color encodes PrimeScienceTimeB [h], accumulated only during dual-eclipse intervals that satisfy LOS to the target, altitude $h < 100$ km, and dwell time ≥ 20 min. Colored markers denote runs that survived the full year (stable), while black points denote runs that impacted the lunar surface before one year (unstable).

To better understand the characteristics of the most effective orbits in this sweep, Table 6.1 lists the top 10 performers ranked by total PrimeScienceTimeB. These cases all satisfy the dual-eclipse and pointing criteria for extended durations and provide a basis for comparison in subsequent analysis.

Table 6.1: Top 10 preliminary design–space sweep configurations ranked by PrimeScienceTimeB. All configurations in this set have RAAN = 0° and TA = 0°.

Rank	SMA [km]	e	i [deg]	AOP [deg]	Prime- ScienceTimeB [h]	t_{560} [d]	Alt Min [km]	Alt Max [km]
1	1831	0.010	0.30	160	773.26	289.43	38.8	146.8
2	1831	0.010	0.40	160	772.97	289.51	38.4	147.2
3	1831	0.010	0.50	165	772.33	289.57	37.6	147.8
4	1831	0.015	0.80	160	771.96	289.34	37.2	148.3
5	1831	0.010	0.30	165	771.61	289.65	38.5	146.9
6	1831	0.010	0.40	170	771.48	289.62	37.5	147.7
7	1831	0.010	0.30	170	771.37	289.62	37.9	147.3
8	1831	0.010	0.20	170	770.94	289.62	38.3	146.9
9	1831	0.015	0.70	160	770.93	289.59	38.4	147.2
10	1831	0.010	0.40	165	770.88	289.73	38.1	147.4

The top-performing orbits in Table 6.1 confirmed the strong preference for near-equatorial, low-eccentricity geometries. All entries feature inclinations $i \leq 0.80^\circ$ and fall into only two eccentricity families, $e = 0.010$ and $e = 0.015$. PrimeScienceTimeB is essentially tied across the list, ranging from 770.88 to 773.26 h, a spread of about 2.4 h, which is under 0.40 %. The time required to accumulate 560 h of PrimeScienceTimeB is similarly tight at 289.34 to 289.73 d. These results indicate that within this low- i , moderate- e corridor, total science accrual is robust. The consistency in science yield and periapsis clearance across these entries also supports their suitability as quasi-frozen-orbit candidates for follow-on refinement. Overall, this broad first-phase analysis provided critical insight into the viable design space and pointed toward a narrow “sweet spot” in orbital parameters for further targeted exploration.

6.2 Refining the Design Space with a Coupled Sweep

The corridors identified in §6.1 were refined by coupling the semi-major axis a and eccentricity e along a near-constant-perilune path. Prime science occurs below 100 km near perilune, so comparing cases with drifting perilune would confound the score. Holding the low-altitude geometry nearly fixed isolated how the rest of the element set, especially e and ω , shaped long-arc behavior in the mascon field and the cadence of dual-eclipse intervals.

Independent scans in a and e change the periapsis radius according to

$$r_p = a(1 - e). \quad (6.1)$$

This change alters the altitude, duration, and timing of low-altitude passes, which muddies any comparison of science yield and speed to 560 h. A coupled rule kept r_p nearly constant, so the differences observed across the set reflected dynamics rather than a moving science floor. This produced fairer rankings and exposed a narrow ridge in the $\{e, \omega\}$ plane that preserved periapsis safety while increasing access to the radio-quiet geometry.

Starting from the periapsis relation and taking a small-step difference,

$$r_p = a(1 - e) \Rightarrow \Delta r_p \approx (1 - e)\Delta a - a\Delta e, \quad (6.2)$$

so that

$$\Delta e \approx \frac{(1 - e)\Delta a - \Delta r_p}{a}. \quad (6.3)$$

Using an initial $a = 1831$ km and $e = 0.00961$, a relatively small $\Delta a = +2.2$ km and gently rising $\Delta r_p = +0.66$ km were chosen, which gave

$$\Delta e \approx \frac{(1 - 0.00961) \cdot 2.2 - 0.66}{1831} \approx 8.30 \times 10^{-4} \quad (6.4)$$

per step. This kept perilune nearly constant across the sweep. Tables 6.2 and 6.3 show the a - e couplings and the remaining orbital elements and their parameterization used in the sweep.

Table 6.2: Coupled (a, e) pairs used for the coupled sweep.

Pair	a [km]	e
1	1831	0.00961
2	1833.2	0.01044
3	1835.4	0.01127
4	1837.6	0.01211
5	1839.8	0.01294

Table 6.3: Parameterization used for the coupled sweep.

Element	Symbol	Values / Range	Step	Count
Semi-major axis, eccentricity (coupled)	(a, e)	Five paired values (Table 6.2)	—	5
Inclination	i	0 to 2.50°	0.01°	251
Argument of periapsis	ω	120 to 240°	5°	25
RAAN	Ω	0°	fixed	1
True anomaly	ν	0°	fixed	1

For completeness, the higher-inclination band from the preliminary design-space map was examined. The best cases in that region delivered PrimeScienceTimeB in the range of about 570 to 590 h, with 560 h typically attained on day 346 to 349. Headroom above the 560 h requirement was only a few percent. Given the late time-to-goal, smaller robustness, and added sampling burden, the 24 to 30° band was not carried into the coupled refinement. The coupled sweep focused on the low-inclination family, $i \in [0^\circ, 2.50^\circ]$, where yield is higher, time-to-560 h is earlier, and behavior is less sensitive to small phase changes.

The combination of the five coupled pairs and angular grids produced 31 375 simulations, each propagated for 365 d with the same force model and logic as the preliminary design-space sweep. Figure 6.3 presents the coupled sweep Skittles plot of PrimeScienceTimeB.

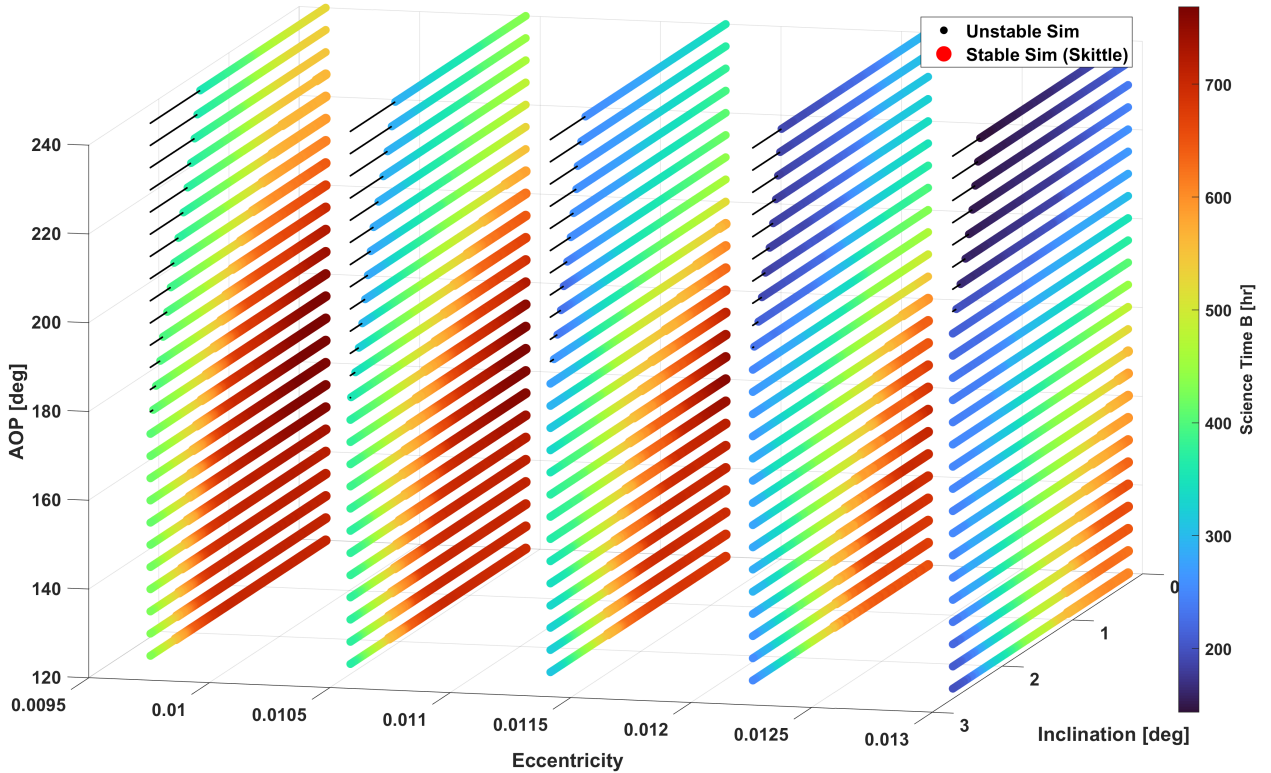


Figure 6.3: Skittles plot of the coupled sweep with five (a, e) pairs chosen to keep periapsis nearly constant. Each colored marker corresponds to a one-year propagation at a unique $\{a, e, i, \omega\}$ drawn from these pairs. Axes show inclination i , eccentricity e , and argument of periapsis ω . Sampling uses i at 0.01° steps and ω at 5° steps, with Ω and ν fixed. Color encodes PrimeScienceTimeB [h], accumulated only during dual eclipse with LOS to the target, altitude $h < 100$ km, and dwell time at least 20 min. Colored markers denote runs that survived the full year (stable). Black points denote runs that impacted before one year (unstable).

Table 6.4 lists the ten best coupled cases. All winners sit at $a = 1831$ km and $e = 0.00961$, with i between 0.10° and 0.42° and $\omega = 160^\circ$ or 165° at $\Omega = 0^\circ$. PrimeScienceTimeB spans 768.03 to 768.62 h, a spread of only 0.59 h. The 560 h milestone occurs between day 289.97 and day 290.14, a 0.17 d window. Perilune and apolune remain tightly bounded, with $h_{p,\min}$ between 37.5 km and 38.6 km and $h_{a,\max}$ between 146.9 km and 148.1 km.

This analysis resulted in two findings. First, the top-performing corridor is flat and robust. Small changes in i within 0.10 to 0.40° or switching ω between 160° and 165° do not materially change science yield or timeliness. Second, these orbits provide large margins: the best case delivered $768.6 - 560 \approx 208.6$ h above the requirement (about 37 %) and reached the threshold near day 290, roughly two months earlier than the 24 to 30° preliminary design-sweep band. This combination of high yield, early attainment, and tight altitude bounds established the low-inclination coupled corridor as the primary candidate for the final science-orbit design.

Table 6.4: Top 10 coupled sweep configurations ranked by PrimeScienceTimeB.
All configurations in this set have RAAN = 0° and TA = 0° .

Rank	SMA [km]	e	i [deg]	AOP [deg]	Prime- ScienceTimeB [h]	t_{560} [d]	Alt Min [km]	Alt Max [km]
1	1831	0.00961	0.32	165	768.62	289.97	37.7	147.8
2	1831	0.00961	0.41	160	768.62	289.99	37.6	148
3	1831	0.00961	0.31	165	768.49	290.06	37.7	147.7
4	1831	0.00961	0.39	160	768.42	290.08	37.7	147.9
5	1831	0.00961	0.28	165	768.20	290.06	37.8	147.6
6	1831	0.00961	0.42	160	768.15	290.08	37.5	148.1
7	1831	0.00961	0.27	165	768.07	290.06	37.9	147.5
8	1831	0.00961	0.40	160	768.07	290.08	37.6	148
9	1831	0.00961	0.10	165	768.04	290.14	38.6	146.9
10	1831	0.00961	0.30	165	768.03	290.06	37.8	147.7

6.3 Quasi-Frozen Orbit Candidate Selection and Scoring

The coupled sweep identified a narrow family of near-equatorial, mildly eccentric orbits that deliver high science yield and robust dual-eclipse access. Within that family, candidate QFOs must also exhibit bounded eccentricity and altitude envelopes over the full year. This section defines the metrics used to characterize boundedness, the feasibility gates applied to the coupled cohort, the anchored normalization, and the composite QFOscore used for ranking. The section concludes with a comparison of QFOscore-based and science-only rankings and the selection of a final HADES design orbit.

6.3.1 Derived metrics

For each one-year propagation that does not impact the lunar surface, the simulation recorded yearly extrema in altitude and eccentricity, the initial osculating eccentricity, and the accumulated PrimeScienceTimeB. The following derived quantities were used:

$$\text{SciHr} = \frac{\text{PrimeScienceTimeB}}{60}, \quad \text{PrimeScienceTimeB yield in hours,} \quad (6.5)$$

$$\Delta h = h_{\max} - h_{\min}, \quad \text{altitude span over the year [km],} \quad (6.6)$$

$$\Delta e = e_{\max} - e_{\min}, \quad \text{eccentricity envelope size,} \quad (6.7)$$

$$e_{\text{mid}} = \frac{e_{\max} + e_{\min}}{2}, \quad \text{mid-value of the eccentricity envelope,} \quad (6.8)$$

$$\text{DriftIdx} = \frac{|e_0 - e_{\text{mid}}|}{\Delta e / 2}, \quad \text{centeredness metric in eccentricity space.} \quad (6.9)$$

Here e_0 is the initial osculating eccentricity, and h_{\min} and h_{\max} are the minimum and maximum altitudes over the year. Smaller Δh and Δe indicate tighter, more stable envelopes. DriftIdx values near zero indicate that the starting point lies close to the middle of its natural oscillation envelope, which is desirable for quasi-frozen behavior.

6.3.2 Feasibility gates and periapsis proxies

A feasibility mask was used to remove cases that did not satisfy operational limits before any ranking was applied. The mask used in this study enforced:

- one-year survival with no lunar impact within 365 days;
- a low-inclination band appropriate to the near-equatorial family;
- a minimum science floor on SciHr; and
- periapsis geometry checks based on conservative proxies.

Two altitude-based quantities were evaluated for periapsis safety:

- the worst-case periapsis clearance over the year, $h_{p,\min}$ [km];
- a proxy for periapsis swing, taken as the altitude span Δh [km].

Selection requires that $h_{p,\min}$ be above a specified safety altitude and Δh below an upper bound. The QFO ranking window uses inclinations $i \in [0.30^\circ, 0.60^\circ]$, where the dual-eclipse geometry is strong and the near-equatorial family is well represented. These filters removed clearly unsuitable cases before weighting and scoring.

6.3.3 Anchored normalization

Heterogeneous metrics were mapped to unitless scores using fixed anchors. The use of anchored scaling avoided cohort dependence and kept scores comparable when the candidate window changed. For a generic metric x with lower and upper anchors x_{\min} and x_{\max} , the anchored value is

$$z_x = \text{sat}_{[0,1]} \left(\frac{x - x_{\min}}{x_{\max} - x_{\min}} \right), \quad (6.10)$$

where $\text{sat}_{[0,1]}(\cdot)$ clips the result into the interval $[0, 1]$.

For this study the anchors were chosen as fixed lower and upper bounds for each metric,

$$\begin{aligned} \text{SciHr}_{\min} &= 560 \text{ h}, & \text{SciHr}_{\max} &= 780 \text{ h}, \\ (\Delta e)_{\min} &= 0, & (\Delta e)_{\max} &= 0.030, \\ (\Delta h)_{\min} &= 80 \text{ km}, & (\Delta h)_{\max} &= 240 \text{ km}, \\ \text{DriftIdx}_{\min} &= 0, & \text{DriftIdx}_{\max} &= 1. \end{aligned}$$

These anchors were applied in Eq. (6.10) to compute the raw anchored scores z_{Sci} , $z_{\Delta e}$, $z_{\Delta h}$, and z_{Drift} .

For “smaller is better” quantities (Δe , Δh , DriftIdx), the anchored value was inverted after scaling so that larger z always corresponds to a more desirable outcome:

$$z_x^{\text{inv}} = 1 - z_x. \quad (6.11)$$

Anchor health was also checked by inspecting the fraction of z values that clip at 0 or 1. Light clipping is acceptable and indicates well-chosen anchors. Heavy clipping suggests that anchors are too tight or too loose and would require adjustment.

6.3.4 Composite QFOscore

The composite QFOscore emphasizes accumulated science time, then the tightness of the eccentricity envelope, then the altitude span, with a smaller weight on centeredness. The weights were fixed for the study and did not depend on the candidate set:

$$\text{QFOscore} = 0.45 z_{\text{Sci}} + 0.25 z_{\Delta e}^{\text{inv}} + 0.20 z_{\Delta h}^{\text{inv}} + 0.10 z_{\text{Drift}}^{\text{inv}}. \quad (6.12)$$

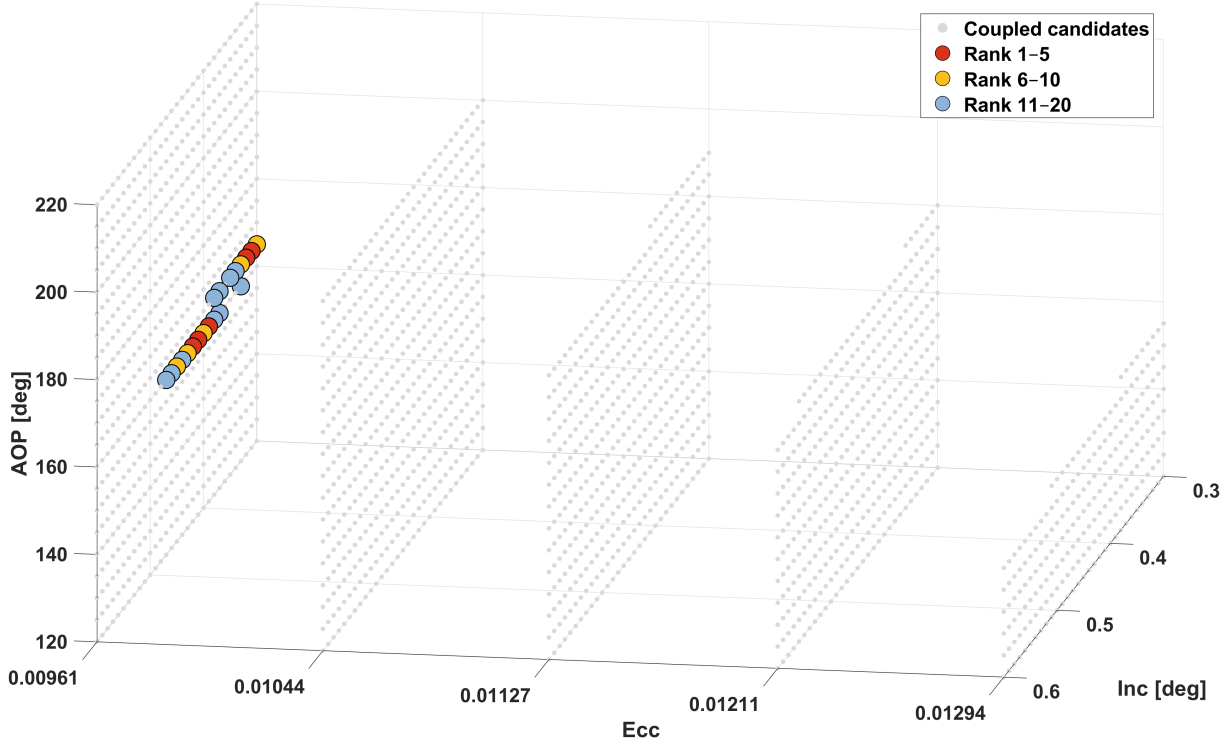
QFOscore is a relative figure of merit rather than a hard requirement. It represents a multi-criteria trade-study scalar built to rank candidates that appear quasi-frozen. The construction follows standard systems-engineering practice: evaluation criteria are selected and tied to mission value and dynamical behavior, normalized to a common scale, then combined with explicit weights so that the ranking reflects priorities.

Table 6.5 reports the Top 10 coupled-sweep configurations when ranked by QFOscore together with the envelope metrics that drive the score. These cases all satisfy the survival and periapsis safety gates and lie within the chosen inclination window.

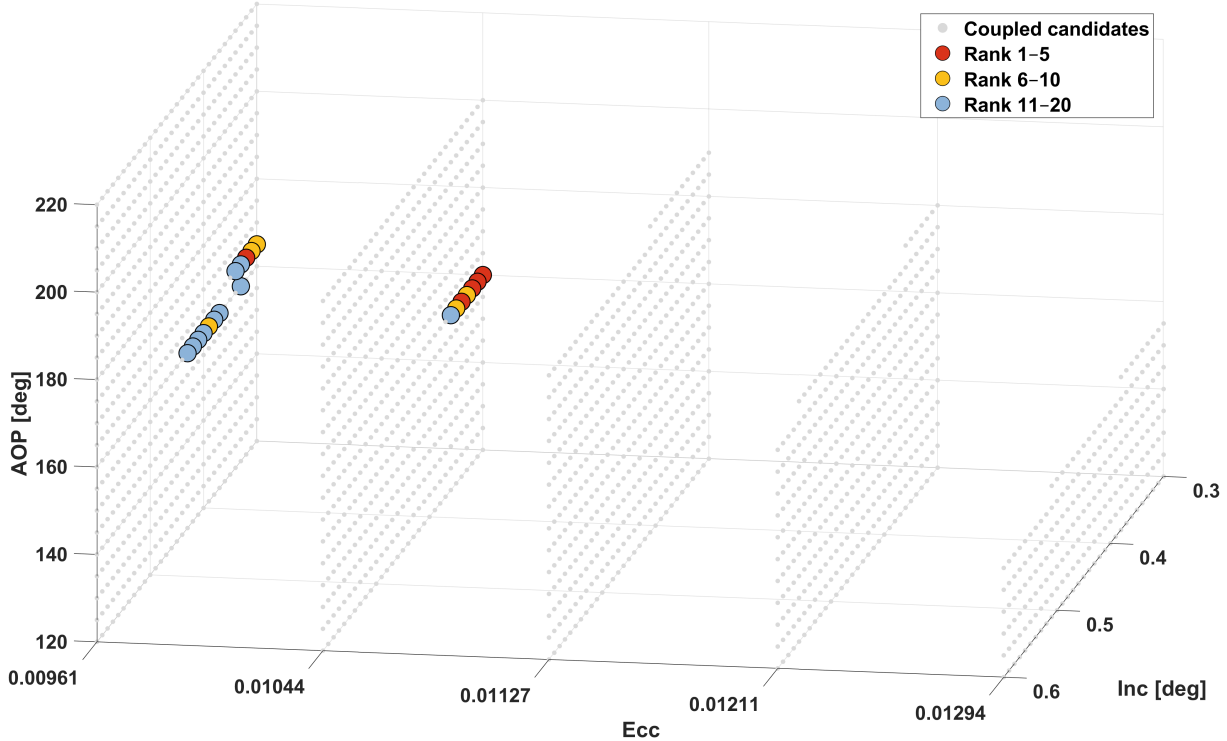
Table 6.5: Top 10 coupled-sweep configurations ranked by QFOscore (anchored metrics). All configurations in this set have RAAN = 0° and TA = 0°.

Rank	SMA [km]	e	i [deg]	ω [deg]	Prime ScienceTimeB [h]	Δe	Δh [km]	DriftIdx	QFOscore
1	1833.2	0.01044	0.30	160	759.99	0.02172	105.6	0.7498	0.75268
2	1833.2	0.01044	0.31	160	759.45	0.02177	105.7	0.7480	0.75135
3	1833.2	0.01044	0.32	160	758.92	0.02182	105.8	0.7461	0.75004
4	1831	0.00961	0.32	165	768.62	0.02377	110.1	0.7757	0.74928
5	1833.2	0.01044	0.34	160	758.78	0.02192	105.9	0.7424	0.74927
6	1833.2	0.01044	0.33	160	758.65	0.02187	105.8	0.7442	0.74925
7	1831	0.00961	0.31	165	768.49	0.02372	110	0.7778	0.74923
8	1831	0.00961	0.30	165	768.03	0.02366	109.9	0.7799	0.74850
9	1833.2	0.01044	0.35	160	758.32	0.02198	106	0.7405	0.74809
10	1831	0.00961	0.39	160	768.42	0.02375	110.3	0.7819	0.74801

Figure 6.4 summarizes how the stability and science metrics carved out slightly different subsets of the same coupled design pool. The plots show where the Top 20 QFOscore and PrimeScienceTimeB solutions cluster in (i, e, ω) and where they begin to diverge, which sets up the overlap analysis in the next subsection.



(a) Top 20 coupled orbits ranked by PrimeScienceTimeB.



(b) Top 20 coupled orbits ranked by QFOscore.

Figure 6.4: Skittles plot of Top 20 rankings on the coupled cohort.

(a) Top 20 orbits ranked by PrimeScienceTimeB hours. (b) Top 20 orbits ranked by QFOscore. Each marker corresponds to an initial condition (i, e, ω) drawn from the coupled (a, e) grid with $i \in [0.30, 0.60]^\circ$, $\omega \in [120, 240]^\circ$, $\text{SciHr} \geq 560$ h, and one-year survival. Light gray points show all candidates in this pool. Colored skittles indicate the Top 20 within each criterion, binned by rank: 1–5 (red), 6–10 (yellow), and 11–20 (blue).

The time-ranked skittles in Fig. 6.4a clustered near a single eccentricity because PrimeScienceTimeB was dominated by dual-eclipse geometry once i and ω lay in the favorable band. Within this cohort, the dual-eclipse duty cycle peaked near one value of e , and small changes in e shifted window length and frequency enough to concentrate most of the Top 20 into that ridge. PrimeScienceTimeB therefore accumulated where eclipse cadence was maximal.

In contrast, the QFO-ranked skittles in Fig. 6.4b spread across multiple eccentricities because the score optimized a trade between PrimeScienceTimeB and a tight dynamical envelope ($\Delta e, \Delta h$), together with a small drift index z_{Drift} . These envelopes were set by how each (a, e) pair interacted with the mascon field and third-body forcing over a year, not only by eclipse cadence. In the coupled grid, each eccentricity mapped to a slightly different orbital period and gravity-gradient environment while holding h_p approximately constant, so local minima in Δe and Δh occurred at different e . The composite QFOScore therefore surfaced several stability ridges across the allowed eccentricity range, distributing its top solutions where boundedness was best and the science yield remains high.

The two Top 20 views demonstrate that QFOScore and PrimeScienceTimeB favor similar regions of the quasi-frozen corridor, yet they do not select exactly the same orbits. Several candidates appeared in both sets, while others were promoted by only one metric either for superior boundedness or for slightly higher dual-eclipse yield. Rather than choose between purely stability-ranked or purely science-ranked solutions, the next subsection constructs a combined design set from the union of the Top N QFOScore and PrimeScienceTimeB orbits. This union captures all high-performing candidates from both perspectives and provides a compact pool from which to select the final HADES reference orbit.

6.3.5 Combined Stability and Science Design Set

The skittle plots showed that QFOScore and PrimeScienceTimeB favor the same low-inclination corridor but do not select exactly the same orbits. To build a practical design pool, the two rankings were then combined. Table 6.6 lists every coupled case that appears in the Top 20 by PrimeScienceTimeB and/or in the Top 20 by QFOScore, for a total of 27 distinct orbits. Each row is one set of coupled initial conditions (a, e, i, ω) , with its science performance (PrimeScienceTimeB and t_{560}) and its long-term behavior ($\Delta e, \Delta h, \text{DriftIdx}$). The two rank columns report how each orbit fared under the two metrics. Rank SciB comes from sorting the full coupled grid by PrimeScienceTimeB alone. Rank QFO comes from sorting the same grid by the composite QFOScore.

Table 6.6: Top 20 union across criteria on the coupled cohort.

Blue-shaded cells highlight entries within the best five values for each metric (largest PrimeScienceTimeB; smallest t_{560} , Δe , Δh and DriftIdx), including ties.

Rank SciB	Rank QFO	SMA [km]	e	i [deg]	AOP [deg]	Prime- ScienceTimeB [h]	t_{560} [d]	Δe	Δh [km]	DriftIdx	QFOscore
–	1	1833.2	0.01044	0.30	160	759.99	290.93	0.02172	105.6	0.7498	0.75268
–	2	1833.2	0.01044	0.31	160	759.45	291.01	0.02177	105.7	0.7480	0.75135
–	3	1833.2	0.01044	0.32	160	758.92	291.09	0.02182	105.8	0.7461	0.75004
1	4	1831	0.00961	0.32	165	768.62	289.97	0.02377	110.1	0.7757	0.74928
–	5	1833.2	0.01044	0.34	160	758.78	291.17	0.02192	105.9	0.7424	0.74927
–	6	1833.2	0.01044	0.33	160	758.65	291.17	0.02187	105.8	0.7442	0.74925
3	7	1831	0.00961	0.31	165	768.49	290.06	0.02372	110	0.7778	0.74923
7	8	1831	0.00961	0.30	165	768.03	290.06	0.02366	109.9	0.7799	0.74850
–	9	1833.2	0.01044	0.35	160	758.32	291.17	0.02198	106	0.7405	0.74809
4	10	1831	0.00961	0.39	160	768.42	290.08	0.02375	110.3	0.7819	0.74801
2	11	1831	0.00961	0.41	160	768.62	289.99	0.02387	110.5	0.7775	0.74792
8	12	1831	0.00961	0.33	165	767.92	290.14	0.02383	110.2	0.7737	0.74762
14	13	1831	0.00961	0.33	160	767.32	290.24	0.02340	109.7	0.7952	0.74713
6	14	1831	0.00961	0.40	160	768.07	290.08	0.02381	110.4	0.7797	0.74704
5	15	1831	0.00961	0.42	160	768.15	290.08	0.02393	110.6	0.7753	0.74671
–	16	1833.2	0.01044	0.36	160	757.57	291.33	0.02203	106.1	0.7387	0.74631
12	17	1831	0.00961	0.38	160	767.41	290.16	0.02369	110.2	0.7841	0.74617
15	18	1831	0.00961	0.37	160	767.22	290.24	0.02363	110.1	0.7863	0.74602
17	19	1831	0.00961	0.34	165	767.11	290.22	0.02388	110.3	0.7716	0.74574
10	20	1831	0.00961	0.43	160	767.62	290.16	0.02399	110.7	0.7731	0.74540
9	–	1831	0.00961	0.45	160	767.64	290.08	0.02410	110.9	0.7687	0.74493
11	–	1831	0.00961	0.44	160	767.51	290.16	0.02404	110.8	0.7709	0.74492
13	–	1831	0.00961	0.47	160	767.36	290.16	0.02422	111	0.7644	0.74384
16	–	1831	0.00961	0.46	160	767.15	290.16	0.02416	111	0.7665	0.74368
18	–	1831	0.00961	0.35	165	767.01	290.22	0.02394	110.3	0.7695	0.74530
19	–	1831	0.00961	0.38	165	766.85	290.22	0.02411	110.6	0.7634	0.74430
20	–	1831	0.00961	0.37	165	766.72	290.30	0.02405	110.5	0.7654	0.74426

Several structural features stand out in the union set. All solutions lie in a very narrow band in element space. SMA takes only two values, 1831 km and 1833.2 km, paired with eccentricities of either 0.00961 or 0.01044. Inclination stays between about 0.30° and 0.47° , and argument of periapsis toggles between 160° and 165° . Both ranking schemes therefore draw almost exclusively from a single low-inclination, slightly eccentric family near the frozen-orbit sweet spot identified earlier in the campaign, rather than sampling widely across the coupled grid.

Within that family, the table splits naturally into two sub-clusters. The $a = 1831$ km, $e = 0.00961$ group carries the highest science yield. These cases deliver roughly 767 to 769 h of PrimeScienceTimeB and reach the 560 h threshold in about 290 to 290.3 d. The $a = 1833.2$ km, $e = 0.01044$ group loses only about 1% of science time, with PrimeScienceTimeB around 758 to 760 h and t_{560} near 291 to 291.3 d, but shows noticeably smaller drift: Δe near 0.0217 to 0.0220 and Δh around 105.6 to 106.1 km, compared to $\Delta e \approx 0.0234$ to 0.0242 and $\Delta h \approx 109.7$ to 111 km for the 1831 km group. DriftIdx follows the same pattern, sitting near 0.74 to 0.75 for the higher-altitude group and closer to 0.77 to 0.80 for the lower-altitude one. QFOScore simply reflects that trade: the most favorable rows concentrate where drift is smallest while still retaining high PrimeScienceTimeB.

The rank pattern clarifies how the two metrics interact. Thirteen orbits appear in the Top 20 of both lists, so most stability-favored orbits are also among the very best science producers. The rows with “–” in **Rank SciB** are those that QFOScore pulls in purely for their stability advantages. They sit just outside the Top 20 in PrimeScienceTimeB but have the smallest Δe , Δh , and DriftIdx in the cohort, and they all belong to the 1833.2 km / 0.01044 cluster. The rows with “–” in **Rank QFO** are the opposite. They belong to the 1831 km / 0.00961 cluster and are extremely strong in raw science hours, usually in the 767 to 768 h range, but they sit at the upper end of the drift band and are therefore penalized in QFOScore.

Taken together, Table 6.6 showed that once the search was restricted to the low-inclination family with $a \in [1831, 1833.2]$ km and $e \approx 0.01$, the pure science metric became nearly flat. Across the union set, PrimeScienceTimeB varied by only a few percent and t_{560} stayed between about 290 d and 291.3 d. The dominant discriminator was the drift behavior, so QFOScore acted primarily as a stability filter on an already science-rich region. For mission design, the preferred solutions sit in the overlapping subset that combines near-maximum PrimeScienceTimeB with minimal Δe , Δh , and DriftIdx. Those orbits reduce long-term orbital degradation and propellant maintenance while still achieving the 560 h science quota within one year.

On this basis, the nominal HADES science orbit was taken from the overlapping subset of the union set: the QFOScore Rank 1 case that maintained a science yield within 1% of the theoretical maximum. This solution belongs to the higher-altitude branch of the coupled family and trades that small fraction of PrimeScienceTimeB for noticeably smaller Δe , Δh , and DriftIdx. Table 6.7 lists initial conditions at the design epoch.

Table 6.7: Initial Keplerian elements for the reference science orbit.

Semi-major axis a [km]	Eccentricity e	Inclination i [deg]	RAAN Ω [deg]	Argument of periapsis ω [deg]	True anomaly ν [deg]
1833.2	0.01044	0.30	0	160	0

6.4 Time-Domain Performance of the Selected Orbit

This section examines the one-year evolution and science timeline of the selected QFO under the full HADES simulation. The selected orbit belongs to the higher-altitude branch of the coupled family and trades about 1% of PrimeScienceTimeB for noticeably tighter envelopes in eccentricity and altitude. In the coupled design sweep of §6.2–6.3, propagated with a 60 s step, this case delivered approximately 760 h of Prime Science integration below 100 km, with $\Delta e = 0.02172$, $\Delta h = 105.60$ km, DriftIdx = 0.7498, and QFOscore = 0.7527 (Table 6.6). These metrics established the orbit as a top performer in terms of science yield and boundedness within the coupled family.

For the detailed time-domain analysis, the same initial conditions were repropagated for one year using the full HADES force and operations model at a finer 20 s integration step. The run covered 365 d and yielded 4484 completed revolutions, with a mean osculating period $\bar{T} \approx 117.2$ min that is consistent with the coupled solution at $a = 1833.2$ km. Each completed revolution was treated as a single orbit, so orbit counts and event rates in this section can be interpreted directly in units of orbits per year. Table 6.8 compares the key Prime Science and QFO metrics for this orbit at the two step sizes.

Table 6.8: Sensitivity of selected-orbit QFO metrics to integrator time step.

Run / metric	PrimeScienceTimeB [h]	Δe	Δh [km]	DriftIdx	QFOscore
60 s sweep	759.99	0.02172	105.6	0.7498	0.75268
20 s verification	741.49	0.02172	105.6	0.7500	0.71481
Relative change [%]	-2.43	-0.01	0	0.03	-5.03

The finer 20 s propagation reduced the counted PrimeScienceTimeB by about 18.5 h, a decrease of roughly 2.4 %. This change reflected slightly shorter Prime Science dwells once eclipse and pointing boundaries were resolved with higher temporal fidelity. The orbit-shape metrics were essentially unchanged: Δe and Δh differed by less than 0.01 % and the DriftIdx changed by only 0.03 %, which confirmed that the mascon-driven envelopes were insensitive to the step size used here. The composite QFOscore dropped from 0.75268 to 0.71481, a 5 % reduction that was driven almost entirely by the lower PrimeScienceTimeB value, but the orbit remained in the high-scoring region of the coupled family and still exceeded the 560 h requirement by more than 180 h. In the remainder of this section all reported values and time histories refer to the 20 s verification run.

To visualize the orbital envelopes directly, Fig. 6.5 shows the osculating eccentricity together with the corresponding apolune and perilune altitudes over the verification run. These time histories make it clear how the coupled orbit responds to the lunar mascon field while remaining within the bounds summarized by Δe and Δh .

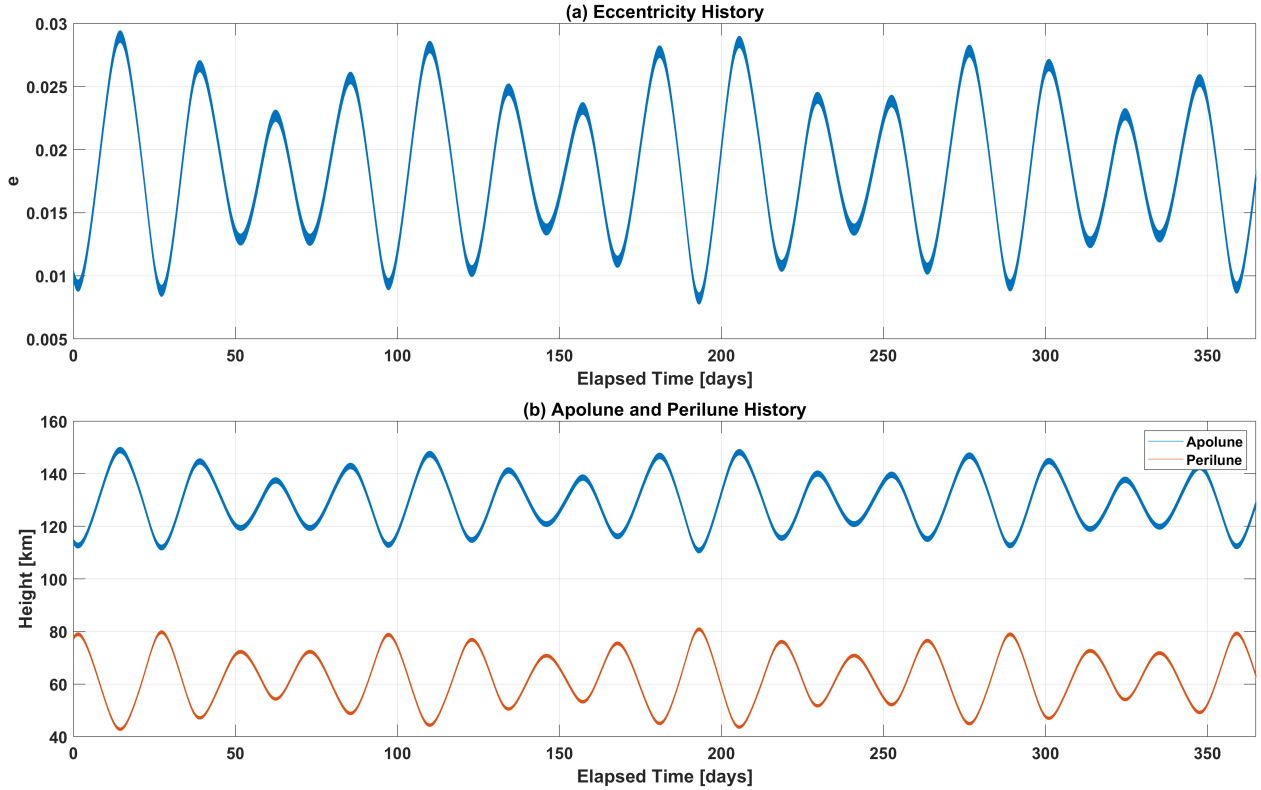


Figure 6.5: Eccentricity and altitude envelope of the selected science orbit over one year.

Panel (a) shows the osculating eccentricity history from the 20s verification run. Panel (b) shows the corresponding apolune and perilune altitudes. The orbit exhibits a bounded oscillatory pattern in e , which translates into paired variations of apolune between roughly 115 to 150 km and perilune between about 45 to 80 km.

The eccentricity in Panel (a) oscillates between about 0.008 and 0.029 with a characteristic period of roughly one synodic month. Panel (b) shows the associated variation in apolune and perilune altitude. Perilune remains between about 45 to 80 km, comfortably above the 35 km floor adopted in Chapter 4, while apolune stays between approximately 115 to 150 km. These extrema are consistent with the envelope values used to compute $\Delta e \approx 0.0217$ and $\Delta h \approx 105.6$ km. The absence of any secular trend in either periapsis or apoapsis altitude over the year supports the interpretation of this case as quasi-frozen within the design horizon.

To clarify the mechanism behind the bounded periapsis altitude, it is useful to examine the evolution of the eccentricity vector rather than only the scalar time history of e in Fig. 6.5. In a purely Keplerian problem, the eccentricity vector is constant: both the magnitude e and the argument of periapsis ω are fixed. In the lunar gravity field it undergoes a slow rotation and small amplitude oscillation due to the non-spherical potential. Figure 6.6 plots this behavior in the eccentricity vector phase space using the Cartesian components $e_x = e \cos \omega$ and $e_y = e \sin \omega$. In this representation, the circulating angle corresponds to the rotation of ω , while the distance from the origin tracks the instantaneous eccentricity.

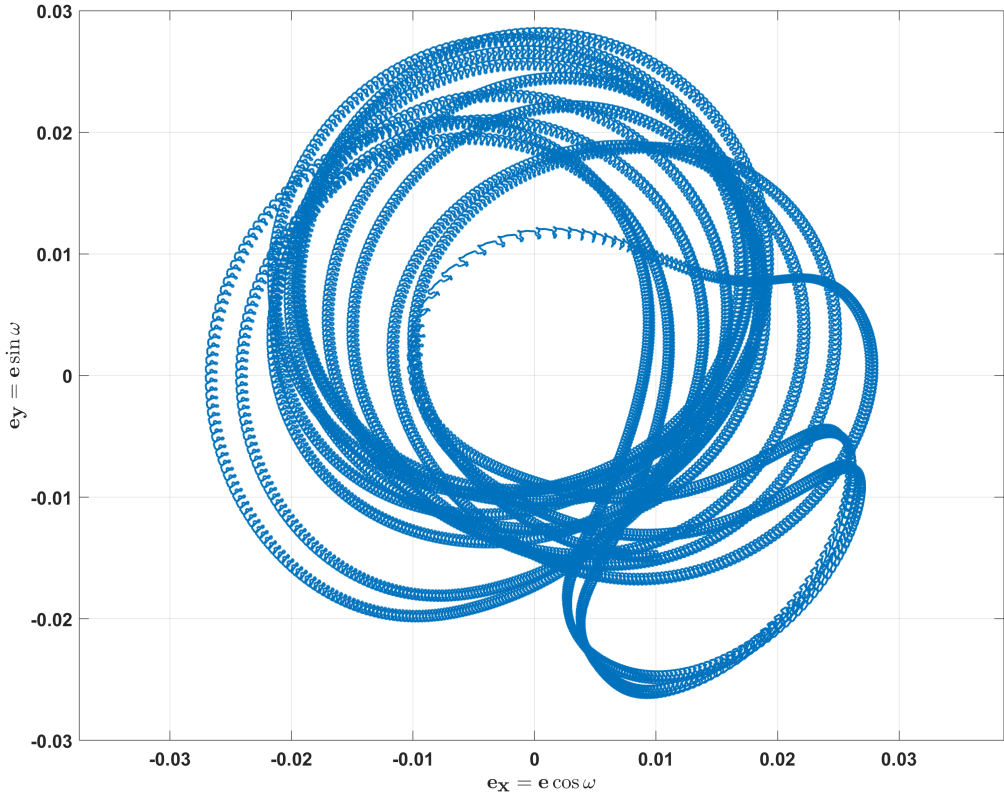


Figure 6.6: Eccentricity-vector portrait for the selected science orbit over one year.

The curve shows the time history of the components $e_x = e \cos \omega$ and $e_y = e \sin \omega$ over the full simulation. The trajectory occupies a compact annulus in the (e_x, e_y) plane, which indicates that the eccentricity vector precesses while its magnitude remains bounded, with no secular growth in e .

Consistent with the time history in Fig. 6.5, this radius oscillates between about $e \approx 0.008$ and $e \approx 0.029$ without any long term trend. This pattern is characteristic of quasi-periodic motion in a stable region of phase space. Because e remains bounded, the periapsis distance $r_p = a(1 - e)$ never drifts toward values that would intersect the lunar surface over the simulated mission duration.

6.4.1 Distribution of Prime Science Event Durations

Figure 6.7 summarizes the distribution of individual Prime Science intervals for the selected orbit.

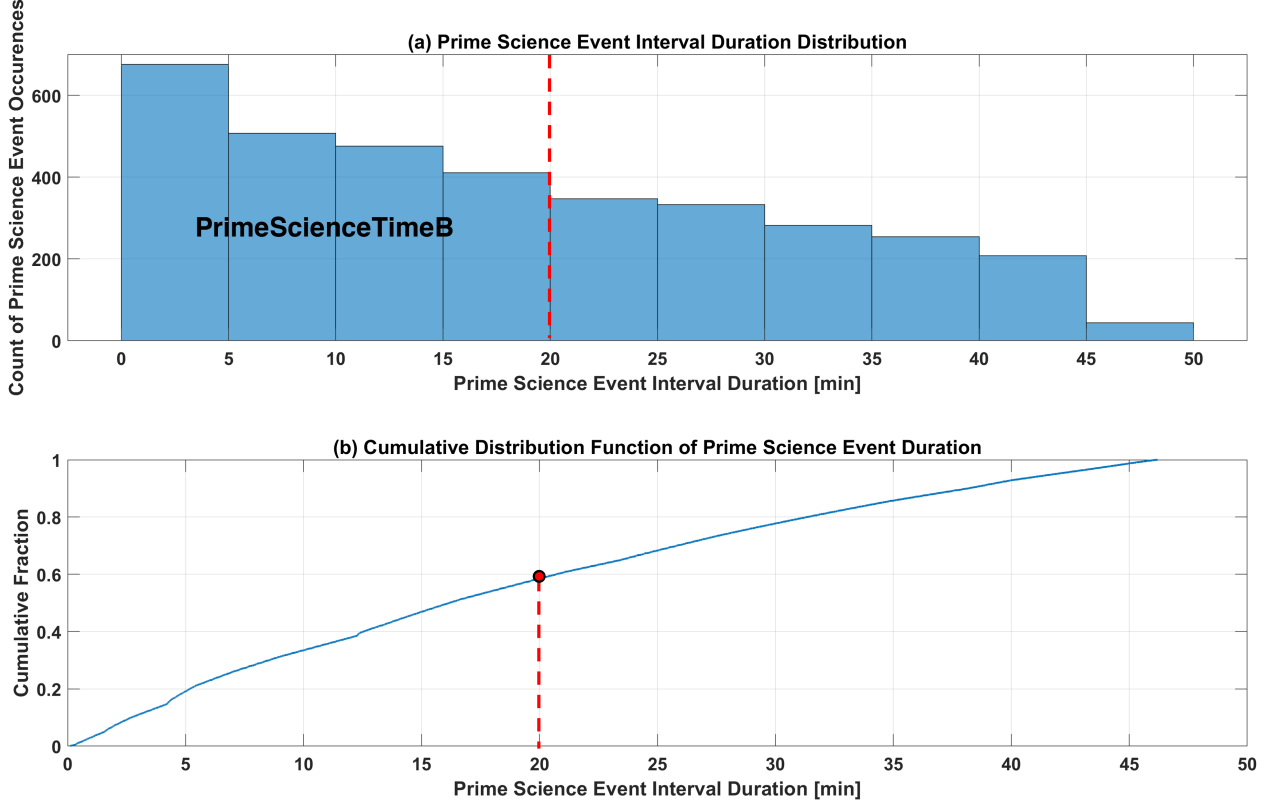


Figure 6.7: Prime Science dwell duration statistics for the selected science orbit.

Panel (a) shows a histogram of all Prime Science intervals from the one-year 20 s run, using 5 min-wide duration bins. The red dashed line marks the 20 min minimum dwell requirement. Panel (b) plots the corresponding cumulative distribution function. The red marker at 20 min indicates that about 60 % of all dual-eclipse opportunities are shorter than the requirement and do not contribute to PrimeScienceTimeB, while the remaining 40 % of longer dwells provide most of the usable integration time.

Panel (a) shows a histogram of Prime Science dwell durations from the one-year run. Intervals ranged from a few minutes up to nearly 50 min, with a clear peak at short durations and a right-skewed tail toward longer events. The red vertical dashed line marks the 20 min minimum dwell requirement for PrimeScienceTimeB.

Panel (b) plots the corresponding cumulative distribution function. At the 20 min threshold the CDF reached approximately 0.60, which means that about 60 % of all Prime Science opportunities were shorter than the required dwell time and therefore did not contribute directly to PrimeScienceTimeB. The remaining 40 % of events exceeded the requirement and formed the set of usable integration intervals. Although they were fewer in number, these longer dwells dominated the total integration time because each contributed

a larger block of continuous observation. The combination of a large population of short windows and a smaller population of long windows is important operationally: it implies frequent opportunities to verify instrument health and calibration, while still providing enough long dwells to close the PrimeScienceTimeB time requirement with margin.

6.4.2 Prime Science Event Cadence and Orbit Statistics

The QFO metrics in Table 6.8 show the selected coupled orbit provides a stable geometry with ample Prime Science margin over the design year. It is also useful to examine how that integration time is assembled in time. Figure 6.8 summarizes the one-year temporal behavior of the selected orbit in terms of lunar phase, individual Prime Science dwells, and cumulative PrimeScienceTimeB.

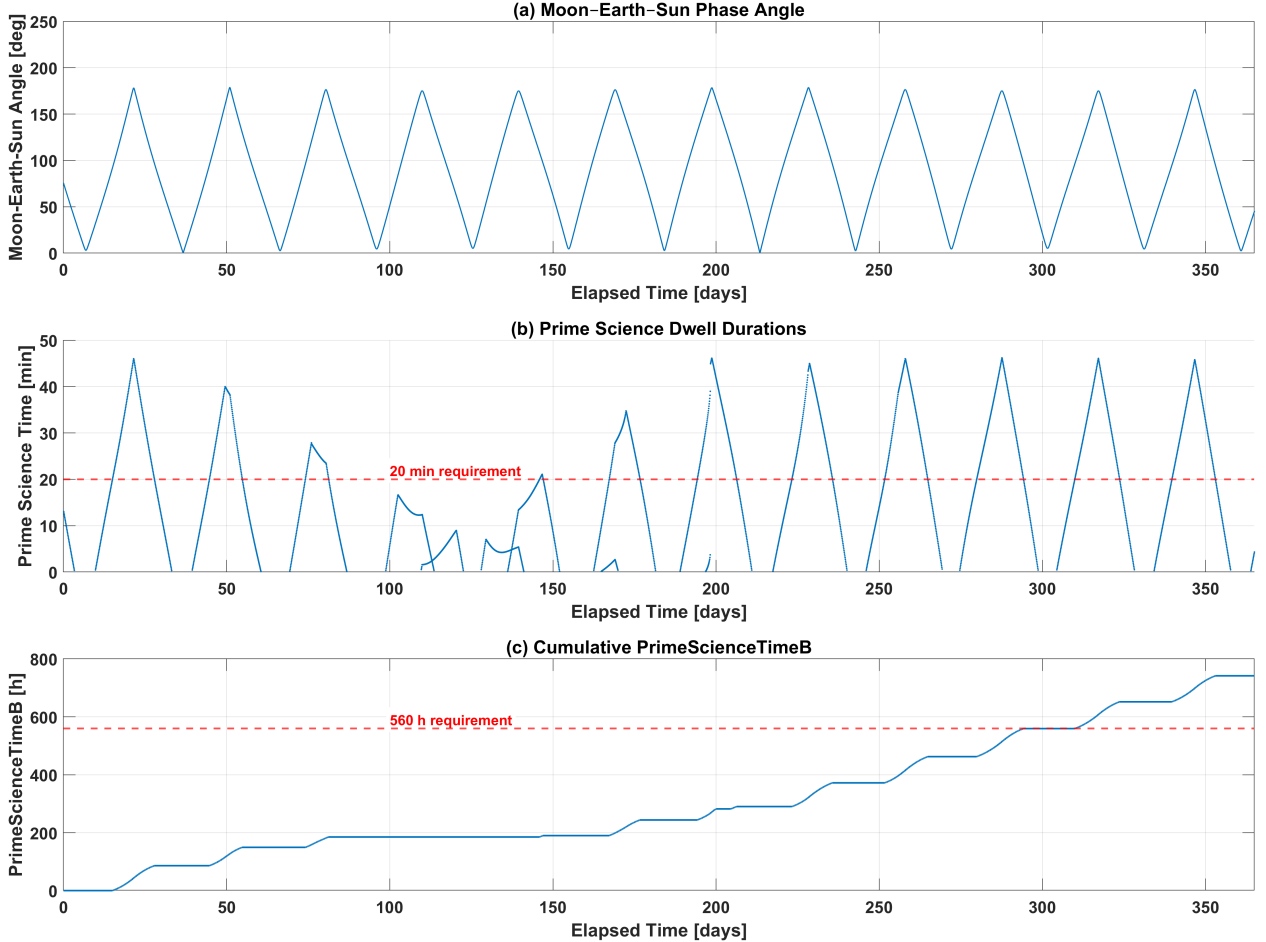


Figure 6.8: Time-domain view of Prime Science performance for the science orbit. Panel (a) shows the Moon–Earth–Sun phase angle as a function of elapsed time, with peaks near full Moon and valleys near new Moon. Panel (b) shows the duration of each Prime Science event in one year together with the 20 min dwell requirement. Panel (c) plots the cumulative PrimeScienceTimeB and highlights the 560 h requirement threshold, which is crossed near day 290 before the total climbs to about 741 h.

Panel (a) plots the Moon–Earth–Sun ($\angle MES$) phase angle. The $\angle MES$ angle follows the synodic cycle and oscillates between new Moon near 0° and full Moon near 180° . Prime Science is only possible when the spacecraft is on the lunar far side with both Earth and Sun occulted, so the peaks and valleys of this curve define the seasons in which the radio environment is quiet enough for Prime Science operations.

Panel (b) gives the duration of each Prime Science dwell as a function of elapsed time and shows the 20 min dwell requirement. Prime Science events form clusters in specific $\angle MES$ seasons where the orbit plane, the Earth–Sun line, and the fixed inertial target align favorably. During these seasons successive orbits often produced dwells that exceeded the requirement and occasionally reached 40 to 50 min. In other parts of the year the geometry only clips the quiet region, and available dwells are short or absent. The long gap in panel (b) near midyear illustrates such an unfavorable season, during which no qualifying Prime Science events occur.

Panel (c) shows the cumulative PrimeScienceTimeB. Each step corresponds to a dwell that satisfies all four mission conditions: far side geometry with Earth and Sun occulted, valid target LOS pointing, dwell duration of at least 20 min, and altitude below 100 km. The staircase grows rapidly during favorable MES seasons and remains flat when only short or no dwells are available. The 560 h requirement was met just before day 290, after which additional seasons increase the total to about 741 h. The time history confirmed that this orbit closes the Prime Science requirement with roughly 180 h of margin, even in the presence of extended intervals with little or no Prime Science B activity.

Table 6.9 recasts the same behavior in terms of discrete orbits and events. The verification run produced 4484 completed orbits. Of these, 3307 orbits (73.8 %) contained at least one Prime Science event, while 1449 orbits (32.3 %) contained at least one Prime Science B event that met the full dwell-time requirement. Almost all of the Prime Science B orbits hosted a single event (1430 cases), with only 19 orbits exhibiting two Prime Science B events. The simulation also recorded 231 consecutive dwell pairs within the same orbit, which occurred when the spacecraft traversed a long quiet-sky arc that was interrupted briefly by a pointing or altitude violation. Together, the time-domain plots and the orbit/event statistics show that the selected coupled orbit provides frequent but strongly seasonal Prime Science opportunities, with enough long dwells to accumulate the required integration time well within the one-year mission horizon.

These results confirm that the selected coupled orbit satisfies the Prime Science requirement with margin while remaining dynamically well behaved in the lunar mascon field over the nominal mission life. However, before formally adopting this trajectory as the design reference, its behavior must be characterized beyond the one-year science phase. A longer-term propagation is required to verify the permanence of the quasi-frozen state and to determine the necessity of active disposal maneuvers for planetary protection compliance.

Table 6.9: Prime Science orbit and event statistics.
Percentages are given relative to the 4484 simulated orbits.

Metric	Value	Comment
Total orbits simulated	4484	
Total Prime Science events (all Prime Science intervals)	3538	events
Orbits with ≥ 1 Prime Science event	3307	73.8 % of orbits
Orbits with ≥ 1 Prime Science B event	1449	32.3 % of orbits
<i>Prime Science events per orbit</i>		
Orbits with exactly 1 event	3078	68.64 % of orbits
Orbits with exactly 2 events	227	5.06 % of orbits
Orbits with exactly 3 events	2	0.04 % of orbits
<i>Prime Science B events per orbit</i>		
Orbits with exactly 1 B event	1430	31.89 % of orbits
Orbits with exactly 2 B events	19	0.42 % of orbits
Orbits with exactly 3 B events	0	0 % of orbits
Number of consecutive dwell pairs in the same orbit	231	pairs

6.5 Extended Long-Term Stability Assessment

While the primary HADES mission requirements specify a one-year operational lifetime (365 days), characterizing the trajectory’s long-term behavior is critical for two reasons. First, it validates the “quasi-frozen” nature of the selected orbit, confirming that the bounded behavior observed in the first year is a stable dynamical feature rather than a transient state preceding a crash. Second, it informs planetary protection and disposal strategies; if the orbit is naturally stable, the spacecraft will not passively deorbit within a reasonable timeframe, necessitating the active disposal maneuver defined in the Concept of Operations.

To assess this stability, the verification simulation from § 6.4 was extended to a continuous three-year duration (1095 days). The propagation utilized the same high-fidelity force model, including the GRAIL GL0660B gravity potential truncated to degree and order 70, point-mass third-body perturbations from the Earth and Sun, and solar radiation pressure, with no station-keeping maneuvers applied.

Stability of Orbital Elements

The evolution of the osculating eccentricity and altitude extrema over the three-year period is presented in Fig. 6.9. The results confirm that the selected design orbit resides in a deep stability region of the phase space.

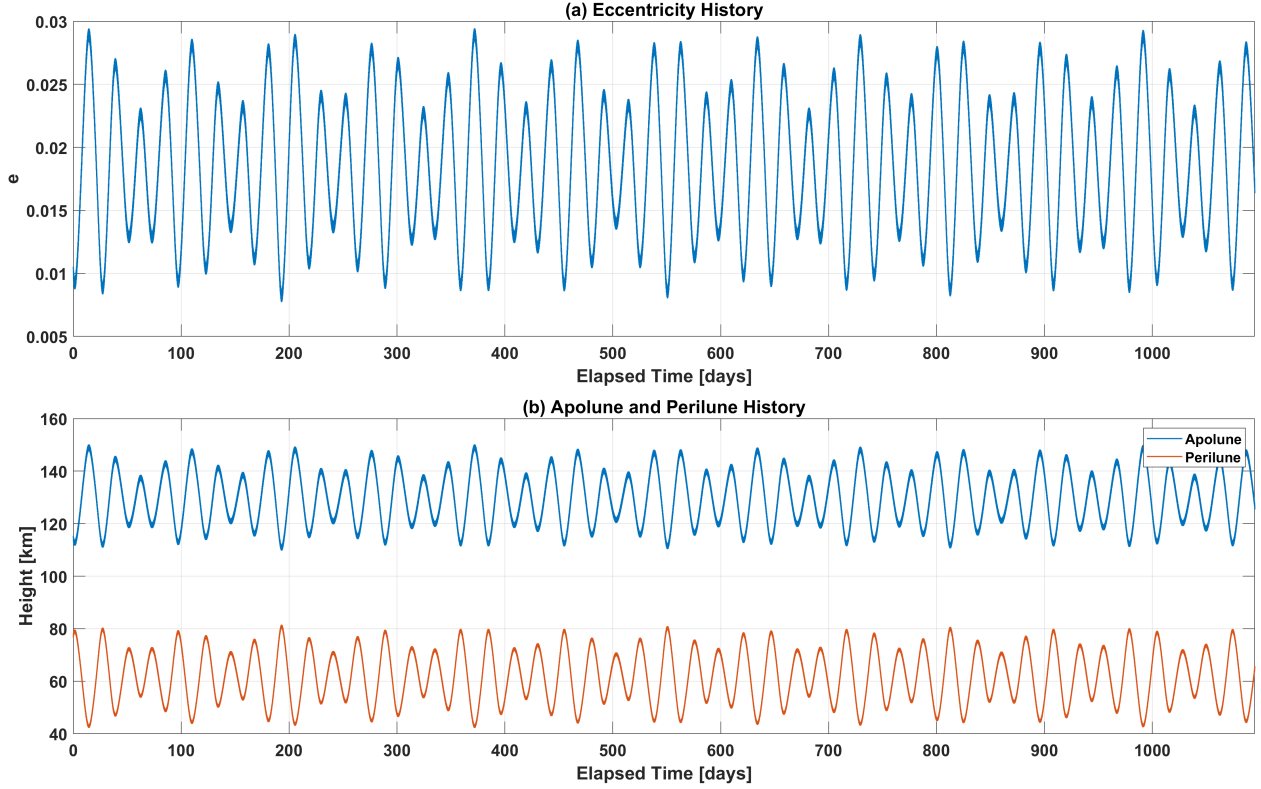


Figure 6.9: Three-year eccentricity and altitude envelope of the adopted HADES science orbit. Panel (a) shows the eccentricity history. Panel (b) shows the corresponding apolune and perilune altitudes. The behavior is qualitatively similar to the one-year result in Fig. 6.5, but extended over a three-year interval.

Eccentricity Evolution: As shown in Panel (a), the eccentricity exhibits a bounded, quasi-periodic oscillation. The value of e fluctuates between a minimum of approximately 0.008 and a maximum of 0.029. The envelope of this oscillation remains constant; there is no secular growth in the mean eccentricity that would indicate a disruption of the frozen condition by third-body resonance or higher-order lunar harmonics. The bounded oscillation of eccentricity observed in Fig. 6.9 validates the analytical predictions of quasi-frozen behavior discussed in §4.4. The characteristic frequency of the oscillation matches the periodicity observed in the one-year run, driven primarily by the rotation of the line of apsides relative to the Earth-Moon-Sun geometry.

Altitude Bounds: The altitude history in Panel (b) mirrors the eccentricity behavior. The perilune altitude oscillates securely between 45 to 80 km, maintaining a comfortable safety margin above the 35 km clearance floor established in Chapter 4. Simultaneously, the apolune altitude remains bounded between 115 to 150 km.

Eccentricity-Vector Behavior: The same three-year run can also be examined in the eccentricity-vector plane. Figure 6.10 shows the components $e_x = e \cos \omega$ and $e_y = e \sin \omega$ over the full 1095 d simulation, analogous to the one-year portrait in Fig. 6.6. The trajectory forms a compact annulus in (e_x, e_y) space, with the radius oscillating between $e \approx 0.01$ and $e \approx 0.03$ but showing no secular drift. This confirms that the eccentricity vector precesses quasi-periodically in a bounded region of phase space, consistent with the stable envelopes seen in Fig. 6.9.

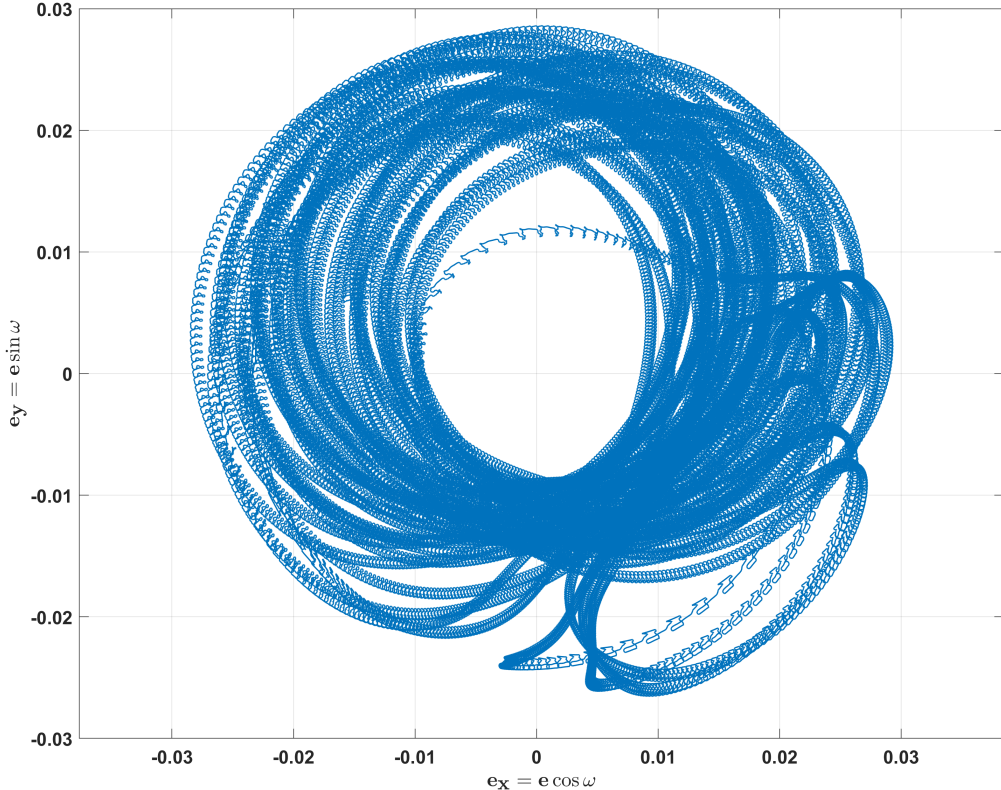


Figure 6.10: Three-year eccentricity-vector portrait for the adopted HADES science orbit. The curve shows the time history of the components $e_x = e \cos \omega$ and $e_y = e \sin \omega$ over the full 1095 d simulation. The trajectory occupies a compact annulus in the (e_x, e_y) plane, indicating that the eccentricity vector precesses while its magnitude remains bounded, with no secular growth in e .

Implications for Mission Architecture

The three-year propagation provides high confidence in the robustness of the HADES trajectory. The absence of monotonic drift in either periapsis or apoapsis altitude confirms that the orbit is effectively “quasi-frozen” over timescales significantly longer than the nominal mission life. The eccentricity-vector portrait in Fig. 6.10 reinforces this conclusion by showing the eccentricity vector confined to a compact annulus in (e_x, e_y) space, with no indication of diffusion toward larger e .

This stability has a direct operational consequence: HADES will not naturally deorbit on mission-relevant timescales. Unlike high-inclination lunar polar orbits, which often experience rapid eccentricity growth leading to surface impact within months, the selected near-equatorial orbit shows no tendency toward impact over the three-year high-fidelity propagation. Consequently, the propulsion subsystem requirement (**PROP-2**) to perform a controlled end-of-life deorbit maneuver is confirmed as necessary to ensure compliance with orbital debris mitigation guidelines.

In summary, the selected orbit ($a = 1833.2\text{ km}$, $e = 0.01044$, $i = 0.30^\circ$, $\Omega = 0^\circ$, $\omega = 160^\circ$, and $\nu = 0^\circ$) meets all performance and stability requirements with significant margin. The three-year validation confirms that the trajectory provides a “safe harbor” for the spacecraft, allowing the mission to focus strictly on science operations without the complexity or propellant cost of routine station-keeping.

Accordingly, this trajectory is adopted as the HADES Design Reference Orbit. The following chapter utilizes this defined orbit as the dynamic baseline to evaluate the power, communications, and data subsystems.

Chapter 7

Power, Communications, and Data

This chapter analyzes the HADES electrical power system, X-band communications link, and onboard data handling for the one-year LLO mission using the FreeFlyer simulation. The analysis uses the same timeline of prime science intervals, Sun and Earth eclipses, and DSN contact opportunities that was used in the orbit design.

The first part of the chapter develops the power subsystem model. It introduces the regulated bus architecture and major loads, builds a component-level power budget to obtain the orbit average electrical load, and applies the solar array model with derating and mean sunlit fraction to check orbit average power (OAP) margin. The same model is then used with worst-case eclipse durations and high load prime science intervals from the year-long simulation to size the battery and verify that the resulting depth of discharge (DoD) stays within the 30 % per orbit limit adopted for HADES.

The later part of the chapter addresses communications and data handling. It examines the X-band link configuration, geometric constraints, and link margins relative to the assumed DSN concept of operations. It then evaluates science data volume, onboard storage requirements, and downlink capacity using the simulated sequence of prime science intervals and DSN contacts. These results evaluate the design’s ability to meet power, link, and data constraints for the reference mission profile.

7.1 Power Architecture Overview

The HADES power subsystem follows a straightforward regulated-bus architecture with maximum power point tracking (MPPT) on the solar array input and a single battery string on the main bus. Figure 7.1 shows the functional flow of power generation, storage, and distribution across the spacecraft.

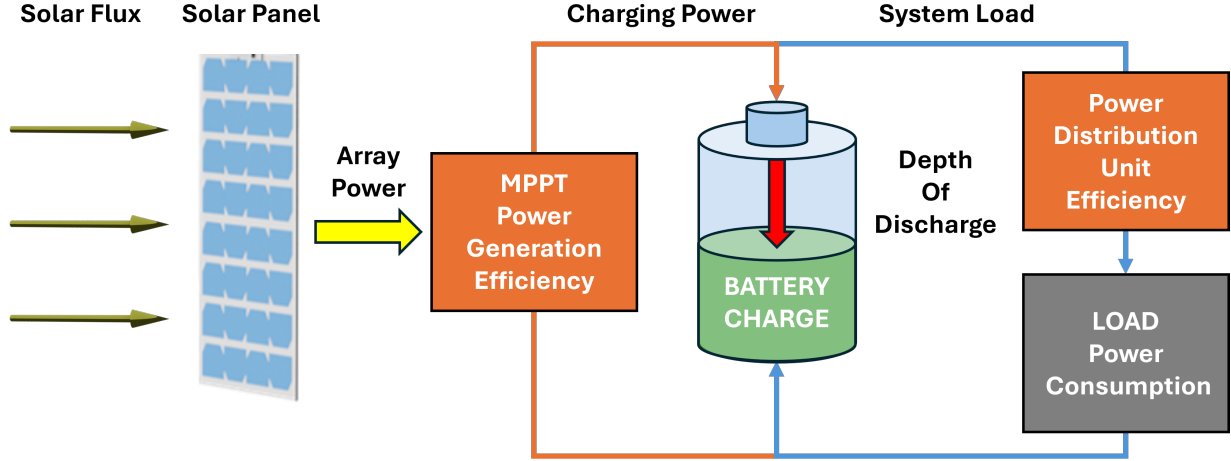


Figure 7.1: HADES power system functional block diagram.

Solar panels convert incident solar flux to array power, which is processed by an MPPT converter, stored in the battery, and distributed through the PDU to spacecraft loads. Battery state of charge and DoD provide the primary performance metrics for the year-long power analysis.

Triple-junction solar panels convert incident sunlight into electrical array power, which is routed to an MPPT converter that tracks the array operating point and regulates charge power into the main bus with efficiency η_{MPPT} . A battery pack provides energy storage and sets the allowable DoD during shadowed operations, while a power distribution unit converts and switches the regulated bus to individual loads with aggregate efficiency η_{PDU} . During sunlit portions of each orbit, the array both supports the instantaneous load and recharges the battery. During eclipse, the battery alone supports all loads and its state of charge decreases. The design objective is to select the solar array area and battery capacity so that HADES meets all load demands with margin under worst-case lighting conditions and mission operations.

7.2 Power Subsystem Sizing

A power budget collects the electrical power requirements for all HADES subsystems, provides estimates for how long each element is active during a representative orbit, and applies design margins to account for uncertainty in both specifications and duty cycles. The resulting budget provides two key quantities. The first is the orbit-average power consumption, which is used with the solar array model in the OAP calculation. The second is the instantaneous peak power demand, which defines the minimum capability required from the power electronics and solar array when all relevant loads are active.

Each component is assigned a nominal power draw based on vendor data or internal estimates. Commercially available subsystems such as the flight computer, reaction wheels, and X-band transceiver receive a 5 % design margin. The radio astronomy payload uses a 20 % margin because its electronics are less mature and have larger performance uncertainty. Duty cycles are expressed as the fraction of time in a representative HADES orbit that each component is active. These duty cycles are derived from the year-long science timeline and the baseline communications concept of operations. The resulting component-level power budget is summarized in Table 7.1.

Table 7.1: HADES power budget and orbit-average power

Subsystem	Nominal Draw [W]	Margin [%]	Adjusted Power [W]	Duty Cycle	Orbit-Average Power [W]
Payload (active)	15.00	20.0	18.00	0.09	1.62
Payload (standby)	2.00	20.0	2.40	0.91	2.18
Payload controller	0.25	20.0	0.30	1.0	0.30
IMU	1.50	5.0	1.58	1.0	1.58
EPS controller	0.15	5.0	0.16	1.0	0.16
Flight computer	0.33	5.0	0.35	1.0	0.35
X-band transceiver (TX)	29.00	5.0	30.45	0.014	0.43
X-band transceiver (RX)	9.00	5.0	9.45	0.0035	0.03
Sun sensors	0.30	5.0	0.32	1.0	0.32
Reaction wheels (steady state)	3.25	5.0	3.41	1.0	3.41
Battery heaters	2.64	5.0	2.77	1.0	2.77
ADCS controller	0.30	5.0	0.32	1.0	0.32
Star tracker	1.00	5.0	1.05	0.5	0.53
Total					14.0

The payload operates in two states. During PrimeScienceTimeB intervals on the lunar far side, the active payload chain draws its full power for a small fraction of each orbit. In the one-year 60 s-step simulation used for power sizing, the total Prime Science B time is approximately 770 hours out of 8760 hours, which corresponds to a payload active duty cycle of 0.09, or roughly ten minutes of science per 117-minute orbit on average. Outside these intervals, the payload remains in a low-power standby state for the remaining 0.91 of each orbit. The payload controller is assumed to be powered continuously, which is reflected in its duty cycle of 1.0.

The remaining bus subsystems that support attitude control and health monitoring are modeled as always on. The flight computer, IMU, EPS controller, reaction wheels, sun sensors, ADCS controller, and average battery heater load all use a duty cycle of 1.0. The star tracker is treated as a fine-pointing sensor that is not required at all times, so a duty cycle of 0.5 is assigned as a mid-range estimate.

The X-band transceiver has two operational modes, transmit (TX) and receive (RX). For the orbit-average power budget, the design assumes one 20 min downlink per day and a shorter 5 min receive interval around each pass for acquisition and uplink commanding. These assumptions correspond to duty cycles of $d_{\text{TX}} \approx 0.014$ and $d_{\text{RX}} \approx 0.0035$, which are applied to the margined TX and RX powers in Table 7.1. In the time-resolved power simulation the RX mode is not scheduled explicitly, because receive activity is confined to sunlit DSN passes and its orbit-average contribution is small (~ 0.03 W) compared with the continuous housekeeping and payload loads. The worst-case eclipse DoD case used for battery sizing assumes no X-band activity, so neglecting the detailed RX timeline does not increase the computed battery stress.

The sum of the orbit-average contributions in Table 7.1 is approximately 14 W. This value represents the orbit-average electrical load that the solar array and power electronics must support in the OAP calculation. The same budget also defines representative peak-power cases. A science peak case with the payload active and all housekeeping subsystems on but the X-band transmitter and receiver off requires about 28 W. A communications peak case with the payload in standby and both transmitter and receiver active requires approximately 53 W. The power subsystem is sized to accommodate the peak communications load with margin, while the 14 W orbit-average load drives the solar array and sunlit fraction analysis in the following section.

7.3 Orbit-Average Power Generation and Solar Array Sizing

The power budget in §7.2 results in an orbit-average electrical load of approximately 14 W. The solar array and power electronics must generate at least this much power on average, with additional margin to account for uncertainties and variation in sun illumination time. This section develops the OAP generation model and uses it to determine the HADES solar array sizing.

The solar array output available on the regulated bus is reduced from its beginning-of-life normal-incidence value by several effects. The combined effect is captured with a single derating factor f_{derate} . The array power is then processed by the maximum power point tracker (MPPT) and the power distribution unit (PDU), which both introduce additional efficiencies η_{MPPT} and η_{PDU} . Only the fraction of each orbit spent in sunlight contributes to energy generation.

The effective bus power while the spacecraft is illuminated is

$$P_{\text{bus,illuminated}} = P_{\text{array,BOL}} f_{\text{derate}} \eta_{\text{MPPT}} \eta_{\text{PDU}}, \quad (7.1)$$

where $P_{\text{array,BOL}}$ is the beginning-of-life array power at normal incidence. The corresponding orbit-average generated power is

$$P_{\text{OAP,gen}} = P_{\text{bus,illum}} f_{\text{sun}} = P_{\text{array,BOL}} f_{\text{derate}} \eta_{\text{MPPT}} \eta_{\text{PDU}} f_{\text{sun}}, \quad (7.2)$$

where f_{sun} is the mean sunlit fraction per orbit. The parameter values used in the HADES design, and the resulting value of $P_{\text{OAP,gen}}$, are summarized in Table 7.2.

Table 7.2: Orbit-average power generation parameters

Quantity	Symbol	Value	Notes
Array BOL electrical power	$P_{\text{array,BOL}}$	82.75 W	Normal incidence, beginning of life
Derating factor	f_{derate}	0.85	Temperature, degradation, harness losses
MPPT efficiency	η_{MPPT}	0.96	Converter efficiency
PDU efficiency	η_{PDU}	0.94	DC-DC and distribution efficiency
Mean sunlit fraction per orbit	f_{sun}	0.6021	From Sun eclipse duration and orbital period
Orbit-average generated power	$P_{\text{OAP,gen}}$	38.22 W	From Eq. (7.2)

The value $P_{\text{array,BOL}} = 82.75$ W comes from the FreeFlyer panel model described in §5.6.9 using the current HADES solar array geometry, cell area, and a nominal triple-junction cell efficiency of 28 %. The combined derating factor f_{derate} is constructed from temperature, lifetime degradation, and harness losses,

$$f_{\text{derate}} = f_{\text{temp}} L_{\text{D}} f_{\text{harness}}. \quad (7.3)$$

The lifetime degradation factor L_{D} follows the SMAD degradation model [38]:

$$L_d = (1 - D)^L, \quad (7.4)$$

where D is the fractional power loss per year and L is the mission duration in years. Using $D = 0.005$ (0.5 %/year) and $L = 1$ year for HADES gives $L_{\text{D}} = (1 - 0.005)^1 \approx 0.995$. A temperature derating of $f_{\text{temp}} = 0.90$ and a harness and mismatch factor of $f_{\text{harness}} = 0.95$ are representative of small-satellite power budgets. The product of these three factors is

$$f_{\text{derate}} = 0.90 \times 0.995 \times 0.95 \approx 0.85, \quad (7.5)$$

which is the value used in Table 7.2 and in the power generation calculation.

The MPPT and PDU efficiencies, $\eta_{\text{MPPT}} = 0.96$ and $\eta_{\text{PDU}} = 0.94$, are representative of available commercial converters and distribution electronics. The mean sunlit fraction $f_{\text{sun}} = 0.6021$ is obtained from the year-long orbit propagation as the average fraction of time that HADES remains outside Sun eclipse.

Substituting these values into Eq. (7.1) gives a bus power in sunlight of

$$P_{\text{bus,illum}} \approx 63.47 \text{ W}, \quad (7.6)$$

and using Eq. (7.2) with $f_{\text{sun}} = 0.6021$ yields an orbit-average generated power of

$$P_{\text{OAP,gen}} \approx 38.22 \text{ W}. \quad (7.7)$$

Comparing this value to the orbit-average load of 14.0 W from Table 7.1 gives an orbit-average power margin

$$M_P = \frac{P_{\text{OAP,gen}} - P_{\text{OAP,load}}}{P_{\text{OAP,load}}} \approx 1.71, \quad (7.8)$$

corresponding to roughly 171 %.

For reference, a 30 % margin requirement on orbit-average load would correspond to a minimum beginning-of-life array power requirement of

$$P_{\text{array,BOL,req}} = \frac{P_{\text{OAP,load}}(1 + 0.30)}{f_{\text{degrade}} \eta_{\text{MPPT}} \eta_{\text{PDU}} f_{\text{sun}}} \approx 39.7 \text{ W}. \quad (7.9)$$

Any array with $P_{\text{array,BOL}} \gtrsim 40 \text{ W}$ would therefore satisfy a 30 % orbit-average power margin for the HADES load and orbital geometry. The dual-deployable array baseline provides 82.75 W at beginning of life, which is more than a factor of two above this requirement and yields generous margin against pointing offsets, hardware degradation, and potential late-stage increases in bus power consumption due to uncertainties in the design and operation of the payload. The next section examines whether the array and battery configuration can also support the worst-case eclipse and Prime Science scenarios in the time domain.

7.4 Battery Sizing and Worst-Case Depth of Discharge

The OAP analysis shows that the HADES solar array can generate significantly more energy per orbit than the 14 W orbit-average electrical load. In practice, the battery is not sized by the orbit-average balance but by the worst-case DoD experienced during eclipses and high-load operations. This section estimates the required battery capacity based on the longest Sun eclipse intervals in the year-long simulation and the corresponding electrical load profile, and then maps that requirement onto a discrete pack architecture.

The HADES design assumes a lithium-ion battery operated with a conservative per-orbit DoD limit of $\text{DoD}_{\max} = 0.30$ to maintain adequate cycle life over the mission. For a given load scenario during eclipse, the required battery capacity is obtained from the maximum eclipse energy demand divided by the allowable DoD.

Worst-Case Eclipse Load Scenarios

The component-level power budget in Table 7.1 provides both the adjusted instantaneous power levels and the duty cycles for each subsystem. For the battery analysis, it is convenient to separate the housekeeping load that remains active at all times from the payload and communications functions that switch between active and standby states.

Summing the adjusted powers for the flight computer, IMU, EPS controller, ADCS controller, sun sensors, reaction wheels, battery heaters, star tracker, and payload controller gives a housekeeping load of

$$P_{\text{house}} \approx 10.26 \text{ W}. \quad (7.10)$$

When the radio astronomy payload is in standby, the total non-science eclipse load becomes

$$P_{\text{ecl,nom}} = P_{\text{house}} + P_{\text{pay,stby}} \approx 10.26 \text{ W} + 2.40 \text{ W} \approx 12.66 \text{ W}, \quad (7.11)$$

where $P_{\text{pay,stby}} = 2.40 \text{ W}$ is the adjusted payload standby power.

During Prime Science B intervals on the far side, the payload operates in its active state while the spacecraft remains in eclipse. In this case the eclipse load increases to

$$P_{\text{ecl,B}} = P_{\text{house}} + P_{\text{pay,act}} \approx 10.26 \text{ W} + 18 \text{ W} \approx 28.26 \text{ W}, \quad (7.12)$$

with $P_{\text{pay,act}} = 18 \text{ W}$, the margin adjusted active payload power. The X-band transmitter and receiver are not scheduled during these dual-occultation science windows and are therefore excluded from the eclipse load.

The maximum Sun eclipse duration over the year-long propagation is approximately

$$T_{\text{ecl,max}} \approx 50 \text{ min} \approx 0.833 \text{ h}, \quad (7.13)$$

which coincides with the longest Prime Science B intervals. The corresponding energy demands on the battery for a worst-case eclipse without science and for a worst-case science eclipse are

$$E_{\text{ecl,nom}} = P_{\text{ecl,nom}} T_{\text{ecl,max}} \approx 12.66 \text{ W} \times 0.83 \text{ h} \approx 10.6 \text{ Wh}, \quad (7.14)$$

$$E_{\text{ecl,B}} = P_{\text{ecl,B}} T_{\text{ecl,max}} \approx 28.26 \text{ W} \times 0.83 \text{ h} \approx 23.6 \text{ Wh}. \quad (7.15)$$

The Prime Science B case has the highest power draw and sets the limiting battery requirement.

Continuous Capacity Requirement

For a battery with usable energy capacity C_{batt} (Wh) and a maximum allowable depth of discharge DoD_{\max} , the DoD associated with a worst-case eclipse event is

$$\text{DoD}_{\text{ecl}} = \frac{E_{\text{ecl}}}{C_{\text{batt}}}. \quad (7.16)$$

Imposing $\text{DoD}_{\text{ecl}} \leq \text{DoD}_{\max}$ yields the minimum required capacity

$$C_{\text{batt},\min} = \frac{E_{\text{ecl},\max}}{\text{DoD}_{\max}}, \quad (7.17)$$

where $E_{\text{ecl},\max}$ is the largest eclipse energy demand over the mission scenarios considered.

Using the Prime Science B case as the worst condition, with $E_{\text{ecl},\max} = E_{\text{ecl,B}} \approx 23.6 \text{ Wh}$ and $\text{DoD}_{\max} = 0.30$, gives

$$C_{\text{batt},\min} \approx \frac{23.60 \text{ Wh}}{0.30} \approx 78.5 \text{ Wh}. \quad (7.18)$$

Any practical HADES battery must provide about 80 Wh of usable energy to keep the DoD below 30% during the longest science eclipse.

Pack-Based Sizing Trade

Commercial small-satellite batteries are often constructed from identical series-parallel packs incorporating 18650 battery form factor elements. A representative 2S1P pack CubeSat battery design uses two 3.7 V cells in series with a 0.70 Ah capacity, resulting in a nominal pack energy of

$$E_{\text{pack}} \approx 7.4 \text{ V} \times 0.70 \text{ Ah} \approx 5.18 \text{ Wh}. \quad (7.19)$$

The example employs fifteen such packs (2S15P) for a total energy of $15E_{\text{pack}} \approx 77.70 \text{ Wh}$. Scaling the HADES battery by the number of 2S1P packs provides a convenient way to explore DoD targets while remaining compatible with a commercially available cell architectures.

For a desired worst-case eclipse depth of discharge D , the continuous energy requirement C_{req} and the corresponding number of packs N_{packs} are

$$C_{\text{req}} = \frac{E_{\text{ecl,B}}}{D}, \quad N_{\text{packs}} = \left\lceil \frac{C_{\text{req}}}{E_{\text{pack}}} \right\rceil, \quad (7.20)$$

where $\lceil \cdot \rceil$ denotes the ceiling function. Table 7.3 summarizes the required capacity, pack count, and resulting actual DoD for several target limits.

Table 7.3: Battery capacity and pack count for different worst-case DoD targets

Target DoD per eclipse	C _{req} [Wh]	Packs N _{packs}	C _{actual} [Wh]	DoD _{actual}
15	157.3	31	160.6	0.147
20	118.0	23	119.1	0.198
25	94.4	19	98.4	0.240

The off-the-shelf fifteen-pack configuration corresponds to an energy capacity of 77.7 Wh and a worst-case eclipse DoD of approximately $23.6/77.7 \approx 0.30$, right at the 30 % limit. Table 7.3 shows that moving into the 20 to 25 % DoD range requires roughly 20 to 25 Wh of additional capacity relative to the theoretical minimum.

For an analysis baseline, a battery composed of eighteen 2S1P packs is selected, for a nominal energy capacity of

$$C_{\text{batt}} = 18E_{\text{pack}} \approx 18 \times 5.18 \text{ Wh} \approx 93.2 \text{ Wh}. \quad (7.21)$$

The resulting worst-case DoD during the longest Prime Science B eclipse is

$$\text{DoD}_{\text{ecl,B}} = \frac{E_{\text{ecl,B}}}{C_{\text{batt}}} \approx \frac{23.6 \text{ Wh}}{93.2 \text{ Wh}} \approx 0.25, \quad (7.22)$$

and the typical non-science eclipse DoD is

$$\text{DoD}_{\text{ecl,nom}} = \frac{E_{\text{ecl,nom}}}{C_{\text{batt}}} \approx \frac{10.6 \text{ Wh}}{93.2 \text{ Wh}} \approx 0.11. \quad (7.23)$$

Both values remain below the 0.30 limit, with the worst case near 25 % and nominal eclipses near 11 %.

Because the illuminated bus power $P_{\text{bus,illuminated}} \approx 63.5 \text{ W}$ exceeds both the Prime Science and communications peak loads, the battery charges whenever the spacecraft is in sunlight and pointed within the nominal Sun-tracking envelope. The year-long simulation therefore does not exhibit cumulative DoD growth over multiple orbits. Instead, the battery repeatedly discharges during eclipses and returns close to a high state of charge before the next shadow period. The 18-pack, 93 Wh configuration together with the 82.75 W array provides adequate margin in both OAP and worst-case DoD for the HADES mission profile, while keeping the eclipse DoD in a regime that is consistent with small-satellite lithium-ion lifetime guidelines.

Time-Domain Power Verification

To complement the analytic DoD sizing, a year-long power simulation is performed using the HADES science orbit, the Prime Science B activity flags, and the scheduled DSN downlink windows. The simulation tracks solar array output, total bus load, and battery state of charge at one-minute resolution. Figure 7.2 shows a representative day near the worst-case Prime Science B day, expressed in elapsed time within the orbit day.

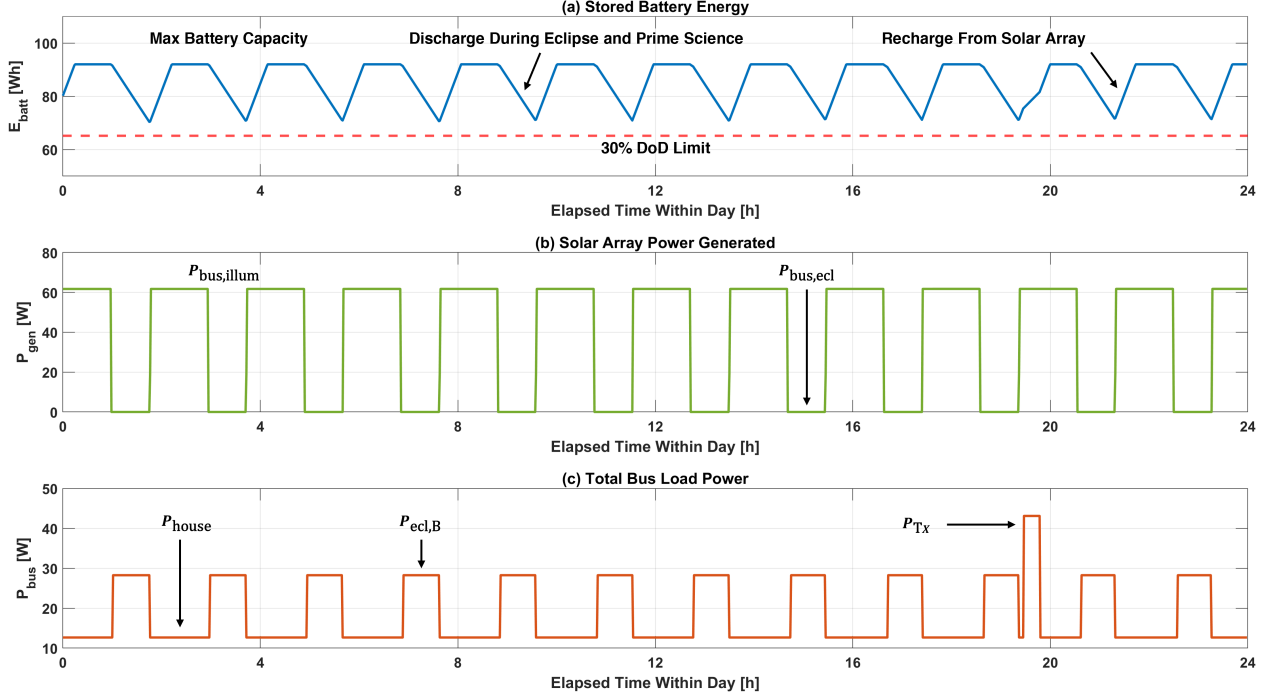


Figure 7.2: HADES representative 24 h power profile for a worst-case Prime Science B day.

Panel (a): battery energy E_{batt} cycles between roughly $E_{\max} \approx 92$ Wh and $E_{\min} \approx 72$ Wh. This variation corresponds to a maximum eclipse DoD of about 25 %, which remains below the 30 % lifetime DoD limit indicated by the red dashed line. Panel (b): instantaneous solar array power P_{gen} , which peaks near 63 W in sunlight and falls to zero in eclipse. Panel (c): total bus power P_{bus} with a baseline housekeeping load of about 12.7 W, an elevated eclipse-plus-Prime Science load near 28 W, and a brief X-band transmit peak reaching roughly 43 W during the scheduled DSN contact.

The time-domain power simulation uses the same margined loads as the orbit-average budget in §7.2. In the FreeFlyer simulation, each subsystem’s instantaneous power draw is taken from the “Adjusted Power” column of Table 7.1 and multiplied by the appropriate on/off flag (payload state, Prime Science B activity, or DSN contact). As a result, the battery energy and DoD histories in Fig. 7.2 already include the 5 % and 20 % design margins applied to the nominal component powers. With the conservative, margined loads used in the simulation, the worst-case eclipse plus Prime Science B event reaches a DoD of about 25 %, still below the 30 % lifetime limit. Because the input loads already carry a 20 % uncertainty margin, the calculated 25 % DoD represents a conservative upper bound. Nominal operations would likely yield significantly lower discharge depths.

7.5 X-Band Communications Link Analysis

The analysis of the communications system determines whether the HADES X-band downlink can return the science and housekeeping data generated by the mission profile without violating any power and pointing constraints described earlier in this chapter. The analysis assumes a one way X-band downlink from HADES to a DSN 34 m ground station and used the same one-year FreeFlyer propagation that drove the orbit and power studies.

Link Configuration and Geometry

An Iris class deep space transponder for HADES X-band communications was selected for the reference mission design, using the power modes and frequency plan given in the Space Dynamics Laboratory datasheet [39]. Iris has heritage from several SLS EM 1 secondary payloads as a flight proven deep space transponder [40]. The transponder provides an RF output power of approximately 4 W in the 8.4 GHz downlink band with symbol rates that comfortably support data rates of order 10^4 bit/s at lunar range. The transmitter drives a fixed spacecraft body mounted X-band antenna with moderate gain and modest off boresight pointing requirements. The ground segment is assumed to be a DSN 34 m antenna with typical X-band performance and system noise temperature representative of current DSN operations.

The FreeFlyer trajectory was used to determine when HADES has geometric line of sight to a notional DSN station. These intervals define potential X-band contacts. In practice, only a subset of these opportunities can be scheduled for downlink after DSN loading, conflicts with other missions, and HADES operations constraints are taken into account. For the purposes of this study, the detailed scheduling problem is replaced by an average allocation of 20 minutes per day of usable X-band downlink time. This assumption is consistent with a low priority small satellite that shares DSN assets with larger deep space missions.

HADES can only transmit when it has geometric LOS to Earth, so all DSN contacts occur on the Earth-facing hemisphere. In addition, the mission concept assumes that X-band downlink is scheduled only during sunlit portions of the orbit to avoid unnecessary battery discharge and is kept separate from Prime Science B intervals. The effective downlink opportunities are therefore the subset of DSN visibility periods that are both sunlit and outside the Prime Science B windows. The pattern in Fig. 7.3 shows that each station provides several contacts and at least one longer pass during a representative day.

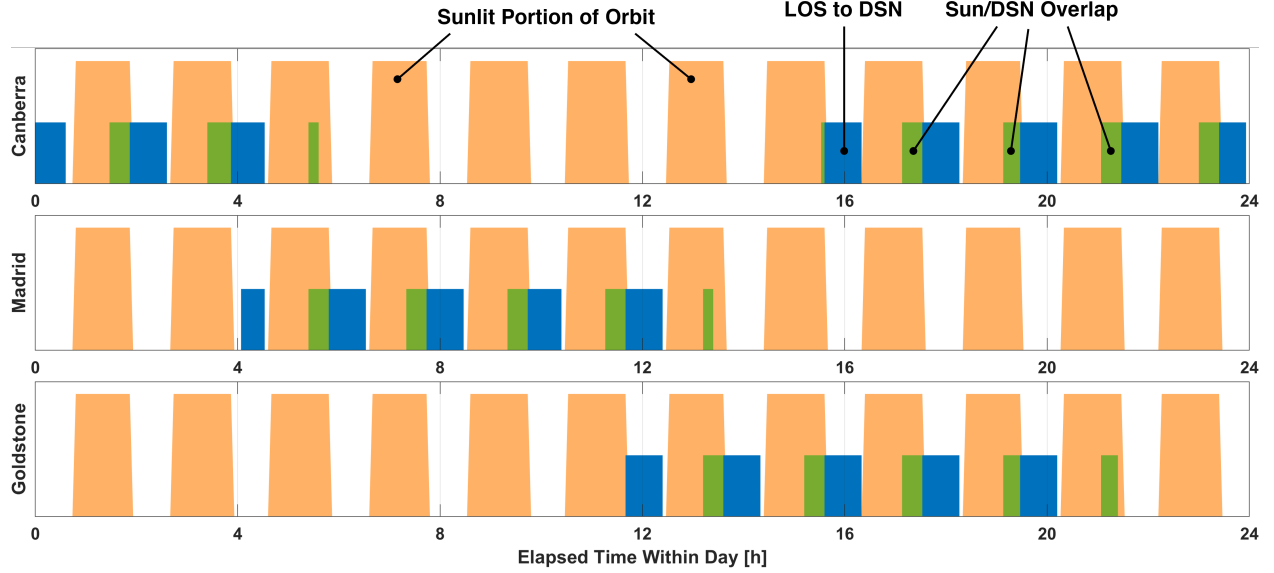


Figure 7.3: DSN contact opportunities and sunlight for a representative mid-mission day.

Each panel shows visibility to one of the three DSN 34 m stations (Canberra, Madrid, and Goldstone) as a function of elapsed time within the day. Pale orange shading indicates intervals when HADES is in sunlight. Blue bars mark periods with geometric LOS to that station. Green bars denote the subset of each contact that occurs in sunlight and is therefore eligible for X-band downlink under the nominal operations assumptions.

Table 7.4 summarizes the contact statistics per station, including the longest sunlit pass duration and start time used for downlink planning.

Table 7.4: DSN contact duration statistics for the representative day shown in Fig. 7.3.

For each DSN station, the table lists the number of contacts, the range and mean of contact durations, the total contact time, and the longest sunlit pass, which is compared against the 20 min daily downlink allocation.

Station	Number of Passes	Minimum Duration [min]	Mean Duration [min]	Maximum Duration [min]	Total Duration [min]	Longest Sun Duration [min]	Start Time of Longest Duration [h]
Canberra	9	12	54.2	68	488	68	17.1
Madrid	6	12	51.3	68	308	68	11.3
Goldstone	6	20	55.3	68	332	68	15.2

Downlink Budget Formulation

The one way X-band downlink is analyzed with a conventional link budget based on the Friis transmission equation [41]. Transmit power, antenna gains, free space path loss, and receiver sensitivity combine to determine the available link margin, as illustrated conceptually in Fig. 7.4. In this view the signal power starts at the transmitter output, is increased by the spacecraft antenna gain to form the effective isotropic radiated power (EIRP), is reduced by propagation losses as it travels to Earth, is boosted again by the ground antenna gain, and is finally compared against the receiver sensitivity or required signal to noise ratio.

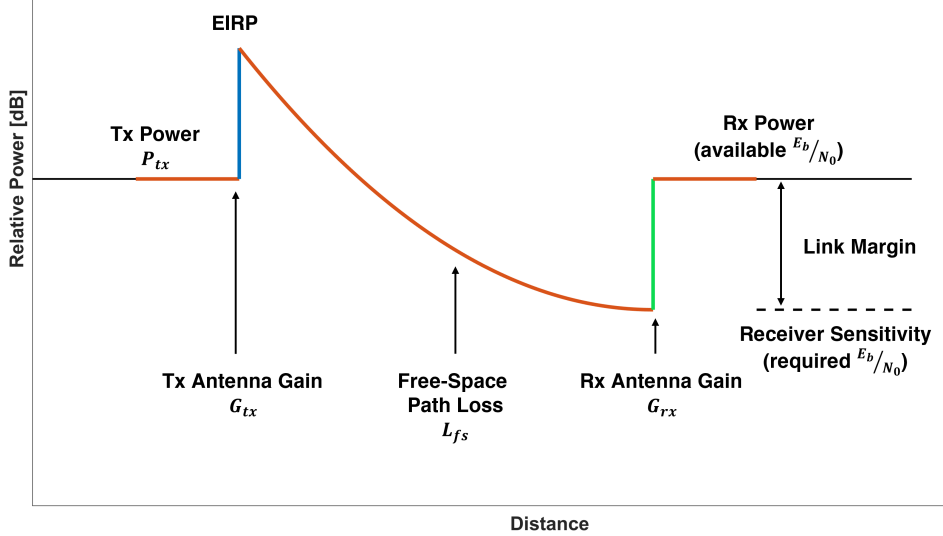


Figure 7.4: HADES X-band link-budget schematic.

Transmit power P_{tx} , antenna gains G_{tx} and G_{rx} , and free-space path loss L_{fs} combine to determine the received carrier power and the link margin relative to the required receiver sensitivity (E_b/N_0).

In free space, the received carrier power P_r is related to the transmitted power P_{tx} by the Friis transmission equation,

$$P_r = P_{tx} G_{tx} G_{rx} \left(\frac{\lambda}{4\pi R} \right)^2, \quad (7.24)$$

where G_{tx} and G_{rx} are the transmit and receive antenna gains, λ is the wavelength, and R is the slant range between HADES and the ground station. It is convenient to express the link in decibel form and separate out the spacecraft side, the propagation loss, and the ground side. The spacecraft EIRP is

$$\text{EIRP} = P_{tx} + G_{tx} - L_{tx}, \quad (7.25)$$

where P_{tx} is the Iris RF output power in dBW, G_{tx} is the spacecraft antenna gain in dBi, and L_{tx} represents cable, mismatch, and pointing losses in dB. The free space path loss between HADES and Earth is

$$L_{fs} = 20 \log_{10} \left(\frac{4\pi R}{\lambda} \right), \quad (7.26)$$

which is about 220 dB at X-band for a nominal Earth–Moon range. Additional losses for polarization mismatch, atmospheric absorption, and implementation margins are collected in a term L_{add} .

On the ground side the figure of merit is the antenna gain to system noise temperature ratio G/T . Using the standard deep space formulation, the carrier to noise density ratio C/N_0 in dB Hz is

$$\left(\frac{C}{N_0} \right)_{\text{dBHz}} = \text{EIRP} + \left(\frac{G}{T} \right) - L_{fs} - L_{add} - k, \quad (7.27)$$

where (G/T) is the DSN 34 m antenna figure of merit in dB/K and $k = -228.60 \text{ dB W/(K Hz)}$ is Boltzmann's constant in decibel units. For the HADES design the Iris radio provides 4 W of RF power, the spacecraft uses a medium-gain X-band antenna, and a DSN 34 m station with typical X-band G/T is assumed. With reasonable values for L_{tx} and L_{add} , the resulting C/N_0 is well above 60 dB Hz at lunar distance.

The downlink margin is assessed in terms of energy per bit to noise spectral density. For a data rate R_b in bit/s,

$$\left(\frac{E_b}{N_0}\right)_{\text{dB}} = \left(\frac{C}{N_0}\right)_{\text{dBHz}} - 10 \log_{10}(R_b), \quad (7.28)$$

so that higher bit rates trade directly against available E_b/N_0 . HADES adopts a conservative downlink rate of $R_b = 64 \text{ kbps}$ using a CCSDS compatible modulation and coding scheme that requires an E_b/N_0 of only a few decibels to meet the desired bit error rate. Substituting the HADES link parameters into Eq. (7.27) and Eq. (7.28) yields an available E_b/N_0 that exceeds the requirement by roughly ten decibels, even after accounting for pointing, atmospheric, and implementation losses. This margin corresponds to the separation between the “Rx Power (available E_b/N_0)” level and the “Receiver Sensitivity (required E_b/N_0)” level in Fig. 7.4, and indicates that the Iris to DSN 34 m link comfortably closes at the selected data rate.

Operational Constraints

The power and pointing constraints identified earlier in this chapter place additional limits on when downlink can occur. The X-band transmitter operates only in sunlight to avoid unnecessary battery discharge and to prevent conflicts with the dual occultation prime science windows. The reaction wheels, star tracker, and antenna pointing solution all must remain within their nominal operating envelopes so that the assumed G_{tx} and L_{tx} values in the link budget remain valid.

Within these constraints, the communications ConOps treats each scheduled DSN contact as a fixed length pass of duration T_{dl} with a constant data rate R_b . Part of each pass is used for command and housekeeping telemetry, and the remainder is available for science data. The detailed balance between science data production and downlink capacity is addressed in the next section.

7.6 Science Data Volume and Downlink Capacity

The final step in the analysis is to compare the science data generated by the HADES payload with the downlink capacity provided by the X-band link and DSN contact assumptions. The instrument concept in Chapter 3 uses a spectrometer that outputs integrated power spectra rather than raw voltage samples, so the stored and downlinked data volume is set by the spectrum resolution and cadence rather than the high internal sampling rate.

Science Data Generation

From the time domain analysis in Chapter 6, the selected HADES orbit yields approximately

$$T_{\text{sci,B,year}} \approx 760 \text{ h} \quad (7.29)$$

of Prime Science B over the one-year mission. This corresponds to an average of about

$$T_{\text{sci,B,day}} = \frac{T_{\text{sci,B,year}}}{365} \approx 2.10 \text{ h/d} \quad (7.30)$$

when the payload is in its active radio astronomy observing mode.

The internal radiometer front end operates at a much higher raw rate (on the order of hundreds of kilobytes per second), but HADES does not store or downlink this raw stream. Instead, the digital processing chain integrates, channelizes, and compresses the data into a science product with an effective downlink rate of

$$R_{\text{sci}} = 8 \text{ kbit/s} \quad (7.31)$$

whenever Prime Science B is active. The total science volume produced over the one-year mission is then

$$V_{\text{sci,year}} = R_{\text{sci}} T_{\text{sci,B,year}} \approx 8 \times 10^3 \text{ bit/s} \times 2.74 \times 10^6 \text{ s} \approx 2.19 \times 10^{10} \text{ bit}, \quad (7.32)$$

or roughly 2.70 GB of science data for the full year.

Downlink Capacity with DSN

The downlink capacity is set by the assumed DSN contact time and the X-band data rate from the previous section. HADES assumes an average of 20 min of scheduled DSN downlink per day at

$$R_b = 64 \text{ kbit/s.} \quad (7.33)$$

The total downlink capacity per day is

$$V_{\text{dl,day}} = R_b T_{\text{dl,day}} = 64 \times 10^3 \text{ bit/s} \times 1200 \text{ s} \approx 7.68 \times 10^7 \text{ bit}, \quad (7.34)$$

or about 9.60 MB/d. Over one year this yields

$$V_{\text{dl,year}} = 365 V_{\text{dl,day}} \approx 2.80 \times 10^{10} \text{ bit}, \quad (7.35)$$

or roughly 3.50 GB of total downlink capacity.

Downlink capacity is shared between science and housekeeping data. HADES reserves a fixed fraction f_{hk} of each DSN pass for housekeeping telemetry and command traffic and uses the remaining fraction for science data. For the present analysis, a 10 % housekeeping allocation is assumed,

$$f_{hk} = 0.10. \quad (7.36)$$

The yearly science downlink capacity is then

$$V_{sci,cap} = (1 - f_{hk})V_{dl,year} \approx 0.9 \times 2.80 \times 10^{10} \text{ bit} \approx 2.52 \times 10^{10} \text{ bit}. \quad (7.37)$$

Data Balance and Storage Margin

Comparing the generated science volume $V_{sci,year}$ to the available science downlink capacity $V_{sci,cap}$ shows that the HADES data volume closes with margin. Using the numbers above,

$$V_{sci,year} \approx 2.19 \times 10^{10} \text{ bit}, \quad V_{sci,cap} \approx 2.52 \times 10^{10} \text{ bit}, \quad (7.38)$$

so the annual science volume uses about 87 % of the science capacity budget. On a daily basis, the payload generates roughly

$$V_{sci,day} = \frac{V_{sci,year}}{365} \approx 6 \times 10^7 \text{ bit}, \quad (7.39)$$

while the science share of the downlink supports about

$$V_{sci,cap,day} = \frac{V_{sci,cap}}{365} \approx 6.90 \times 10^7 \text{ bit}, \quad (7.40)$$

leaving modest margin for variations in the Prime Science B duty cycle and occasional missed passes.

In the actual one-year timeline, many days contain little or no Prime Science B activity. The average rate calculation above is therefore slightly conservative for onboard storage, since days without science allow the DSN passes to draw down any accumulated backlog.

The required onboard storage is set by the amount of data that can accumulate between DSN contacts. In steady state, with the long-term average data generation below the average downlink capacity, the data buffer does not grow without bound. The annual science data volume implied by the 64 kbps, 20 min/d downlink allocation is of order 3×10^{10} bit, consistent with a mission-averaged science product rate of roughly 1 kbps. A worst-case DSN outage of one week at this rate would produce about 6×10^8 bit (approximately 75 MB) of buffered data, and even a month-long outage would require only a few 10^9 bit (a few hundred

megabytes). Commercial solid-state memory devices for CubeSats readily provide hundreds of megabytes to several gigabytes of non-volatile storage, so a 256–512 MB allocation is sufficient for HADES with comfortable margin for housekeeping and calibration data. Onboard data storage is therefore not a limiting driver in the current design.

The X-band link configuration, DSN contact assumption of 20 min/d, and onboard data reduction to an 8 kbit/s science product yield a closed data volume budget with margin. The same simulated timeline that underpins the orbit and power analysis therefore also supports a feasible communications and data handling ConOps for HADES.

Chapter 8

Conclusions

The HADES mission concept represents a step toward accessible, low-frequency radio cosmology. By leveraging the unique radio-quiet environment of the lunar far side, this 12U CubeSat architecture offers a pathway to observing the redshifted 21 cm HI line, a signal from the Cosmic Dawn that remains effectively invisible to terrestrial observatories. This thesis has presented a preliminary systems engineering analysis and high-fidelity simulation framework to evaluate the feasibility of such a mission. The results demonstrate that a CubeSat-class platform can not only survive the dynamic instability of the lunar potential field but also meet the stringent integration time, power, and data requirements necessary for scientific success.

Feasibility of the Science Orbit

A primary challenge of this study was identifying an orbital regime that balances the competing constraints of low altitude (for RFI shielding) and orbital longevity (against lunar mascons). Through the development of a custom simulation environment in FreeFlyer, utilizing the high-resolution GRAIL GL0660B gravity model, this research characterized the complex phase space of low lunar orbits.

The parametric design sweeps conducted in Chapter 6 yielded a critical finding: the existence of a robust family of “quasi-frozen” orbits in the near-equatorial regime. The selected design reference orbit, characterized by a semi-major axis of 1833.2 km, an eccentricity of 0.01044, and a low inclination of 0.30°, demonstrated remarkable stability. As illustrated by the Skittles plots, this specific geometry allows HADES to bypass the strongest gravitational perturbations that would otherwise lead to rapid deorbiting. Unlike higher-inclination orbits that often impacted the surface within months, this trajectory survived the full one-year simulation duration without requiring station-keeping maneuvers.

Significantly, this orbit proved highly efficient for science operations. The simulation verified that the selected trajectory provides 741 h of valid Prime Science integration time over one year in the final 20 s-step verification run, exceeding the 560 h science requirement by approximately 32 % (roughly 180 h of margin). The temporal analysis revealed that while science opportunities are seasonal, driven by the synodic month, the orbit provides a reliable cadence of deep-sky dwells exceeding the 20 min minimum integration threshold.

Subsystem Viability

Beyond orbital dynamics, this thesis evaluated the capability of a 12U bus to support the mission's operational demands. The analysis confirms that standard commercially available components are sufficient to close the critical power and data budgets.

Power Systems: The power analysis in Chapter 7 demonstrated that the proposed dual-deployable solar array, providing 82.75 W at BOL, offers substantial margin. The OAP generation exceeds the average load by approximately 170 %, ensuring the spacecraft remains energy-positive. The battery sizing analysis confirmed that a 93 Wh lithium-ion pack is sufficient to provide power through the worst-case Prime Science B eclipse. The maximum DoD was calculated at roughly 25 %, below the 30 % safety limit typically imposed to ensure battery longevity.

Communications and Data Handling: The study also verified the closure of the communications link satisfying the projected data budgets. Using a standard X-band deep space transponder and a 34 m DSN ground station, the link closes with sufficient margin at 64 kbps. The operational analysis showed that a modest allocation of 20 min of DSN contact time per day yields a total downlink capacity of 3.50 GB/yr. This comfortably accommodates the estimated 2.70 GB of annual science data generated by the instrument, leaving ample overhead for housekeeping telemetry and retransmission requests.

Impact on System Design

The successful identification of a stable, high-yield orbit fundamentally simplifies the HADES spacecraft design. By validating a passive orbital solution, the requirement for a complex, high ΔV propulsion system for station-keeping is eliminated. This significantly reduces the mission's complexity, mass, and cost. The 12U form factor is preserved primarily for the large aperture science payload and necessary power generation, rather than propellant tanks.

Furthermore, the orbital analysis confirms that the science operations concept is robust. The cyclical nature of the Prime Science windows, driven by the synodic month, allows for a predictable and repetitive operations cadence. This predictability simplifies ground operations and allows for the optimization of data downlink schedules well in advance.

Concluding Remarks

The analysis presented in this thesis demonstrates that the HADES mission objectives can be met within the constraints of a 12U platform. By determining a specific quasi-frozen orbit that mitigates the instability of the lunar gravity field, this work eliminates the need for complex station-keeping while maximizing science yield. The accompanying subsystem verification confirms that standard bus components are sufficient to close the power and data budgets required for these observations. Ultimately, this study establishes that small satellites can effectively access the radio-quiet lunar far side, offering a viable pathway to detecting the signal from the Cosmic Dawn.

References

- [1] J. R. Pritchard and A. Loeb, “21 cm Cosmology in the 21st Century,” *Reports on Progress in Physics*, vol. 75, no. 8, p. 086901, Jul. 2012. DOI: [10.1088/0034-4885/75/8/086901](https://doi.org/10.1088/0034-4885/75/8/086901).
- [2] Cavendish Radio Astronomy & Cosmology, *Research*, 2025. [Online]. Available: <https://www.cavendishradiocosmology.com/research.html>.
- [3] J. D. Bowman, A. E. Rogers, R. A. Monsalve, T. J. Mozdzen, and N. Mahesh, “An Absorption Profile Centred at 78 Megahertz in the Sky-Averaged Spectrum,” *Nature*, vol. 555, no. 7694, pp. 67–70, 2018.
- [4] S. Singh, T. Nambissan, R. Subrahmanyam, N. Udaya Shankar, et al., “On the Detection of a Cosmic Dawn Signal in the Radio Background,” *Nature Astronomy*, vol. 6, no. 5, pp. 607–617, 2022.
- [5] J. O. Burns et al., “Probing the First Stars and Black Holes in the Early Universe with the Dark Ages Radio Explorer (DARE),” *Advances in Space Research*, vol. 49, no. 3, pp. 433–450, 2012.
- [6] NASA, *The Electromagnetic Spectrum*, 2022. [Online]. Available: <https://hubblesite.org/contents/articles/the-electromagnetic-spectrum>.
- [7] J. D. Kraus, M. Tiuri, A. V. Räisänen, and T. D. Carr, *Radio Astronomy*, 2nd ed. Powell, Ohio: Cygnus-Quasar Books, 1986.
- [8] NASA, *Lunar Crater Radio Telescope: Illuminating the Cosmic Dark Ages*, 2023. [Online]. Available: <https://www.nasa.gov/solar-system/lunar-crater-radio-telescope-illuminating-the-cosmic-dark-ages/>.
- [9] J. J. Hibbard, J. O. Burns, R. MacDowall, et al., *Results from NASA’s First Radio Telescope on the Moon: Terrestrial Technosignatures and the Low-Frequency Galactic Background Observed by ROLSES-1*, arXiv:2503.09842, Mar. 2025. [Online]. Available: [http://arxiv.org/abs/2503.09842](https://arxiv.org/abs/2503.09842).
- [10] A. Krolikowski and M. Elvis, “Potential and Perils: Paths to Protecting Lunar Sites of Extraordinary Scientific Importance (SESI) for Astronomy Before it is too Late,” *Philosophical Transactions of the Royal Society A*, vol. 382, no. 2271, 2024. DOI: [10.1098/rsta.2023.0078](https://doi.org/10.1098/rsta.2023.0078).
- [11] United States Department of Transportation – Federal Highway Administration, *Systems Engineering for Intelligent Transportation Systems*, 2007. [Online]. Available: <https://ops.fhwa.dot.gov/publications/seitsguide/section3.htm>.
- [12] NASA, *NASA Systems Engineering Processes and Requirements Updated w/Change 2*, 2023. [Online]. Available: <https://nodis3.gsfc.nasa.gov/displayDir.cfm?t=NPR&c=7123&s=1C>.
- [13] D. A. Vallado, *Fundamentals of Astrodynamics and Applications*, 4th. Microcosm Press, 2013.

- [14] K. W. Meyer, J. J. Buglia, and P. N. Desai, "Lifetimes of Lunar Satellite Orbits," NASA Langley Research Center, Hampton, Virginia, Tech. Rep. NASA TP-3394, Mar. 1994. [Online]. Available: <https://www.cs.odu.edu/~mln/ltrs-pdfs/tp3394.pdf>.
- [15] P. Muller and W. Sjogren, "Mascons: Lunar Mass Concentrations," *Science*, vol. 161, no. 3842, pp. 680–684, 1968.
- [16] A. S. Konopliv et al., "High-Resolution Lunar Gravity Fields from the GRAIL Primary and Extended Missions," *Geophysical Research Letters*, vol. 41, no. 5, pp. 1452–1458, 2014.
- [17] T. Hansen, *Spaceborne: The Lunar Orbiter Missions*. NASA SP-242, 1970.
- [18] B. de Saedeleer, "Analytical Theory of a Lunar Artificial Satellite with Third-Body Perturbations," *Celestial Mechanics and Dynamical Astronomy*, vol. 95, no. 1–4, pp. 407–423, 2006. DOI: [10.1007/s10569-006-9029-6](https://doi.org/10.1007/s10569-006-9029-6).
- [19] A. S. Konopliv, S. W. Asmar, E. Carranza, W. L. Sjogren, and D.-N. Yuan, "Recent Gravity Models as a Result of the Lunar Prospector Mission," *Icarus*, vol. 150, pp. 1–18, 2001.
- [20] A. Elipe and M. Lara, "Frozen Orbits About the Moon," *Journal of Guidance, Control, and Dynamics*, vol. 26, no. 2, pp. 238–243, 2003. DOI: [10.2514/2.5064](https://doi.org/10.2514/2.5064).
- [21] W. Lauderdale and W. Eichelman, "Apollo Scientific Experiments Data Handbook," NASA, Tech. Rep. NASA TM X-58131, 1974.
- [22] T. E. Bell, *Bizarre lunar orbits*, *Science@NASA*, NASA Marshall Space Flight Center, Available at https://science.nasa.gov/science-news/science-at-nasa/2006/06nov_loworbit/, 2006.
- [23] D. Lozier, K. Galal, D. Folta, and M. Beckman, "Lunar Prospector Mission Design and Trajectory Support," in *AAS/AIAA Astrodynamics Specialist Conference*, 1998.
- [24] M. Kato et al., "The Kaguya (SELENE) Mission and its Lunar Science," *Space Science Reviews*, vol. 154, pp. 3–19, 2010.
- [25] S. Goossens, K. Matsumoto, Y. Ishihara, H. Noda, et al., "An Improved Lunar Gravity Field Model from SELENE and Historical Tracking Data: Revealing the Farside Gravity Features," *Journal of Geophysical Research: Planets*, vol. 116, no. E7, E07002, 2011.
- [26] M. Beckman, "Mission Design for the Lunar Reconnaissance Orbiter," in *2007 IEEE Aerospace Conference*, 2007, pp. 1–11.
- [27] M. Mesarch et al., "Lunar Reconnaissance Orbiter: 14 Years of Station Keeping," *AAS Guidance, Navigation, and Control Conference*, 2023.
- [28] V. Zharkov and V. Trubitsyn, *Physics of Planetary Interiors*. Astronomy and Astrophysics Series, Pachart, 1978.
- [29] H. Melosh et al., "The Origin of Lunar Mascon Basins," *Science*, vol. 340, no. 6140, pp. 1552–1555, 2013.
- [30] M. T. Zuber et al., "Gravity Field of the Moon from the GRAIL Mission," *Science*, vol. 339, no. 6120, pp. 668–671, 2013.
- [31] G. Chin et al., "Lunar Reconnaissance Orbiter Overview: The Instrument Suite and Mission," *Space Science Reviews*, vol. 129, pp. 391–419, 2007.

- [32] H. Wirnsberger, S. Krauss, and T. Mayer-Gürr, “First Independent Graz Lunar Gravity Model Derived from GRAIL,” *Icarus*, vol. 317, pp. 324–336, 2019. doi: [10.1016/j.icarus.2018.08.011](https://doi.org/10.1016/j.icarus.2018.08.011).
- [33] E. Mazarico et al., “Orbit Determination of the Lunar Reconnaissance Orbiter,” *Journal of Geodesy*, vol. 86, no. 3, pp. 193–207, 2012. doi: [10.1007/s00190-011-0509-4](https://doi.org/10.1007/s00190-011-0509-4).
- [34] A. Abad, A. Elipe, and E. Tresaco, “Analytical Model to Find Frozen Orbits for a Lunar Orbiter,” *Journal of Guidance, Control, and Dynamics*, vol. 32, no. 3, pp. 888–898, 2009. doi: [10.2514/1.38350](https://doi.org/10.2514/1.38350).
- [35] D. Folta and D. Quinn, “Lunar Frozen Orbits: Numerical Construction and Stability Analysis,” in *20th International Symposium on Space Flight Dynamics*, 2007.
- [36] L. Plice, K. Galal, and J. O. Burns, “Low-Altitude Quasi-Frozen Orbits for the Dark Ages Radio Explorer (DARE),” in *AAS/AIAA Astrodynamics Specialist Conference*, 2017.
- [37] a.i. solutions, “FreeFlyer® Independent Verification & Validation Summary,” a.i. solutions, Inc., Lanham, MD, Tech. Rep., Jul. 2020.
- [38] J. R. Wertz, D. F. Everett, and J. J. Puschell, Eds., *Space Mission Engineering: The New SMAD*. Hawthorne, CA: Microcosm Press, 2011, vol. 28.
- [39] “Iris Radio Version 3.0: Multi-Band Deep Space Communication,” Space Dynamics Laboratory, North Logan, Utah, Tech. Rep. SDL/24-2048 Rev -, 2024.
- [40] M. M. Kobayashi et al., “The Iris Deep-Space Transponder for the SLS EM-1 Secondary Payloads,” *IEEE Aerospace and Electronic Systems Magazine*, vol. 34, no. 9, pp. 34–44, 2019. doi: [10.1109/MAES.2019.2905923](https://doi.org/10.1109/MAES.2019.2905923).
- [41] H. Friis, “A Note on a Simple Transmission Formula,” *Proceedings of the IRE*, vol. 34, no. 5, pp. 254–256, 1946.

Appendix A

Classical Orbital Elements

Overview

The HADES mission analysis relies on the classical set of six Keplerian orbital elements (COEs), $\{a, e, i, \Omega, \omega, \nu\}$, to represent the spacecraft's state with respect to the Moon. These parameters transform the Cartesian position and velocity vectors (\vec{r}, \vec{v}) into geometric quantities that describe the orbit's size, shape, orientation, and the satellite's specific location within it.

Note on Terminology

Standard astrodynamics uses the general terms *periapsis* and *apoapsis* to refer to the closest and farthest points in an orbit. In the context of lunar orbits, these are physically synonymous with *perilune* and *apolune*. To maintain consistency with standard orbital element definitions and the variable notation (r_p, r_a), this appendix uses the general terminology.

Orbital Size and Shape (In-Plane Geometry)

The first two elements define the 2-dimensional geometry of the ellipse itself, independent of its orientation in 3D space.

1. Semi-major Axis (a)

The semi-major axis is defined as half of the major axis of the ellipse. Physically, a defines the “size” of the orbit and determines the specific mechanical energy (ε) of the satellite. For a lunar orbiter, assuming two-body dynamics, energy is conserved and is given by:

$$\varepsilon = -\frac{\mu_{moon}}{2a}, \quad (\text{A.1})$$

where μ_{moon} is the Moon's gravitational parameter. Consequently, a also dictates the orbital period (T) via Kepler's Third Law:

$$T = 2\pi \sqrt{\frac{a^3}{\mu_{moon}}}. \quad (\text{A.2})$$

For the selected design orbit, $a \approx 1833$ km results in a period of approximately 2 hours, driving the cadence of communication passes and eclipse cycles.

2. Eccentricity (e)

The eccentricity is a dimensionless parameter describing how much the orbit deviates from a perfect circle ($e = 0$). Physically, e controls the variation in altitude. It relates the semi-major axis to the radius of periapsis (r_p) and apoapsis (r_a):

$$r_p = a(1 - e) \quad (\text{A.3})$$

$$r_a = a(1 + e), \quad (\text{A.4})$$

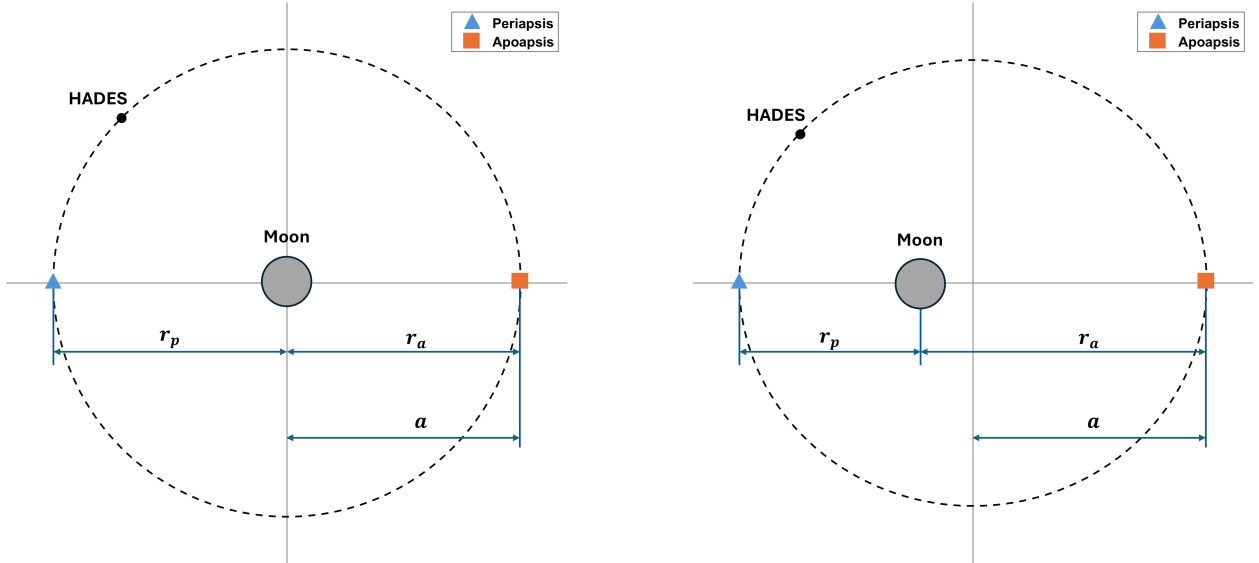
and can be written in terms of these radii as

$$e = \frac{r_a - r_p}{r_a + r_p}. \quad (\text{A.5})$$

A higher eccentricity “flattens” the orbit, and the ratio

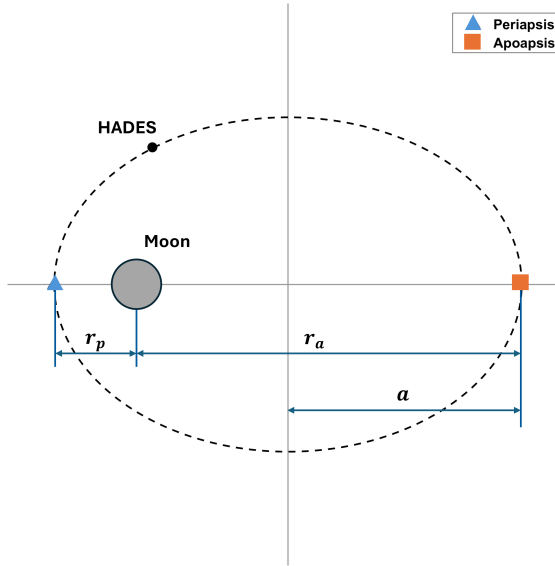
$$\frac{r_a}{r_p} = \frac{1 + e}{1 - e} \quad (\text{A.6})$$

grows rapidly with e , so the orbit becomes more elongated in the direction of the major axis. For HADES, maintaining a quasi-frozen eccentricity is critical: it keeps periapsis safely above the lunar surface and limits apoapsis to preserve the mission's link margin and science sensitivity. Figure A.1 illustrates these relationships for three values of e at a fixed $a = 2000$ km.



(a) $e = 0, a = 2000 \text{ km}, r_p = r_a = 2000 \text{ km}$

(b) $e = 0.3, a = 2000 \text{ km}, r_p = 1400 \text{ km}, r_a = 2600 \text{ km}$



(c) $e = 0.7, a = 2000 \text{ km}, r_p = 600 \text{ km}, r_a = 3400 \text{ km}$

Figure A.1: Effect of eccentricity on orbit geometry for a fixed semi-major axis $a = 2000 \text{ km}$.

As e increases from 0 to 0.7, the periapsis radius decreases from $r_p = 2000 \text{ km}$ to $r_p = 600 \text{ km}$, while the apoapsis radius increases from $r_a = 2000 \text{ km}$ to $r_a = 3400 \text{ km}$. The semi-major axis remains constant, so higher eccentricity produces a more flattened and elongated orbit with lower minimum altitude and higher maximum altitude above the Moon.

Orbital Orientation (Out-of-Plane Geometry)

The next three elements are Euler angles that orient the orbital plane relative to an inertial reference frame. For this mission, the elements are expressed in FreeFlyer's Moon Principal Axis (PA) Inertial frame evaluated at J2000. This frame is centered at the Moon's center of mass and its axes are aligned with the lunar principal moments of inertia at the J2000 epoch. The reference plane is the lunar PA equatorial plane at J2000, and the reference direction is a fixed axis in that plane defined by the principal-axis orientation at that epoch. The frame is treated as inertial, so the reference plane and direction do not rotate with the Moon. The geometric relationship between these angles and the reference plane is illustrated in Fig. A.2.

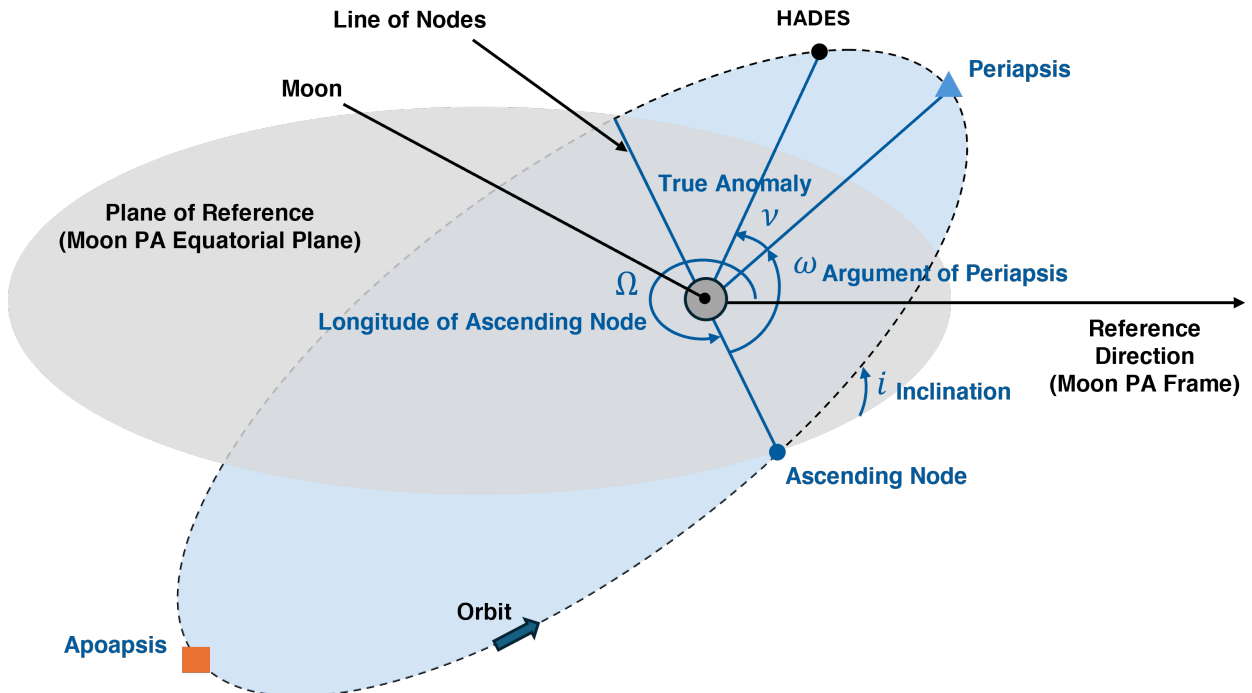


Figure A.2: Geometry of the COE.

The orbital plane is inclined by i relative to a fixed plane of reference, and the line of nodes is defined by the intersection of these planes. The longitude of the ascending node Ω is measured in the reference plane from a fixed reference direction to the ascending node. Within the orbital plane, the argument of periapsis ω is measured from the ascending node to the periapsis direction, and the true anomaly ν locates HADES along the orbit relative to periapsis.

3. Inclination (i)

The inclination defines the tilt of the orbital plane relative to the Moon's PA equatorial plane. For HADES, the mission utilizes a near-equatorial orbit ($i \approx 0.30^\circ$). This contrasts with typical mapping missions which use polar orbits ($i \approx 90^\circ$). The low inclination maximizes time spent in the Moon's shadow during specific seasons, which is crucial for achieving long dual-eclipse radio-quiet intervals.

4. Right Ascension of the Ascending Node (Ω)

The Right Ascension of the Ascending Node (Ω , or RAAN) is the angle measured in the reference plane (the Moon’s PA equatorial plane) from the fixed inertial reference direction of the Moon PA frame to the ascending node, the point where the spacecraft crosses the equator moving northward. Physically, this acts as the swivel of the orbit around the Moon’s polar axis. For HADES, Ω determines the orientation of the orbital plane relative to the Sun and Earth vectors, and therefore strongly influences when the Prime Science seasons occur.

5. Argument of Periapsis (ω)

The argument of periapsis is measured *in the orbital plane* from the ascending node to the periapsis vector. This orients the ellipse within its own plane, determining *where* over the lunar body the satellite reaches its lowest altitude at any given time.

This parameter is critical for the orbital stability analyzed in Chapters 4 and 6. Due to lunar mascons, the long-term evolution of the orbit is highly sensitive to the initial placement of the periapsis. For HADES, selecting a specific initial ω (e.g., near 160°) places the trajectory into a stable, quasi-periodic mode where eccentricity remains bounded, even if the argument itself circulates over time.

Satellite Position

6. True Anomaly (ν)

The true anomaly is the angle measured in the direction of motion from the periapsis to the spacecraft’s current position vector \vec{r} . While ν is a geometric angle, it provides the instantaneous timing of the satellite. In the context of HADES, ν determines the instantaneous altitude and whether the satellite is currently on the near side (communications phase) or far side (science phase) of the Moon.

Summary of HADES Elements

The selection of these six elements constitutes a multi-objective optimization problem. While they mathematically define a single trajectory state, from a systems engineering perspective they can be categorized into two distinct functional groups.

The first group, comprising the semi-major axis (a), eccentricity (e), and argument of periapsis (ω), governs the dynamical stability of the spacecraft. As detailed in Chapter 6, these three parameters must be precisely coupled to counteract the lunar gravitational anomalies (mascons). Any significant deviation in this “survival triad” disrupts the quasi-frozen condition and leads to rapid eccentricity growth and surface impact.

The second group consists of inclination (i) and the Right Ascension of the Ascending Node (Ω), which together govern scientific performance. These angular elements determine the orbital plane's orientation relative to the Earth and Sun, thereby defining the seasonal cadence and duration of the dual-shielded Prime Science windows.

Table A.1 summarizes this functional decomposition, linking each classical element to its primary role in the HADES mission architecture.

Table A.1: Summary of Orbital Elements for HADES

Symbol	Name	Unit	Engineering Function
a	Semi-major Axis	km	Sets orbital energy and period.
e	Eccentricity	-	Sets the altitude envelope (Δh) via periapsis and apoapsis radii.
i	Inclination	deg	Determines visible latitude bands.
Ω	RAAN	deg	Orients orbit plane relative to Earth/Sun vectors.
ω	Arg. of Periapsis	deg	Sets perilune longitude to minimize long-term eccentricity growth.
ν	True Anomaly	deg	Provides the instantaneous “clock angle” of the satellite along the orbit.

Appendix B

HADES FreeFlyer Simulation Code

The HADES FreeFlyer simulation code presented in this thesis can be requested from the author or accessed at: https://github.com/cyoung701/HADES_FreeFlyer_code.git